

# **Computational Study of the Properties and Stabilities of Endohedral Metallofullerenes**

**Timothy James Fuhrer**

**Dissertation submitted to the faculty of the Virginia Polytechnic Institute and State  
University in partial fulfillment of the requirements for the degree of**

**Doctor of Philosophy  
In  
Chemistry**

**Harry C. Dorn, Chair  
Daniel Crawford  
Louis A. Madsen  
James M. Tanko  
Eduard F. Valeyev**

**April 2, 2013  
Blacksburg, VA**

**Keywords: Fullerenes, Endohedral, Metallofullerenes, Density Functional Theory**

**Copyright 2013**

# Computational Study of the Properties and Stabilities of Endohedral Metallofullerenes

Timothy James Fuhrer

## ABSTRACT

The chemistry of fullerenes, which are a class of carbon allotropes that can be prepared by vaporization of graphite in an electric arc in a low pressure atmosphere,<sup>1</sup> has become a topic of much experimental and theoretical study over the past 25 years. Herein we present a series of theoretical studies related to recently discovered or studied endohedral metallofullerenes (EMF) and a theory as to the selective stability of certain isomers of EMFs.

Computational treatments of the anions of C<sub>80</sub> and C<sub>94</sub> are presented and compared in an effort to gain an understanding and predictive model for which isomers of each cage size EMF will be most stable. A model is proposed in which the pentagons of fullerene anions are seen as charge localization centers that repel one another, making the pyracyclene bonding motif much more unstable for fullerene anions than for fullerene neutral cages.

Computational treatments are also presented for two newly discovered EMFs, Y<sub>2</sub>C<sub>2</sub>@C<sub>92</sub> and Gd<sub>2</sub>@C<sub>79</sub>N. Y<sub>2</sub>C<sub>2</sub>@C<sub>92</sub> is reported to exhibit a previously undiscovered mode of internal cluster rotation, while Gd<sub>2</sub>@C<sub>79</sub>N is shown to have unusual stability for an azofullerene with a large spin quantum number (15/2).

Finally, computational techniques are employed to predict the thermodynamic feasibility of a chemical reaction replacing one metal atom in a trimetallic-nitride

template (TNT) endohedral metallofullerene with different metal atom. At least two of these are predicted to be thermodynamically practical.

## **AUTHOR'S ACKNOWLEDGMENTS**

Thank you so much to my mentor, Dr. Harry C. Dorn for taking a chance on me and seeing my potential when others did not. You have turned me into a real scientist and I hope to carry on your legacy in bringing the best out in others.

Thanks also go out to my committee members, Dr. Daniel Crawford, Dr. James Tanko, Dr. Lou Madsen, and Dr. Ed Valeyev for their support and guidance throughout my graduate school career.

Wujun Fu, Jainfei Zhang, Jason Zhang, Cocoa Wang, Hunter Champion, Jim Duchamp, Stephanie Hurt, Caitlyn Dixon, Sarah Black, thank you all so much for the friendship and support you have given me as fellow members of the Dorn group.

Kyle Wilmsmeyer, Amanda Neighbors Hudson, Stephanie Antolak, Steve June, Ryan Fortenberry, Josh Layfield, Erin Durke Davis, Scott Forbey, and Ashley Nelson, I thank you all so much for the friendship and support you have given me during my years at Virginia Tech. You challenged me intellectually and supported me emotionally through all of the good and trying times of my graduate career.

Thank you so much to the faculty and administration at Radford University for their continuous support in the advancement of my academic career and scholarship.

My Parents, Norman and Hope Fuhrer, have been instrumental over the course of my life in helping me learn how to move toward my life goals, both personally and professionally. I am nearly as good a parent for my children as they have been for me.

Finally, I thank my wife and children for their constant love and support of me as I have chased dreams for the last so many years. Without their help, I would never have caught one.

# TABLE OF CONTENTS

<b>ABSTRACT</b> .....	<b>ii</b>
<b>AUTHOR'S ACKNOWLEDGMENTS</b> .....	<b>iv</b>
<b>TABLE OF CONTENTS</b> .....	<b>v</b>
<b>LIST OF FIGURES</b> .....	<b>ix</b>
<b>LIST OF TABLES</b> .....	<b>xiv</b>
<b>OVERVIEW OF THESIS</b> .....	<b>1</b>
<b>CHAPTER 1: INTRODUCTION AND LITERATURE REVIEW</b> .....	<b>6</b>
INTRODUCTION .....	6
EARLY THEORY .....	9
INCORPORATION OF STATISTICAL MECHANICS .....	11
ENDOHEDRAL METALLO-FULLERENES (EMF) .....	17
USE OF DENSITY FUNCTIONAL THEORY FOR FULLERENE MODELING .....	22
THE FORMATION OF FULLERENES AND EMFS.....	24
<b>CHAPTER 2: C<sub>94</sub> DIELECTRON AFFINITIES.....</b>	<b>26</b>
CONTRIBUTIONS .....	26
INTRODUCTION .....	26
COMPUTATIONAL METHODS .....	29
RESULTS AND DISCUSSION .....	31
CONCLUSION .....	36

<b>CHAPTER 3: C<sub>80</sub>: ENERGIES, CHARGES, AND PYRACYCLENE BONDS ....</b>	<b>37</b>
CONTRIBUTIONS .....	37
INTRODUCTION .....	37
COMPUTATIONAL METHODS .....	38
RESULTS AND DISCUSSION .....	40
CONCLUSION .....	47
<b>CHAPTER 4: Y<sub>2</sub>C<sub>2</sub>@C<sub>2n</sub>: AN ENDOHEDRAL METAL CARBIDE</b>	
<b>FULLERENE.....</b>	<b>49</b>
CONTRIBUTIONS .....	49
INTRODUCTION .....	49
COMPUTATIONAL METHODS .....	54
RESULTS .....	55
DISCUSSION .....	62
CONCLUSION .....	64
<b>CHAPTER 5: Gd<sub>2</sub>@C<sub>79</sub>N: STRUCTURAL AND ELECTRONIC PROPERTIES .</b>	<b>66</b>
CONTRIBUTIONS .....	66
INTRODUCTION.....	66
EXPERIMENTAL AND COMPUTATIONAL METHODS .....	67
RESULTS AND DISCUSSION .....	69
CONCLUSION .....	72

<b>CHAPTER 6: METATHESIS: REPLACING A METAL ATOM IN A</b>	
<b>FULLERENE CAGE .....</b>	<b>73</b>
CONTRIBUTIONS .....	73
INTRODUCTION .....	73
COMPUTATIONAL METHODS .....	76
RESULTS AND DISCUSSION .....	78
CONCLUSION .....	82
<b>CHAPTER 7: CONCLUDING REMARKS .....</b>	<b>84</b>
GENERAL COMMENTS.....	84
FULLERENE ANIONS .....	85
CARBIDE CLUSTERS .....	86
OTHER FUTURE DIRECTIONS .....	87
CONCLUSION .....	88
<b>APPENDIX 1: Relative Energies of <math>C_{94}^{2-}</math> ion isomers .....</b>	<b>89</b>
<b>APPENDIX 2: Effect on atomic charges and bond lengths of adding 6 electrons to</b>	
<b>each isomer of <math>C_{80}</math>. Bond types are shown in more detail in Figure 4 (a=4 Hexagons,</b>	
<b>b=Pyracyclene, c=Pent. to Hex., d=Pent. Edge).....</b>	<b>90</b>
<b>APPENDIX 3: Dependence of relative energy (kJ/mol) of <math>C_{80}</math> IPR isomers on charge</b>	
<b>of the cage. The <math>D_{5h}(6)C_{80}^{2-}</math> is shown to have the lowest energy of the 49 systems</b>	
<b>modeled .....</b>	<b>91</b>

<b>APPENDIX 4: Six geometries of <math>Y_2C_2C_{92}</math> optimized to confirm carousel rotation hypothesis. For each structure, the cage symmetry axis is horizontal through the cluster .....</b>	<b>92</b>
<b>APPENDIX 5: Complete plot of dielectrion affinities of the <math>C_{94}</math> IPR isomers vs. number of pyracyclene motifs on each and verse number of para-fused-pentagon motifs on each .....</b>	<b>93</b>
<b>REFERENCES .....</b>	<b>94</b>



## LIST OF FIGURES

<b>Figure 1: Model of <math>\text{Ca}@(\text{I}3\text{C}_{3\text{v}})\text{C}_{94}</math> discovered by Dorn Group .....</b>	<b>1</b>
<b>Figure 2: Model of <math>\text{Y}_2\text{C}_2@\text{C}_{92}</math>, shown with pyracylene carbon atoms highlighted in blue .....</b>	<b>2</b>
<b>Figure 3: Translucent density surface map of <math>\text{Y}_2@\text{C}_{92}^{2+}</math> .....</b>	<b>4</b>
<b>Figure 4: Example of proposed metathesis reaction .....</b>	<b>5</b>
<b>Figure 5: Truncated icosahedron and soccer ball .....</b>	<b>6</b>
<b>Figure 6: Models of <math>\text{C}_{60}(\text{I}_h)</math> and <math>\text{C}_{70}(\text{D}_{5h})</math>. Each corner represents a carbon atom ...</b>	<b>7</b>
<b>Figure 7: Models of the three isomers of <math>\text{C}_{78}</math> isolated by Kikucki <i>et al.</i> The <math>\text{D}_3</math> isomer is on the left with the two <math>\text{C}_{2\text{v}}</math> isomers in the center and on the right ..</b>	<b>8</b>
<b>Figure 8: Models of the two isomers of <math>\text{C}_{84}</math> isolated separately by Diederich <i>et al</i> and Kikuchi <i>et al.</i> The dominant <math>\text{D}_2</math> isomer is on the left. The <math>\text{D}_{2\text{d}}</math> isomer is on the right .....</b>	<b>9</b>
<b>Figure 9: Model of <math>\text{La}@\text{C}_{60}</math> using van der Waals radius for lanthanum .....</b>	<b>17</b>
<b>Figure 10: Model of <math>\text{Sc}_3\text{N}@\text{C}_{80}</math> using van der Waals radii for scandium and nitrogen .....</b>	<b>18</b>
<b>Figure 11: Anti-aromatic fused pentagons, aromatic fused pentagons with 2- charge .....</b>	<b>22</b>
<b>Figure 12: Anti-aromatic neutral bonding motifs and aromatic di-anion bonding motifs .....</b>	<b>28</b>
<b>Figure 13: Four different bonding motifs for IPR fullerenes .....</b>	<b>29</b>
<b>Figure 14: Average <math>\text{C}_{94}</math> Dielectron Affinities computed at the B3LYP/3-21G level of theory vs. number of para-fused-pentagons .....</b>	<b>32</b>

<b>Figure 15: Average <math>C_{94}</math> Dielectron Affinities computed at the B3LYP/3-21G level of theory vs. number of para-fused-pentagons .....</b>	<b>33</b>
<b>Figure 16: HOMO-1 and HOMO for <math>C_{94}^{2-}(I34)</math>.....</b>	<b>34</b>
<b>Figure 17: LUMO <math>C_{94}^{2-}(I34)</math>.....</b>	<b>35</b>
<b>Figure 18: Mulliken charge analysis of <math>C_{94}^{2-}(I34)</math>. More negatively charged atoms shown in red.....</b>	<b>36</b>
<b>Figure 19: The seven IPR isomers of <math>C_{80}</math> .....</b>	<b>40</b>
<b>Figure 20: Relative electronic energy versus charge for the seven IPR isomers of <math>C_{80}</math> .....</b>	<b>40</b>
<b>Figure 21: Relative electronic energy versus charge for the seven IPR isomers of <math>C_{80}</math> focused around the minima.....</b>	<b>41</b>
<b>Figure 22: Plot of Pyracyclene count for each IPR isomer of <math>C_{80}</math> versus the charge of the cage at its energy minimum .....</b>	<b>43</b>
<b>Figure 23: Plot of Para-Fused-Pentagon count for each IPR isomer of <math>C_{80}</math> versus the charge of the cage at its energy minimum .....</b>	<b>44</b>
<b>Figure 24: Model of the <math>C_{80}^{2-}(6)D_{5h}</math> anion showing the relative Mulliken charges for each atom from two different points of view .....</b>	<b>46</b>
<b>Figure 25: Plot of the HOMO of <math>C_{80}^{2-}(6)D_{5h}</math> from two different points of view .....</b>	<b>47</b>
<b>Figure 26: 800MHz <math>^{13}C</math> NMR spectrum of <math>Y_2C_2@D_3(85)-C_{92}</math> in <math>CS_2</math> with 10 mg <math>Cr(acac)_3</math> relaxant, acetone-<math>d_6</math> lock after 32768 scan at 25 °C. (a) The whole range of <math>^{13}C</math> NMR spectrum of <math>Y_2C_2@D_3(85)-C_{92}</math> (b) Expand range (from 128 to 154 ppm) of <math>^{13}C</math> NMR spectrum of <math>Y_2C_2@D_3(85)-C_{92}</math>. The signal marked with * is assigned to impurities because it was not visible in the 600</b>	

MHz $^{13}\text{C}$ NMR and its unreasonable chemical shift. (c) Calculated $^{13}\text{C}$ NMR spectrum of $\text{Y}_2\text{C}_2@D_3(85)\text{-C}_{92}$ .....	51
Figure 27: $^{13}\text{C}$ -NMR for $\text{Y}_2\text{C}_2@C_{2v}(8)\text{C}_{82}$ .....	52
Figure 28: Nanoscale fullerene compression of yttrium carbide endohedral fullerenes. (a) $\text{Y}_2\text{C}_2^{4+}$ cluster without a cage. (b) Linear $\text{Y}_2\text{C}_2^{4+}$ cluster inside a large fullerene cage. (c) $\text{Y}_2\text{C}_2^{4+}$ cluster with carbide bond vector orthogonal to the yttrium-yttrium vector in a compressed fullerene cage. (d) $\text{Y}_2\text{C}_2^{4+}$ cluster with carbide bond vector orthogonal to and deviated from yttrium-yttrium vector. (e) Mass-spectrometry showing a family of endohedral metallofullerenes with formula $\text{Y}_2\text{C}_{2n}$ .....	53
Figure 29: Front and side view of starting geometry for $\text{Y}_2\text{C}_2@C_{3v}(8)\text{C}_{82}$ .....	54
Figure 30: Computational model of $\text{Y}_2\text{C}_2@C_{100}$ . Cluster is slightly compressed with Y-C-C bond angles of 157.6 degrees and a dihedral angle of 15.6 degrees ...	56
Figure 31: Two views of the modeled cluster geometry for $\text{Y}_2\text{C}_2@C_{92}$ . The left view (a) is the optimized structure while the right view (b) is the transition state structure between two equivalent optimized structures .....	56
Figure 32: Energetics of Rotation of $\text{Y}_2\text{C}_2$ Cluster within the $\text{C}_{92}$ Cage .....	58
Figure 33: $\text{Y}_2\text{C}_2$ from two different viewpoints with pyracyclene atoms shown in dark blue .....	59
Figure 34: Equatorial carbon atoms on the $\text{C}_{92}$ cage. Atoms with significant signal broadening in the NMR show in orange, those without significant signal broadening, the pyracyclene motifs, are shown in blue .....	60

<b>Figure 35: Raman spectroscopy of <math>Y_2C_2@C_{92}</math> at several temperatures with matching <math>C_2</math> free rigid rotor frequencies .....</b>	<b>61</b>
<b>Figure 36: Optimized structure of <math>Y_2C_2@C_{82}</math>. Symmetry axis for each view is shown in red .....</b>	<b>62</b>
<b>Figure 37: The change of interatomic distances upon compression. Red lines and points denote the data obtained from NFC (data source Table 2, <math>C_\infty</math> represents the calculated interatomic distances for <math>(Y_2C_2)^{4+}</math> cluster), and blue lines and points denote the data obtained from MPC (data source Ref. <sup>119</sup>. Y-C distances are average values of corresponding Y-C1, Y-C2 and Y-C3 distances in the lattice. Y-Y distances are average values of corresponding Y-Y1 and Y-Y2 distances in the lattice). (a) Y-C distances in fullerene cages. (b) Y-Y distances in fullerene cages. (c) Y-C distances in superconducting materials. (d) Y-Y distances in superconducting materials .....</b>	<b>64</b>
<b>Figure 38: HPLC Chromatography of soot extracts containing <math>Gd_2@C_{79}N</math> fractions and <math>Y_2@C_{79}N</math> fractions from separate soot preparations .....</b>	<b>68</b>
<b>Figure 39: DFT HOMO-LUMO levels of <math>(C_{80})^{6-}</math>, <math>(C_{79}N)^{5-}</math> and <math>(C_{79})^{6-}</math> cages .....</b>	<b>70</b>
<b>Figure 40: DFT MO energy level diagrams optimized for <math>Y_2@C_{79}N</math> and <math>Gd_2@C_{79}N</math> .....</b>	<b>71</b>
<b>Figure 41: Unpaired Spin Density (<math>\alpha</math>) distribution for <math>Y_2@C_{79}N</math> and <math>Gd_2@C_{79}N</math> ...</b>	<b>72</b>
<b>Figure 42: Synthesis and functionalization of b-emitting <math>Lu_3N@C_{80}</math> for use in cancer therapy .....</b>	<b>74</b>
<b>Figure 43: Metathesis Reaction between Y (metal) and <math>Sc_3N@C_{80}</math> Yttrium metal powder (~40 mesh) and <math>Sc_3N@C_{80}</math> (mass ratio Y/ <math>Sc_3N@C_{80}</math>=2/1) The pellet</b>	

was irradiated by CO<sub>2</sub> laser (10.6 micrometer, less than 25W) for about 6 minutes under 50 torr of N<sub>2</sub>. (in chamber on the right) .....75

**Figure 44: Sealed quartz tube containing Sc<sub>3</sub>N@C<sub>80</sub> and Al powder for attempted metathesis reaction .....75**

**Figure 45: Plot of computed ΔG of reaction versus temperature for reactions involving Sc<sub>3</sub>N@C<sub>80</sub> and aluminum in several forms. Crystal entropy effects are not included for the oxide case .....78**

**Figure 46: Plot of computed ΔG of reaction versus temperature for reactions involving Sc<sub>3</sub>N@C<sub>80</sub> and lutetium in several forms. Crystal entropy effects are not included for the oxide case .....79**

**Figure 47: Plot of computed ΔG of reaction versus temperature for reactions involving Sc<sub>3</sub>N@C<sub>80</sub> and yttrium in several forms. Crystal entropy effects are not included for the oxide case .....80**

**Figure 48: Plot of computed ΔG of reaction versus temperature for reactions involving Sc<sub>3</sub>N@C<sub>80</sub> and gadolinium in several forms. Crystal entropy effects are not included for the oxide case .....81**

**Figure 49: Plot of computed ΔG of reaction versus temperature for reactions involving Sc<sub>3</sub>N@C<sub>80</sub> and lanthanum in several forms. Crystal entropy effects are not included for the oxide case .....82**

**Figure 50: C<sub>18</sub> unit thought to be a precursor to pentagon closure in fullerenes ....87**

## LIST OF TABLES

<b>Table 1: Relative energies computed for the five most stable isotopes of the C<sub>94</sub> dianion using four different model chemistries .....</b>	<b>30</b>
<b>Table 2: Minima from graph of relative energy (kJ/mole) versus charge for each isomer of C<sub>80</sub> compared to the number of para-fused-pentagons and pyracyclene motifs on each isomer .....</b>	<b>42</b>
<b>Table 3: Key results from NMR experiments and DFT Calculations. Numbers in parentheses are computational results .....</b>	<b>63</b>

## OVERVIEW OF THESIS

Chapter one of this work presents a literature review of the background and history of fullerene computational modeling, focusing on endohedral metallofullerenes (EMF) and systems related to EMFs.

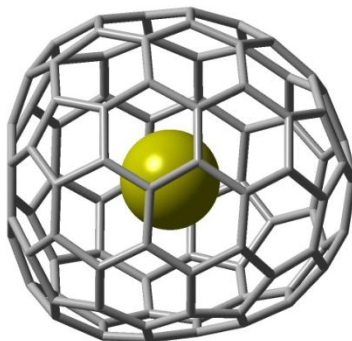


**Figure 1: Model of  $\text{Ca}@(\text{134C}_{3v})\text{C}_{94}$  discovered by Dorn Group.**

In chapter two we present the results of the computational modeling of the complete set of 134 isolated pentagon rule  $\text{C}_{94}^{2-}$  dianion isomers at the B3LYP/3-21G level of theory.<sup>2</sup> The isolated pentagon rule (IPR) states that for most stable fullerenes, none of the twelve pentagons found on the surface will share a common side. Our reason for investigating the dianions of  $\text{C}_{94}$  is that the isomer found to encapsulate calcium or thulium in  $\text{Ca}@C_{94}$  or  $\text{Tm}@C_{94}$  was not the isomer predicted by Slanina and verified by Richter's experiments<sup>3,4</sup> to be the most stable for the  $\text{C}_{94}$  neutral empty cage.<sup>5</sup> The hypothesis that we set out to verify is that the arrangements of the pentagons around the cage not only affects its overall stability, but also its electron affinity, second electron affinity, etc. Our focus in this chapter is on the combination of the first and second electron affinities, which we will refer to as the *dielectron affinity*. This work has not yet

been published but was presented as a professional talk at the meeting of the Virginia Academy of Sciences in Richmond, VA in May of 2009.<sup>6</sup>

In order to develop a better understanding of the effect of the relative positions of the pentagons on a fullerene cage, we have modeled all of the IPR isomers of the  $C_{80}$  set at charges between 0 and 6- with the B3LYP density functional utilizing the 6-31G\* basis set.  $C_{80}$  was chosen because of its relatively small number of IPR isomers (seven). The energy of each isomer was plotted as a function of charge for each isomer, and then compared with the numbers of each bonding motif for each isomer. These results are detailed in chapter three of this work. This work is not yet published but was presented in a professional talk at the Southeast Regional Meeting of the American Chemical Society in New Orleans in 2010.<sup>7</sup>

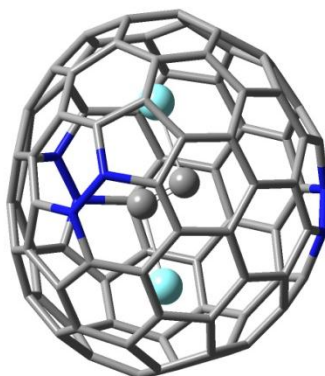


**Figure 2: Model of  $Y_2C_2@C_{92}$ , shown with pyracylene carbon atoms highlighted in blue.**

Chapter four of this work details modeling of the  $Y_2C_2@C_{92}$  molecule. The cage for this molecule has  $D_3$  symmetry and appears to be very similar in structure to the  $Gd_2C_2@C_{92}$  first characterized by Liu and Balch (see **Figure 2** above).<sup>8</sup> Our interest in this molecule from a computational perspective originated from the motion of the yttrium carbide cluster within the cage. Line broadening in the  $^{13}C$ -NMR at high magnetic fields



observed by Wujun Fu (Ph.D. 2009) in our group suggests rotation of the cluster within the cage. Computations so far show a very low energy barrier (~12 kJ/mol) to cluster rotation within the cage, but in a carousel-like motion as the negatively charged carbide atoms avoid approaching the three bonds on the cage that match pyracyclene bonding motif (see the blue colored atoms in **Figure 2** above). Density surface mapping of the molecule without the carbide ( $C_2^{2-}$ ) shows unexpected electron density within the cage behind each of these bonds (See **Figure 3** below). Additionally, the  $Y_2C_2^{4+}$  cluster is modeled inside of a series of cages ranging from  $C_{82}$  to  $C_{100}$ . These models are compared to experimental results for both  $Y_2C_2$  fullerenes and  $Y_2C_3$ , a compound that exhibits superconducting behavior when compressed under large pressures.

Part of the results of my work on this project were published in conjunction with Raman evidence obtained by our collaborator, Brian Burke at the University of Virginia, that supports the hypothesis that the carbon atoms are tunneling from one position on the “carousel” to another without passing through the space in between.<sup>9</sup> However, the bulk of the computational work I did on this project was accepted for publication on April 13, 2012 by the *Journal of the American Chemical Society* in an article titled “*Nanoscale Fullerene Compression of a Yttrium Carbide Cluster*”.<sup>10</sup> I have also reported this work in a professional talk at the international meeting of the Electrochemical Society in Vancouver, BC in 2010.<sup>11</sup>

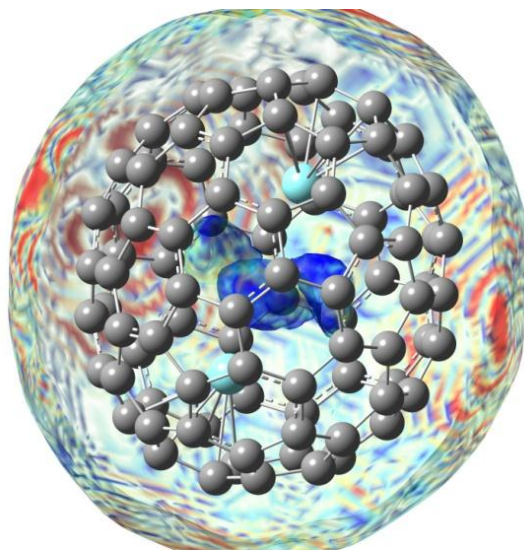


**Figure 3. Translucent density surface map of  $Y_2@C_{92}^{2+}$**

Chapter five of this document details computational models of the  $Gd_2@C_{79}N$  molecule. The focus in this work is on the unexpectedly high band gap of this species, and on the locations of the 15 singly occupied molecular orbitals (SOMO) on the molecule. This work has been published in the *Journal of the American Chemical Society* in 2011.<sup>12</sup>

Chapter six of this document shows computational modeling of the thermodynamics of the hypothetical so-called “metathesis” reaction. In this reaction, one scandium atom in a molecule of  $Sc_3N@C_{80}$  would be replaced by another metal atom such as Gd, Y, Lu, La, etc. Jason Zhang and Hunter Champion from our group have been working on the experimental details of such a reaction. I reported the computational evidence for the plausibility of these reactions at the international meeting of the Electrochemical Society in Montreal, Quebec in May of 2011.<sup>13</sup>

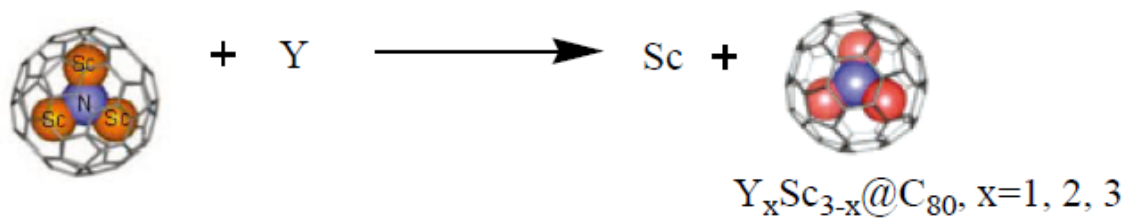


**Figure 4: Example of proposed metathesis reaction.**

Finally, chapter seven of this document presents a summary of findings as well as several possibilities for future computational research on fullerenes.

## CHAPTER 1: INTRODUCTION AND LITERATURE REVIEW

### INTRODUCTION:

The chemistry of fullerenes, which are a class of carbon allotropes that can be prepared by vaporization of graphite in an electric arc in a low pressure atmosphere,<sup>1</sup> has become a topic of much experimental and theoretical study over the past 25 years. The first report of experimental production of fullerenes in a refereed journal was in November of 1985 when H. W. Kroto and his collaborators found, using time-of-flight mass spectrometry, a cluster containing 60 carbon atoms in the products of laser irradiated graphite.<sup>14</sup> Kroto's group postulated the truncated icosahedron structure for this species in which  $sp^2$  hybridized carbon atoms are found at each vertex of a structure similar to that of a soccer ball (see **Figure 5** below).

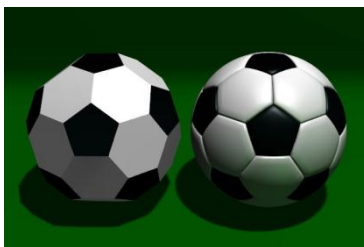


**Figure 5: Truncated icosahedron and soccer ball. (This image was copied with permission from reference number <sup>15</sup>)**

At that time, Kroto's group did not have experimental evidence to support this hypothetical structure. Kratschmer's 1990 experiments gave some spectral support to this hypothesis via infrared spectroscopy.<sup>1</sup> Later that same year, Kroto's group was able to add additional experimental evidence to the validity of their proposed truncated icosahedron structure of the  $C_{60}$  molecule using Carbon-13 NMR.<sup>16</sup> The existence and structure of the  $C_{70}$  fullerene was also confirmed in this same work. Since then,  $C_{60}$  and

$C_{70}$  have been discovered to exist in nature in Precambrian rocks,<sup>17</sup> and more recently, in outer space, particularly in “young planetary nebulae”.<sup>18</sup>

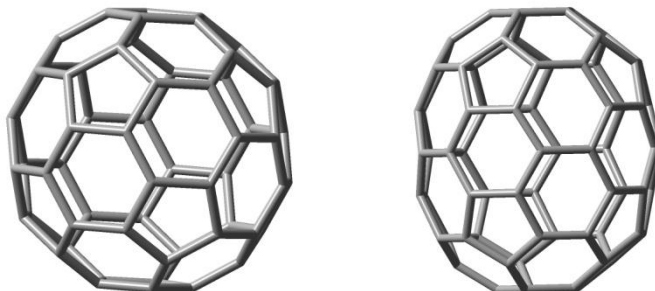


**Figure 6: Models of  $C_{60}(I_h)$  and  $C_{70}(D_{5h})$ . Each corner represents a carbon atom.**

In order to develop a more systematic theory of fullerenes, it is important to define what a fullerene is and generate a list of the theoretically possible fullerenes. A fullerene is defined as a closed-shell, pseudo-spherical molecule composed entirely of carbon atoms in fused five and six membered rings. For a fullerene containing  $n$  atoms ( $C_n$ ), the cage will have 12 pentagonal faces and  $n/2 - 10$  hexagonal faces.<sup>2</sup>

Manolopoulos has postulated that all possible isomers of all fullerenes ( $C_n$ ) can be predicted via a “spiral algorithm” where the fullerene is thought of as an orange that is able to be peeled one face at a time in a continuous spiral about the cage.<sup>19</sup> Using this algorithm, Fowler and Manolopoulos were able to write a computer program to generate all possible isomers for all fullerenes ( $C_n$ ) for  $n \leq 100$ .<sup>2</sup>

This algorithm generates a very large number of possible isomers (1812 for  $C_{60}$  alone), but relatively few are found in experiment. For example, only one is found for  $C_{60}$ . It became convenient, even necessary, to develop a system to further narrow the list of possible isomers for each fullerene ( $C_n$ ). Both experiment and theoretical computations have shown that in general, the most stable fullerenes are those with the 12

pentagons as far apart from one another as possible.<sup>20</sup> The smallest possible fullerene with no fused pentagons is  $C_{60}(I_h)$ , which is why this is the smallest found in significant amounts in experiments. The fact that no fused pentagon, empty cage fullerene isomers are found in significant quantities in experiment is referred to as the Isolated Pentagon Rule (IPR). The closer pentagons are found together on a fullerene the more strained the bond angles are in that area.<sup>21</sup> If consideration is confined to only those isomers that obey the IPR, this narrows down the number of possible isomers considerably (for example; one in the cases of  $C_{60}$  and  $C_{70}$ , seven in the case of  $C_{80}$ ), but the number of IPR isomers for each fullerene ( $C_n$ ) also grows rapidly as  $n$  gets larger (134 for  $C_{94}$ , 450 for  $C_{100}$ ).<sup>2,22</sup>

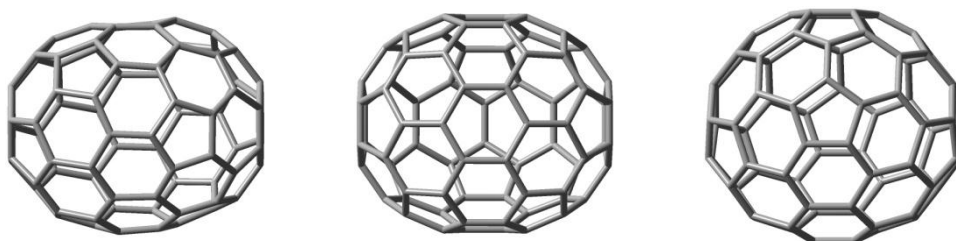


**Figure 7: Models of the three isomers of  $C_{78}$  isolated by Kikuchi *et al.* The  $D_3$  isomer is on the left with the two  $C_{2v}$  isomers in the center and on the right.**

Of the five possible IPR isomers of  $C_{78}$ , only two were found in the empty cage form in the plasma-arc soot by Diederich *et al* in 1991, a  $C_{2v}$  isomer and a  $D_3$  isomer.<sup>23</sup> However three isomers were found by Kikuchi *et al* in 1992 in a 5:2:2 ratio with the dominant isomer being the other IPR  $C_{2v}$  isomer not seen at all by Dietrich, while the minor isomers are the same as the two found by Diederich (see **Figure 7**).<sup>24</sup> These competing findings suggest that the concentrations found for isomers of a given cage size especially depends on kinetic factors more critically than the thermodynamic stability of

the isomers, at least when the thermodynamic stabilities of two or more competing isomers are close to one another.

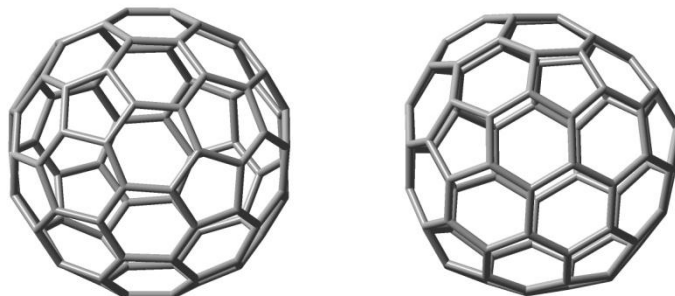


**Figure 8: Models of the two isomers of  $C_{84}$  isolated separately by Diederich *et al* and Kikuchi *et al*. The dominant  $D_2$  isomer is on the left. The  $D_{2d}$  isomer is on the right.**

However, of the 24 possible IPR isomers of  $C_{84}$ , only two are found (a  $D_2$  and a  $D_{2d}$  isomer), in a 2:1 ratio by both Diederich *et al*, and Kikuchi *et al*, suggesting that for some cage sizes, thermodynamic stabilities do override kinetic effects regardless of experimental parameters.<sup>24,25</sup> All of this leads to the desire to develop a more comprehensive theory of the stabilities and mechanisms of formation for fullerenes, some of which can be accomplished through quantum mechanical modeling of isomers for each cage size.

### **EARLY THEORY:**

The possible existence of fullerene type molecules was postulated theoretically by Osawa, Davidson and Jones, independently from one another, several years before the first experimental evidence for them was gathered.<sup>26-28</sup> Jones in particular asserted in 1966 the possibility that “graphite balloons” might be generated by modifying the procedure for high temperature graphite production.<sup>28</sup> Computational modeling of fullerene cages began as early as 1986 using fairly simple computational methods such as

the Hückel Model, MNDO (Modified Neglect of Differential Overlap)<sup>29</sup> and various other semi-empirical methods, primarily on the experimentally abundant C<sub>60</sub> I<sub>h</sub> and C<sub>70</sub> D<sub>5h</sub>.<sup>21,30-33</sup>

In the mid to late 1980s, *ab initio* computations on molecules of this size were still quite difficult from a computational standpoint,<sup>34,35</sup> but there were groups who had the resources and performed these computations. These computations were done using fairly small basis sets (STO-3G, 3-21G, etc) and were mostly intended to prove the possible existence of a C<sub>60</sub> I<sub>h</sub> molecule rather than compare the stability of one isomer to another.<sup>35,36</sup>

In the early 1990s, interest began growing in what is called the “higher fullerenes”, fullerene type molecules with more than 70 carbon atoms on the cage. Manolopoulos’s spiral algorithm<sup>19</sup> was used to generate possible structural isomers for these larger cage sizes and the Hückel Model was used to predict whether one isomer was more stable than the others in a particular isomeric set.<sup>37-39</sup>

Once lists of possible isomers for the higher fullerenes became available, efforts to predict the most stable isomer for each isomeric set intensified. In 1992, two groups, Raghavachari *et al.*<sup>40</sup> and Zhang *et al.*,<sup>41</sup> worked separately to determine by semi-empirical means the most stable isomer(s) of the C<sub>84</sub> cage. This case was particularly interesting because of the 24 possible IPR isomers for C<sub>84</sub>,<sup>39</sup> it seemed by NMR evidence that two or more must exist in the plasma-arc soot.<sup>25</sup> The two groups both came to the same conclusion that the two most energetically favorable isomers are nearly isoenergetic, a D<sub>2</sub> isomer and a D<sub>2d</sub> isomer.<sup>40,41</sup> Zhang’s paper was particularly important in that it was the first to report energy computations on a full isomeric set for a higher



fullerene with a non-trivial number of IPR isomers.<sup>2</sup> Later in 1992, another group (Bakowies *et al.*) built upon this work by modeling all 24 IPR isomers of C<sub>84</sub> using *ab initio* methods, which confirmed the findings of Zhang and Raghavachari.<sup>42</sup>

As stated earlier, C<sub>78</sub> is also prepared as an isomeric mixture of two or three isomers (depending on experimental parameters) in plasma-arc soot.<sup>23,24</sup> In 1992, Bakowies *et al.* performed *ab initio* computations on the five IPR isomers of C<sub>78</sub> and found two different nearly isoenergetic C<sub>2v</sub> isomers to be the most stable, followed closely by a D<sub>3</sub> isomer. These findings were in agreement with NMR studies discussed earlier in which Diederich's group found one C<sub>2v</sub> isomer and one D<sub>3</sub> isomer and Kikuchi found the same two isomers plus an additional C<sub>2v</sub> isomer.<sup>23,24</sup> It has been suggested that one of the C<sub>2v</sub> isomers, though energetically favored over the other C<sub>2v</sub> isomer and the D<sub>3</sub> isomer, is only kinetically favored under certain experimental conditions and was therefore not observed by Diederich's group.<sup>43</sup> These findings were later confirmed by Raghavachari and Rohlfing.<sup>44</sup>

For C<sub>76</sub>, there are three possible IPR isomers, but what makes C<sub>76</sub> an interesting case is that two of these are an enantiomeric pair of D<sub>2</sub> isomers (the third is a T<sub>d</sub> isomer that undergoes a Jahn-Teller distortion to a D<sub>2d</sub> conformation).<sup>37</sup> In 1992, Colt and Scuseria studied this smaller isomeric set using Hartree-Fock theory with the STO-3G basis set to confirm the stability of the D<sub>2</sub> enantiomeric pair in comparison with the T<sub>d</sub>→D<sub>2d</sub> isomer.<sup>45</sup>

## **INCORPORATION OF STATISTICAL MECHANICS:**

The computational background covered so far focused entirely on the electronic energy of each molecule while ignoring entropic effects. In 1979, Slanina began to apply

a computational method for comparing relative stabilities of isomers in isomeric systems to molecular clusters. This method incorporates all of the terms necessary to compare Gibbs free energies of the isomers, rather than just the electronic energies.<sup>46</sup> The procedure combined the use of quantum mechanical modeling with equations from statistical mechanics to give an equation for predicted mole fraction,  $w_i$ , as follows:

$$w_i = \frac{q_i \exp[-(e_{0,i} - e_0)/(kT)]}{\sum_{j=1}^m q_j \exp[(e_{0,j} - e_0)/(kT)]} \quad (1)$$

Where  $q_i$  is the product of translational, rotational and vibrational partition functions for the  $i^{\text{th}}$  isomer of an isomeric set and  $e_{0,i}$  is the ground state electronic energy of the  $i^{\text{th}}$  isomer of the isomeric set and  $e_0$  is the ground state electronic energy for some reference isomer. This equation can be rearranged and expressed in terms of Gibbs free energy values.

$$w_i = \frac{\exp[-\Delta G_i / (RT)]}{\sum_{j=1}^m \exp[-\Delta G_j / (RT)]} \quad (2)$$

$\Delta G_i$  is the difference between  $G_{0,i}$  for the  $i^{\text{th}}$  isomer and the  $G_{0,i}$  for some reference isomer, usually the isomer with the lowest  $G_{0,i}$ . Gaussian 03 calculates the electronic energy ( $E_{elec}$ ) and the nuclear repulsion energy ( $E_{nuclear}$ ) using the method specified in the input file and then automatically predicts the  $G_{0,i}$  term for each isomer when a frequency computation is requested. Several assumptions, summarized in the following derivation, are necessary in order to make this prediction.<sup>47</sup> Total energy is defined by the equation:

$$E = E_{elec} + E_{nuclear} + E_{vib} + E_{rot} + E_{transl} \quad (3)$$

where  $E_{elec}$ ,  $E_{nuclear}$ ,  $E_{vib}$ ,  $E_{rot}$ , and  $E_{transl}$  are the electronic, nuclear repulsion, vibrational, rotational and translational energies of the molecule. The rotational and translational energies are computed with the assumption that they are directly related to the Kelvin temperature:<sup>48</sup>

$$E_{rot} = E_{transl} = \frac{3}{2}kT \quad (4)$$

$e_{0,i}$  from equation 1 can be represented as:

$$e_{0,i} = E_{elec} + E_{nuclear} \quad (5)$$

Vibrational frequencies are computed by taking the second derivatives of the quantum mechanical energies with respect to the Cartesian coordinates for each nucleus, and then converting those coordinates to mass weighted coordinates for the purpose of calculating the frequencies using harmonic approximation.<sup>49,50</sup>

$G_0$  and  $H_0$  are defined by:

$$G_0 = H_0 - TS_0 \quad (6)$$

And

$$H_0 = E + PV \quad (7)$$

Combining equations (3) through (7) we get:

$$G_0 = e_{0,i} + E_{vib} + E_{rot} + E_{transl} + PV - TS_0 \quad (8)$$

Making the ideal gas assumption that

$$PV = NkT \quad (9)$$

Where N is equal to one molecule, giving:

$$G_0 = e_{0,i} + E_{vib} + E_{rot} + E_{transl} + kT - TS_0 \quad (10)$$

The molecules being studied are solid at the temperature being assumed in the computations (298.15K), so the ideal gas law assumption is not valid. But since the error would be about the same for each isomer, the error introduced will be subtracted out when  $\Delta G_{0,i}$  are calculated.  $S_0$  for each isomer is calculated using standard statistical mechanical thermodynamic connection formulas that can be found in statistical thermodynamics texts like those by McQuarrie<sup>48</sup> or Nash.<sup>51</sup> A spreadsheet can be constructed using the same formulas from McQuarrie's text used for the entropic terms providing  $G_{0,i}$  for each isomer at various temperatures.

Slanina first applied this procedure to fullerenes in 1987 when he calculated  $G_{0,i}$  for C<sub>60</sub> I<sub>h</sub> and C<sub>70</sub> D<sub>5h</sub> at a range of temperatures from 298 K to 5000 K and pressures from 2.113X10<sup>-7</sup> atm to 10<sup>5</sup> atm, using a variety of semi-empirical methods, in an effort to determine whether the percentage of each fraction in the plasma-arc soot was dependent on the temperature and pressure of the plasma-arc chamber.<sup>52</sup>

In 1993, Slanina's group applied this method to compare the relative stabilities of all five IPR isomers of C<sub>78</sub> for the purpose of finding the temperature dependence on the predicted equilibrium mole fraction of each isomer. Their work demonstrated that the differences in composition found between the original experiments of Diederich *et al.*<sup>23</sup> and Kikuchi *et al.*<sup>24</sup> (vide supra) were more likely due to a thermodynamic effect than a kinetic effect as the semi-empirical computations showed that the thermodynamic properties of several of the isomers are significantly temperature dependent.<sup>53</sup>

In 1995, Slanina applied this same technique to the 24 IPR isomers of C<sub>84</sub> in an effort to show the temperature dependence on the relative stabilities of the isomers as it relates to their chirality.<sup>54</sup> Slanina's group modeled the 24 isomer IPR C<sub>84</sub> set in two

different ways. In the first set of computations, they modeled the set as 35 different isomers, 13 achiral isomers and 11 enantiomeric pairs. In the second set of computations they ignored one enantiomer from each pair, accounting for only 24 isomers.

They found that accounting for chirality effects does make a significant difference in the predicted temperature dependence of thermodynamic isomeric stability. The computations accounting for chirality gave much closer agreement with the 2:1 ratio between isomers the  $D_2$  and  $D_{2d}$  isomers shown by NMR evidence.<sup>24,25</sup> In this same study, they also reported that the most stable  $C_{84}$  isomer varied significantly with temperature.

In 1996, Slanina's group modeled all seven IPR isomers of  $C_{80}$ , which had not yet been isolated in experiment, using semi-empirical techniques.<sup>55</sup> In this work, they found the most stable isomer to be dependent on temperature.  $C_{80}$  electronic structure had been previously studied in all seven IPR isomers by Nakao *et al.* using *ab initio* methods, but they had ignored temperature and entropic effects.<sup>56</sup> In 1997, Slanina again reported on  $C_{80}$  ( $C_{86}$  and  $C_{88}$  were covered in the same paper) using *ab initio* methods as high as HF/4-31G to confirm their previous work.<sup>57</sup> The  $C_{80}$  isomeric set presents an interesting case for future study that will be developed later in this work, in that the isomers predicted by both Slanina's and Nakao's groups to be most stable are not the ones found in tri-metal nitride templated (TNT) endohedral metallo-fullerene (EMF)  $C_{80}$  such as  $Sc_3N@C_{80}$ .<sup>58</sup>

In 2003, Slanina used the same Gibbs free energy based, temperature dependent means to computationally study the 20 most stable of the 134 IPR isomers of  $C_{94}$ .<sup>59</sup> That same year, his group published another paper presenting a semi-empirical treatment of all

134 IPR isomers of  $C_{94}$  and *ab initio* treatment (HF/4-31G) of the 20 most stable IPR isomers.<sup>5</sup> These two publications agreed with experimental results for the four most stable empty cage  $C_{94}$  isomers.<sup>3,4</sup> This case again presents an interesting future study in that when the EMF  $Ca@C_{94}$  was later isolated, the geometry found for that cage was the one ranked 76<sup>th</sup> most stable by Slanina's group.<sup>60</sup> This case will also be discussed in more detail later in this document.

Although Slanina had previously ignored excited state contributions, which could be important at the elevated temperatures associated with the plasma-arc synthesis method for fullerenes, in their relative stability computations, the Slanina group reinvestigated the  $C_{78}$  isomeric set using their Gibbs free energy approach with semi-empirical methods, but this time accounting for excited states using the ZINDO method, in a paper published in 2004.<sup>61</sup> However, there was almost no difference in the relative stabilities calculated at low temperatures when accounting for excited states of the  $C_{78}$  isomers as opposed to ignoring the excited states. There was a noticeable difference at higher temperatures, but still only marginally significant at best.

In 2006, Slanina's group added the excited state energies to the partition function for the  $C_{80}$  isomers and noticed a more significant difference in predicted equilibrium mole fraction at higher temperatures than they did in the  $C_{78}$  case.<sup>62</sup> One possible reason for this is that the dominant species in the  $C_{78}$  case are significantly more stable than the  $C_{80}$  isomers and the lower band gap for the  $C_{80}$  species gives rise to a higher probability for excited state population.<sup>63</sup> Slanina postulated that these effects may even be more significant in endohedral metallo-fullerenes.<sup>62</sup>

## ENDOHEDRAL METALLO-FULLERENES (EMF):

Kroto and Smalley's original 1985 paper, introducing the first experimentally produced fullerenes, suggested that the width of the interior of the  $C_{60}$  cages was sufficient (on the order of 7 Ångstroms) to allow for the insertion or enclosure of other atoms.<sup>14</sup> Later that same year, this group introduced the first endohedral metallofullerene (EMF), a  $C_{60}$  cage with a lanthanum atom inside of the cage, as well as several other larger cages, each containing one lanthanum atom.<sup>64</sup> This finding was later reproduced on a larger scale with the finding that  $La@C_{82}$  was particularly stable.<sup>65</sup>  $La@C_{82}$  was produced on the milligram scale the following year and characterized by mass spectrometry and EPR.<sup>66</sup> Over the next couple of years, advances were made in generating measurable quantities of EMFs containing one or more metal atoms including lanthanum, yttrium, scandium, potassium and many others.<sup>67</sup>

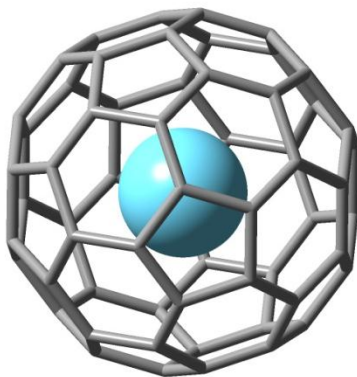


**Figure 9: Model of  $La@C_{60}$  using van der Waals radius for lanthanum.**

In 1999, the Dorn group at Virginia Tech introduced a new type of EMF that they dubbed the “trimetallic nitride templated” (TNT) fullerene. This consists of a fullerene cage,  $C_{80}$  or larger, containing a trigonal planar complex of three metal atoms and one nitrogen atom. The first experimentally produced TNT was  $Sc_3N@C_{80}$ . The

experimental procedure used to generate TNTs was similar to that used to generate other EMFs with the exception that a small amount of nitrogen gas is mixed with the helium usually found in the reaction chamber.<sup>58</sup> TNTs, in particular  $\text{Gd}_3\text{N@C}_{80}$  and  $\text{Lu}_3\text{N@C}_{80}$  have become of increasing interest because of their unique magnetic properties and possible medical uses.<sup>68-76</sup>

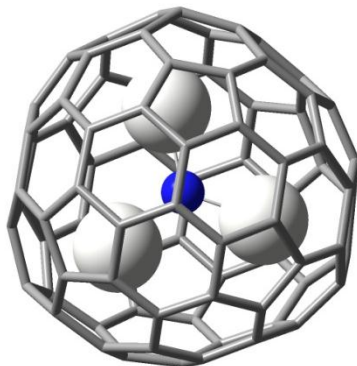


**Figure 10: Model of  $\text{Sc}_3\text{N@C}_{80}$  using van der Waals radii for scandium and nitrogen.**

Modeling of EMFs is significantly more complicated than empty cage modeling for several reasons. First of all, EMFs do not always follow the isolated pentagon rule.<sup>77</sup> For larger cages this can increase the number of possible isomers to be investigated by a significant number. It appears that electrons transfer from the metal to the cage, giving the cage a net negative charge. If a particular isomer has an open-shell configuration, adding electrons to the cage could fill in the empty orbitals in the open-shell, closing the shell and stabilizing the molecule. Conversely, when electrons are added to a cage that has a closed-shell configuration, those electrons would add to a higher open-shell, destabilizing the molecule..<sup>78</sup>

Another complication of modeling EMFs is the presence of the metal itself. Basis sets that model carbon fairly accurately are not always reliable for metals, particularly larger metals like transition metals and lanthanides.<sup>79</sup> Manolopoulos and Fowler proposed



a method for overcoming this problem in 1991 when they began to model the dianions of the IPR isomers of all of the cages between  $C_{70}$  and  $C_{90}$ .<sup>80</sup> In this work, they show that each charged fullerene  $C_n^{2-}$  where  $n$  is an even number between 70 and 90 has at least one closed shell IPR isomer. These computations (performed at the Elementary Hückel level of theory) predicted the correct isomer for even more charge (3-) cage of the  $La@C_{74}$  and  $La@C_{82}$  molecules that had been previously isolated and characterized.<sup>81</sup>

As early as 1998, *ab initio*, density functional theory (DFT) computations of relative stabilities for EMFs were reported by Kobayashi and Nagase involving  $M@C_{82}$  ( $M = Sc, Y, La, Ce, Pr, Eu, Gd, Yb, Lu$ ).<sup>82</sup> In order to perform these computations, they had to find a basis set capable of handling the lanthanides with partially filled  $f$  orbitals. For the lanthanide atoms, “effective core potential” (ECP) basis sets developed in 1993 by Cundari and Stevens were used.<sup>83</sup> Lanthanide basis set development has advanced significantly since that time,<sup>84,85</sup> but the predictions given then seem to match experimental results that were being reported, namely that the  $C_{2v}$  IPR  $C_{82}$  isomer was favored in the  $M@C_{82}$  rather than the  $C_2$  isomer that was favored in the empty cage.<sup>82</sup> In 2004, Senapati *et al.* performed more detailed computations on the  $C_{2v}$  isomer of  $Gd@C_{82}$  with the hopes of gaining a better understanding of its electronic transport properties.<sup>86</sup> In this case, the CEP-121G<sup>87</sup> basis set was used for gadolinium and the results of the computation were in satisfactory agreement with experiment.<sup>86</sup>

In 2001, Slanina’s group applied their Gibbs free energy based, temperature dependent method for predicting the most stable isomer to  $Mg@C_{72}$  using the MNDO/d technique.<sup>88</sup> Four isomers were studied; the only IPR isomer for  $C_{72}$ , two selected fused pentagon isomers, and an isomer with one heptagon. Near room temperature, the model

predicted only the IPR isomer in significant mole fractions, however, at temperatures above 3000 K, the two fused pentagon isomers were more significant than the IPR isomer. Slanina later repeated these computations at the higher CIS level of theory using the LanL2MB and the LanL2DZ basis sets while also accounting for excited states in the computation of the partition function. The results found were close to those found in his 2001 paper.<sup>61</sup>

In 2004, Slanina's group also modeled the nine IPR isomers of Ca@C<sub>82</sub> using their Gibbs free energy, temperature-dependent method. In this case they accounted for excited states, for comparing relative stabilities of isomers. They used the B3LYP density functional and the 6-31G\* basis set for energetic, and B3LYP density functional with the 3-21G basis set for entropy.<sup>89</sup> This was an intriguing task because of the number of possible IPR (nine) isomers and the number of already known isolated isomers from experiments (four). Slanina's group's predicted four of the nine possible IPR isomers to be more stable than the other five, which agreed with experimental findings of Shinohara's group in 1996.<sup>90</sup> Shinohara's group had found these four isomers in nearly equimolar amounts, consistent with Slanina's predictions for very high temperatures. These results were compared with computations on La@C<sub>82</sub> at the same levels of theory in a paper by Slanina the next year.<sup>91</sup> While low temperature results were very similar between the lanthanum case and the calcium case, higher temperature models showed that the lanthanum atom (a +3 oxidation state) stabilizes the cages differently relative to the calcium atom (a +2 oxidation number), in particular, the C<sub>3v</sub> isomer is predicted to be much more populated in the lanthanum case at higher temperature than it was in the calcium case.

In 2005, Slanina used his Gibb's free energy based, temperature dependent model to investigate trimetallic nitride templated (TNT) fullerenes for the first time, focusing on the  $\text{Sc}_3\text{N}@C_{80}$  molecule.<sup>92</sup> This was an interesting study case since of the seven possible IPR isomers for the cage, only two had been isolated so far: the  $I_h$  isomer,<sup>58</sup> and the  $D_{5h}$  isomer.<sup>93</sup> Furthermore, an experimental equilibrium mole fraction was fairly well established with the plasma-arc soot  $\text{Sc}_3\text{N}@C_{80}$  fraction being approximately 83%  $I_h$  cage and 17%  $D_{5h}$  cage.<sup>94</sup> According to Slanina's temperature-dependent findings, this mole fraction is achieved at approximately 2450 K. However, the predicted mole fraction is 50%  $I_h$  cage and 50%  $D_{5h}$  cage at a temperature of approximately 4000 K and the  $D_{5h}$  cage is predicted to be more stable than the  $I_h$  cage at higher even temperatures.<sup>92</sup> If kinetic effects are not important, one could predict the mole fraction of products for some TNTs by controlling the temperature inside the arc through manipulation of voltage, current and the pressure and character of the inert gas.

In 2006, Slanina's group used this same technique to investigate  $\text{La}_2@C_{72}$  and  $\text{Sc}_2@C_{72}$ .<sup>95</sup> The notable feature of this case is that  $C_{72}$  had not yet been found in experiment in the empty cage form and previous computations suggested that a non-IPR isomer (one with two fused pentagons) is more stable than the lone IPR isomer.  $\text{La}_2@C_{72}$  was isolated for the first time in 1998,<sup>96</sup> and characterized by NMR for the first time in 2003, 18 lines were found in the  $^{13}\text{C}$ -NMR spectrum consistent with a  $D_2$  geometry for the cage.<sup>97</sup> The lone IPR isomer for  $C_{72}$  has a theoretical symmetry of  $D_{6d}$  which is capable of Jahn-Teller distortion to  $D_2$ . There are also 38 non-IPR, fused-pentagon isomers of  $C_{72}$  that are either  $D_2$  in their theoretical structure, or are capable of Jahn-Teller distortion to  $D_2$ .<sup>2</sup> Slanina's group then modeled all 39 of these isomers, but in

order to avoid the complexities caused by modeling lanthanum atoms, they modeled empty cages with a 6- charge on each, assuming that the only significant contribution from each lanthanum (or scandium) atom to the stability of the cage is the three valence electrons each atom will contribute.<sup>77,95</sup> Using this approach, Slanina's group was able to predict a non-IPR geometry for  $\text{La}_2@C_{72}$  without modeling the lanthanum atoms, then confirm that geometry by remodeling only the highest stability isomers with lanthanum atoms included.<sup>95</sup>

Slanina postulated that the reason fused-pentagon isomers could be found in EMFs is that the addition of electrons to the cage would allow the anti-aromatic (8  $\pi$  electrons) fused pentagon pair to become aromatic (10  $\pi$  electrons) by absorbing two of the donated from the metal atom(s) (see **Figure 11** below).<sup>95</sup>

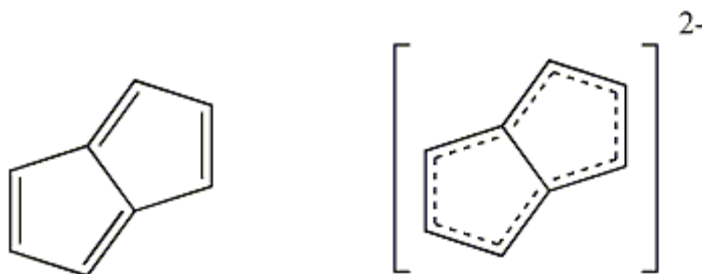


**Figure 11. Anti-aromatic fused pentagons, aromatic fused pentagons with 2- charge**

#### **USE OF DENSITY FUNCTIONAL THEORY FOR FULLERENE MODELING:**

It is worth noticing that most of the modeling of fullerenes and EMFs published in the last fifteen years, including the work contained in this dissertation, utilizes density-functional theory (DFT), which seeks to overcome the electron correlation problem by approximating all of the electron correlation terms with one simple three-dimensional electron exchange-correlation functional.<sup>98,99</sup> The key to the success or failure of a

particular DFT method lies in the accuracy of the assumptions and approximations involved in the electron exchange-correlation function for the system in question.<sup>100</sup> A successful DFT method can model a particular system with accuracy better than Hartree-Fock method, and similar to Møller-Plesset perturbation theory, but with computational time cost similar to that of Hartree-Fock theory and significantly less expensive than Møller-Plesset perturbation theory.<sup>101</sup>

Most of the computations in this dissertation employ the B3LYP density functional.<sup>102,103</sup> B3LYP is the most commonly used DFT method both for general systems and for fullerene systems, having represented over 80% of the total occurrences of density functional theory in the literature during the time period from 1990-2006.<sup>101</sup> Despite new density functionals being reported in the literature each year, B3LYP's popularity has not waned. B3LYP is a hybrid generalized gradient approximation (H-GGA) density functional. The generalized gradient approximation (GGA) improves on the Local density approximation (LDA) by including a term to compute the gradient of the density at each point. Combining the electron-correlation of a GGA method with a percentage of the Hartree-Fock exchange (20% in the case of B3LYP) leads to the even more improved accuracy of the H-GGA methods like B3LYP.<sup>102</sup>

While B3LYP is the most popular, and one of the most accurate of the DFT methods,<sup>104</sup> it can suffer from inaccuracies where non-bonded interactions are concerned as in the cage cluster interactions in fullerenes that encapsulate an atom or cluster of atoms.<sup>101</sup> While this limitation has been difficult to improve upon, Slanina reported some success in 2006 using the new MPWB1K<sup>105</sup> density function on C<sub>60</sub> encapsulating H<sub>2</sub>, N<sub>2</sub> or Ne. He found that the MPWB1K density functional was more successful at modeling

non-bonding interactions such as are found between the cage and the enclosed species in EMFs.<sup>106</sup> The belief is that quite often in EMFs, the distance between the cage and the encapsulated complex is too far for B3LYP to accurately model the interaction. This causes an underestimation of the energy of encapsulation.<sup>107</sup> In 2008, Slanina's group revisited the  $\text{Li}_x@C_{60}$  molecules using the MPWB1K density functional to improve upon the accuracy of their previous work on that system.<sup>105</sup>

Modeling EMFs can be even further complicated by the identity of the metal. Several of the most important EMFs contain atoms with unpaired  $f$  electrons (like gadolinium with seven unpaired  $f$  electrons) which are not well treated by standard density functionals like B3LYP.<sup>108</sup> Success has been found in treating EMFs containing these kinds of atoms with the PBE0 functional<sup>109-111</sup> (also called PBE1PBE) with effective core potential basis sets like CEP-121G.<sup>83,87,112,113</sup> This method is used on all EMFs in this dissertation containing one or more lanthanide atoms in the endohedral cluster.

### **THE FORMATION OF FULLERENES AND EMFs:**

Beginning in 1995, Maruyama's group at the University of Tokyo examined theoretical approaches for studying how fullerenes form in the plasma arc or laser vaporization synthesis.<sup>114</sup> Molecular dynamics simulations were performed beginning with a group of 200 randomly distributed isolated carbon atoms at controlled temperature of 3000 K using an empirical function proposed by Brenner in 1990.<sup>115</sup> The simulation produced an imperfect fullerene cage of 70 carbons that formed from intermediates of between  $C_2$  and  $C_{10}$  chain length, mono-cyclic rings of  $C_{10}$ - $C_{15}$  and polycyclic clusters of

$C_{20}$ - $C_{30}$ . But the resulting imperfect cluster did not reorganize to the experimentally realized  $C_{70}$ - $D_{5h}$  cage.

In 1998, Maruyama *et al.* improved on this result by performing a molecular dynamics simulation using the same empirical function as above, but allowing the imperfect  $C_{60}$  and  $C_{70}$  fullerene-like clusters generated to anneal at 2500 K in the absence of intermolecular collisions.<sup>116</sup> During the simulations, a series of Stone-Wales transformations allowed the formation of both the  $C_{60}$ - $I_h$  and the  $C_{70}$ - $D_{5h}$  cage structures. That same year, they showed by molecular dynamics simulation that allowing a reaction of the same type, but at a lower temperature than 2500 K caused flat graphitic sheets to form rather than fullerenes.<sup>117</sup>

## CHAPTER 2: C<sub>94</sub> DIELECTRON AFFINITIES

### CONTRIBUTIONS:

This chapter represents work that has not yet been published focusing on the relative stabilities of the C<sub>94</sub><sup>2-</sup> anion IPR isomeric set compared to the neutral molecules of the same set. Contributions to this chapter are as follows: Tim Fuhrer (author of this dissertation) performed all computational work and all writing in the manuscript.

### INTRODUCTION:

The C<sub>94</sub> fullerene cage has 134 IPR isomers.<sup>2</sup> Slanina's treatment of this isomeric set (discussed earlier in this work) found the C<sub>2</sub> isomer (called number 133 by Fowler<sup>2</sup>) to be the most stable for the empty cage neutral species.<sup>5</sup> Experimental isolations of Ca@C<sub>94</sub> and Tm@C<sub>94</sub> have shown that the so-called isomer number 134, the only C<sub>3v</sub> IPR isomer for C<sub>94</sub>, is the one found for C<sub>94</sub> EMFs.<sup>60</sup> This C<sub>3v</sub> isomer was found, however, to be only the 76<sup>th</sup> most stable IPR isomer for the neutral empty cage.<sup>5</sup>

This has led to an interesting computational question: Why is it that there is often a different cage isomer favored for EMFs than for empty cages of the same size? Modeling EMFs including the encapsulated atom(s) for an isomeric set as large as the C<sub>94</sub> set will likely be very time consuming, particularly if done at a sufficient basis set and density functional to accurately model the interactions between the cage and the encapsulated atom(s).<sup>118</sup> Previous computations by Slanina's group on five C<sub>72</sub><sup>6-</sup> ions and five La<sub>2</sub>@C<sub>72</sub> isomers have suggested that the main reason for this change in stability is the electron transfer from the encapsulated metal atoms to the cage and they proposed that the fused pentagon is stabilized by the addition of a pair of electrons, altering the character of that group from anti-aromatic to aromatic (see **Figure 11** above).<sup>95</sup>



The fact that a different  $C_{94}$  IPR isomer is the most stable in the neutral cage from the one that is most stable in the dianion that we would find in the case of  $Ca@C_{94}$  and  $Tm@C_{94}$  shows that the fused pentagon motif is not the only one stabilized by the addition of a pair of electrons from an encapsulated metal. Full treatment of the 134 IPR isomers of the  $C_{94}^{2-}$  ions will lead to a deeper understanding of the reasons for these differences in stabilities between empty cage and EMF isomers. For example, an extension of the isolated pentagon-rule that has been proposed is that fullerene cages will have the most stable structure when pentagons are located as far apart as possible. The reason for this is thought to be that the closer pentagons are together on the cage, the more strain they induce.<sup>20</sup> However, another possible reason for stability increasing as pentagons are further separated may be that pentagons as near neighbors create regions of local anti-aromaticity.

The fusing of two pentagons with the same hexagon, whether they are para to one another (**Figure 12a**) or meta to one another (**Figure 12b**), creates another region of anti-aromaticity (twelve  $\pi$  electrons) in the neutral case and aromaticity (14  $\pi$  electrons) in the di-anion case.

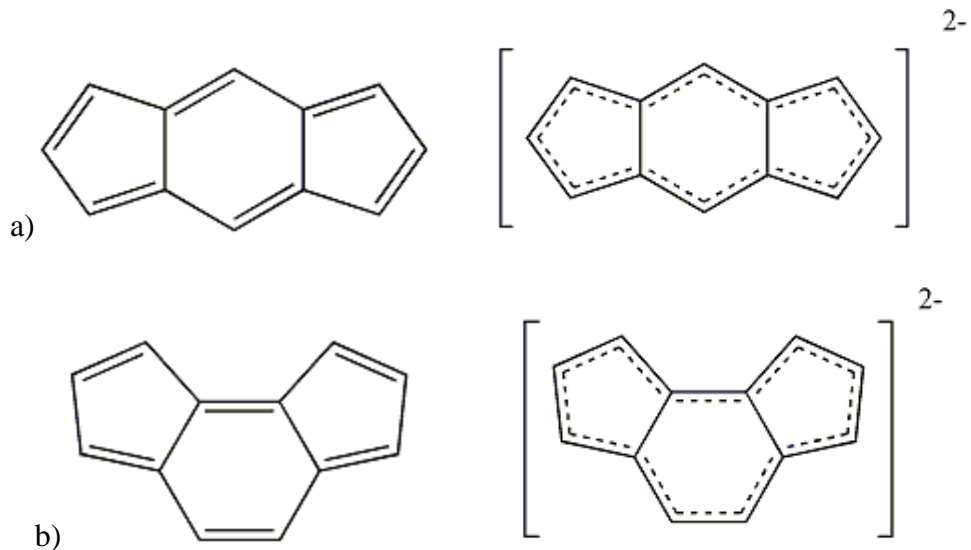


**Figure 12. Anti-aromatic neutral bonding motifs and aromatic di-anion bonding motifs**

Modeling of all 134 di-anion IPR isomers of  $C_{94}$  using Slanina's Gibbs free energy, temperature dependent method,<sup>46</sup> and counting the number of the above motifs found on each isomer would provide evidence in support of or against this hypothesis.

A different, more localized view of the bonding on a fullerene shows all bonds on any IPR fullerene as being one of four types; a) fusing two hexagons and connecting two hexagons, b) fusing two hexagons and connecting two pentagons (the so-called "pyracylene" motif), c) fusing two hexagons and connecting a hexagon to a pentagon, and d) fusing a hexagon to a pentagon and connecting two hexagons (see **Figure 13** below where each bond being described is highlighted in bold).

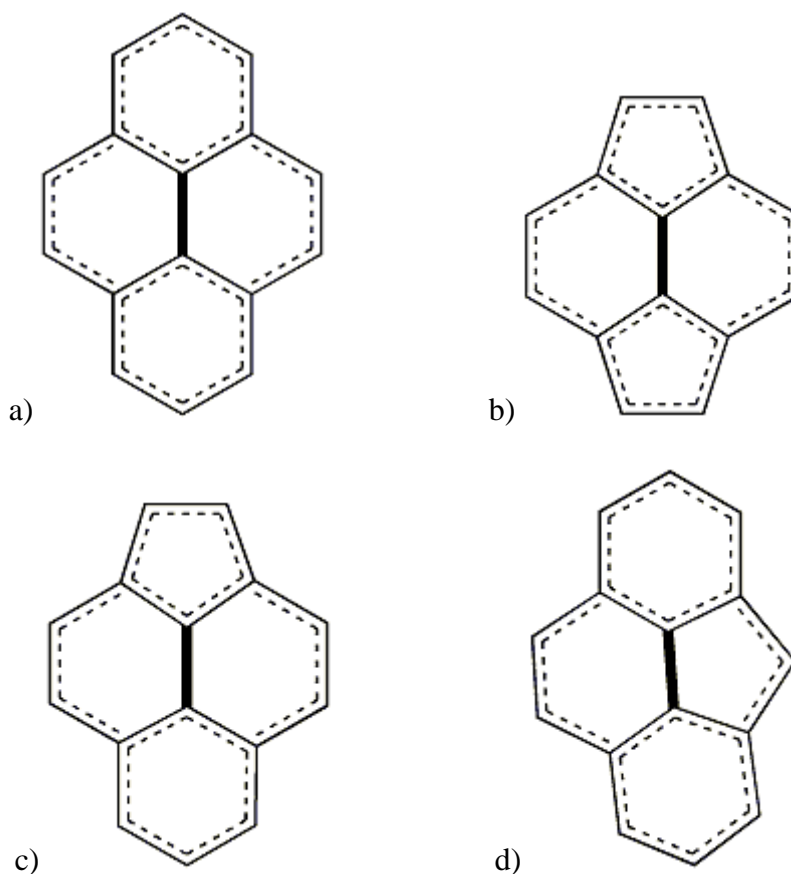


**Figure 13: Four different bonding motifs for IPR fullerenes**

Our hypothesis is that there is a slightly simpler approach to this problem. Our results will show that added electron density has a tendency to accumulate on pentagon carbon atoms rather than on carbon atoms that are on hexagons only. This makes sense given that a neutral pentagon would have five *pi* electrons, and therefore a pentagon with one added electron would have six *pi* electrons and therefore be aromatic. As a result, pentagons on fullerene anions repel each other electrostatically making isomers with pentagons further apart more stable than those with pentagons as near neighbors.

#### **COMPUTATIONAL METHODS:**

All 134 IPR isomers of the  $C_{94}^{2-}$  cage were modeled via density functional theory. To generate suitable starting coordinates, the geometries of each IPR isomer were

optimized using the AM1 semi-empirical quantum mechanical method. Each isomer's geometry was then further optimized using the B3LYP density functional and the 3-21G basis set. B3LYP is the most popular of all density functional for modeling systems of this size and is known to be particularly accurate, especially in cases like this where an endohedral metal atom is not being considered.<sup>101</sup> The 3-21G basis set is admittedly small and more accuracy could likely have been obtained using a larger basis set, but that would have amounted to a huge increase in computational time cost because of the large number of isomers (134, each having 94 atoms) needing to be modeled.

As a calibration test for this method, energies for the five most energetically favorable C<sub>94</sub> dianion models were computed both at a higher basis set (6-31G\*) with the B3LYP functional, and with several other functionals using the 3-21G basis set. Results were qualitatively similar for each method tested. The data is summarized in table below:

<b>Isomer #</b>	<b>B3LYP/321G</b>	<b>B3LYP/6-31G*</b>	<b>BLYP/321G</b>	<b>BPW91/321G</b>
<b>124</b>	0.00	0.00	0.00	0.00
<b>132</b>	5.81	4.51	3.04	2.87
<b>134</b>	9.92	9.65	9.53	8.59
<b>118</b>	15.04	14.28	11.17	11.10
<b>75</b>	17.63	23.05	16.81	16.02

**Table 1: Relative energies computed for the five most stable isotopes of the C<sub>94</sub> dianion using four different model chemistries.**

Once the geometry of each isomer had been optimized, a vibrational frequency analysis was performed on each to assure that each geometry was in fact a minimum on its potential energy hypersurface rather than a saddle point. Optimized geometries with imaginary frequencies were reoptimized either using tighter convergence criteria, or from

an adjusted starting geometry in order to find an optimized geometry with no imaginary vibrational modes, thus resolving all the imaginary frequencies found.

The energies computed for each optimized isomer were used to confirm that the charge difference on the cage is the reason for the difference in stability between the empty cage  $C_{94}$  and the  $C_{94}$  EMFs. We also modeled all 134 neutral cages for comparison using exactly the same methods and model chemistries described in the paragraphs above. These energies combined with those from the  $C_{94}^{2-}$  anions then allowed us to compute the “dielectron affinity”, the energy associated with adding two electrons to the neutral molecule, for each cage. Once the dielectron affinities were calculated for all 134 IPR isomers, we compared these energies to the numbers of pyracylene bonding motifs (see **Figure 13b**) as well as the number of pentagons with para-fused-hexagons (see **Figure 12a**) in an effort to find a link between the prevalence of either of these motifs and the dielectron affinity of each isomer. The Gaussian 03 modeling software package was used for all computations.<sup>47</sup>

## RESULTS AND DISCUSSION:

The  $Ca@C_{94}$  and  $Tm@C_{94}$  reported by the Dorn group was the  $C_{3v}$  isomer called number 134 by Fowler’s book (see **Figure 1** on page 1).<sup>2,60</sup> Slanina found this isomer to be the 76<sup>th</sup> most stable in the neutral empty cage.<sup>5</sup> Our calculations predict this isomer to be the 3<sup>rd</sup> most stable in the dianion form, about 9.9 kJ/mol less stable than the predicted most stable isomer (see **Appendix 1**).

A plot of the average energy change resulting from the addition of two electrons to the neutral cage (the *dielectron affinity*) versus the number of pyracylene bonding

motifs on each isomer shows a trend that suggests that the pyracyclene motif in some way destabilizes the addition of electrons to the cage (see **Figure 14** below). However, there is a wide variance in dielectron affinities within each group (see graph of complete data in **Appendix 5**) showing that pyracyclene motifs on the cage is not the only important criteria for determining the dielectron affinity of a fullerene isomer.

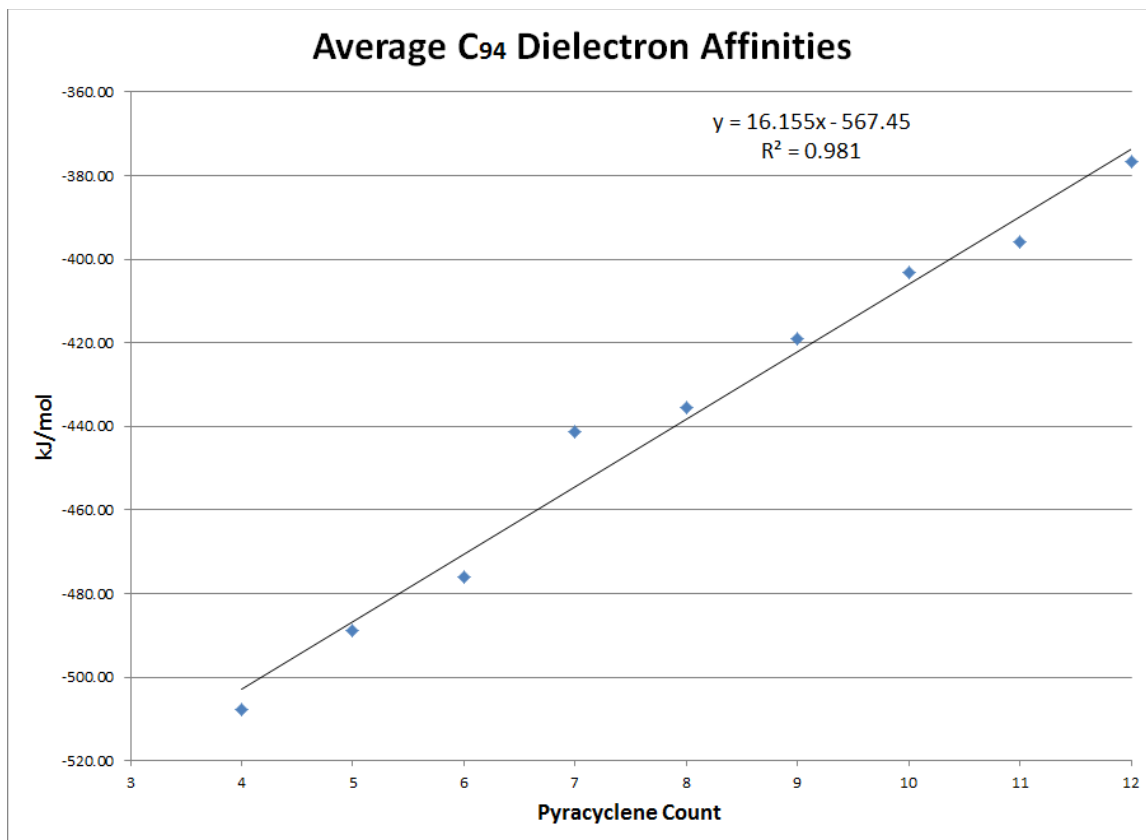


**Figure 14: Average C<sub>94</sub> Dielectron Affinities computed at the B3LYP/3-21G level of theory vs. number of para-fused-pentagons.**

**Figure 15** shows that there is also a correlation between the average dielectron affinities for the C<sub>94</sub> isomers and the number of hexagons with para-fused-pentagons. There is also a great variance among the dielectron affinities within each para-fused-pentagon number group (see **Appendix 5** for complete data) demonstrating that the number of para-fused

pentagons on a surface, while important, is not the only important factor in determining the dielectron affinity of a fullerene isomer.

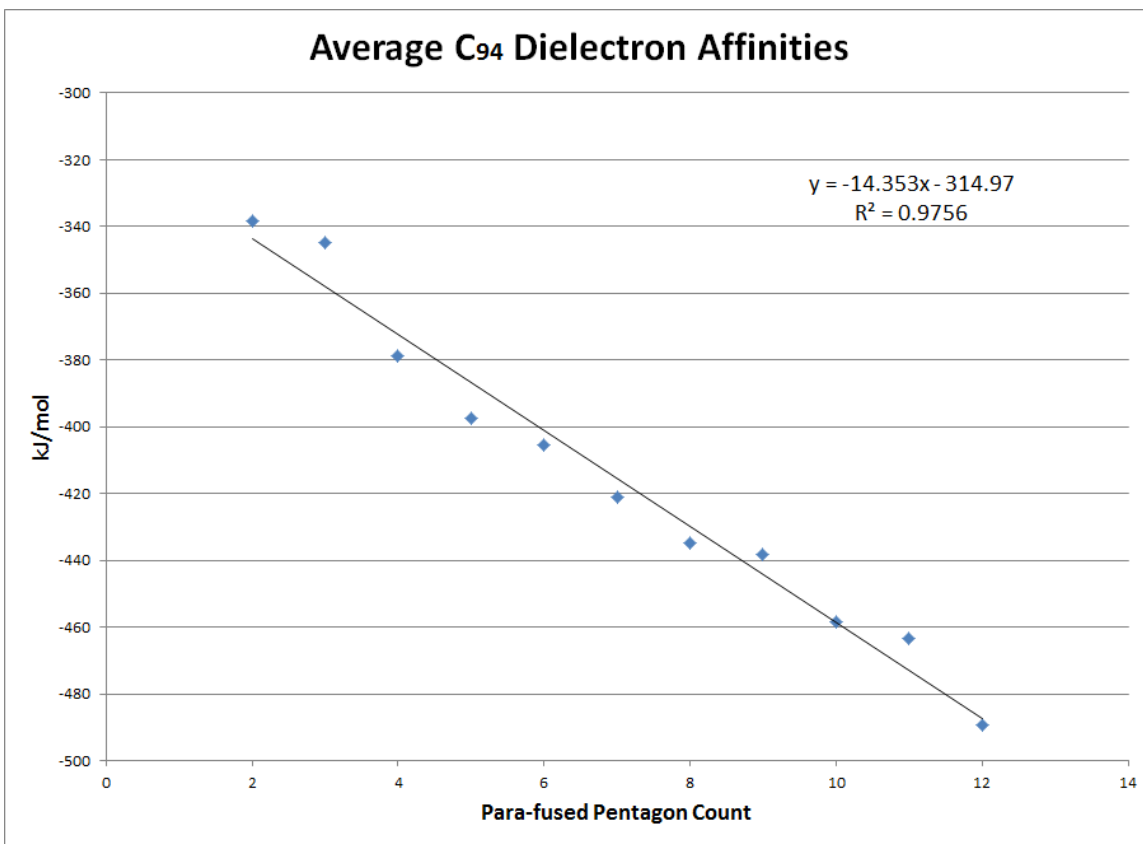


**Figure 15: Average  $C_{94}$  Dielectron Affinities computed at the B3LYP/3-21G level of theory vs. number of para-fused-pentagons.**

A plot of the HOMO for  $C_{94}^{2-}(I34)$  (**Figure 16** below) gives some insight into the reason for this phenomenon. The figure shows a plot of the HOMO-1 and HOMO orbitals, which form a degenerate pair, for the  $C_{94}^{2-}(I34)$  isomer looking down through its  $C_{3v}$  symmetry axis. Six of the twelve pentagons are visible from the top at this angle. Each of those pentagons are pyracyclene bonded to the next forming a belt around the top hemisphere of the molecule. There is very little contribution to either the HOMO or the HOMO-1 orbital from the pyracyclene atoms. Both of these orbitals have their most significant contributions from the other side of the molecule where each pentagon is

separated from the next by a hexagon in the “para-fused-pentagon” motif described above.  $C_{94}^{2-}$  IPR isomers with a larger number of pyracyclene bonds and a smaller number of para-fused-pentagon motifs will have more and more localized HOMO orbitals and therefore be less stable than their counterparts with less pyracyclene bonds and more para-fused-pentagon motifs.

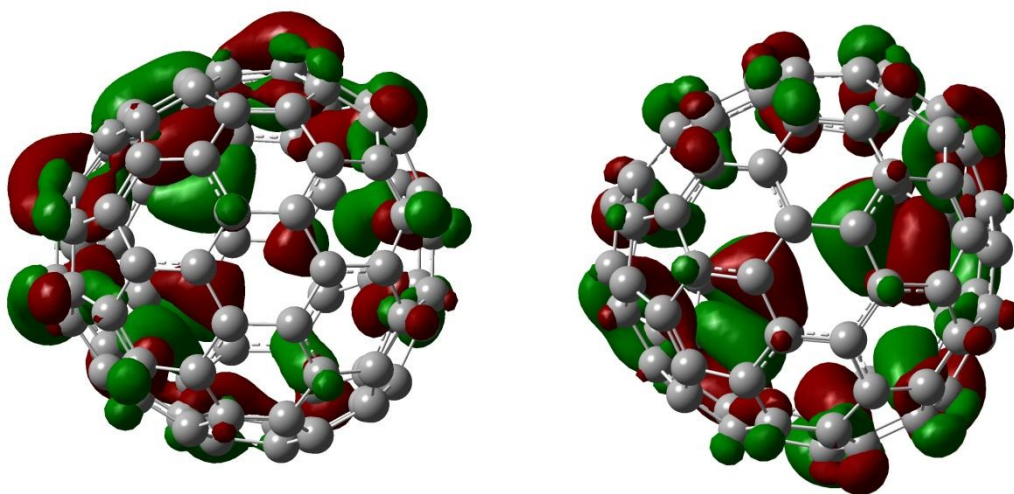


**Figure 16: HOMO-1 and HOMO for  $C_{94}^{2-}(134)$ .**

A plot of the LUMO for  $C_{94}^{2-}(134)$  looking down through the  $C_{3v}$  axis is shown in **Figure 17** below. The LUMO orbital is non-degenerate and has a significantly higher energy than the degenerate HOMO-1 and HOMO pair (6.3 kJ/mole). This higher energy orbital does contain contributions from the pyracyclene bonded carbons, which destabilize it giving it its higher energy.



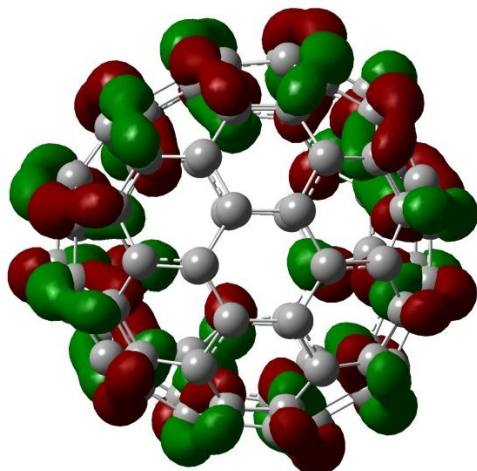


**Figure 17:** LUMO  $C_{94}^{2-}(134)$ .

What we have not yet determined is whether the differences found in stability among the  $C_{94}$  IPR dianions is caused by a tendency for electrons to collect on para-fused-pentagon motifs to form an aromatic region, or to avoid pyracylene motifs and the anti-aromaticity they might cause, or simply electrostatic repulsion between negatively charged pentagons that are each their own region of aromaticity. **Figure 18** (below) shows a visual representation of the Mulliken charge analysis of  $C_{94}^{2-}(134)$  from two different viewpoints with atoms that are more negatively charged shown in red, and atoms that are less negatively charged shown in green. This gives us a more detailed picture of where on the surface of the cage the added electron density collects.

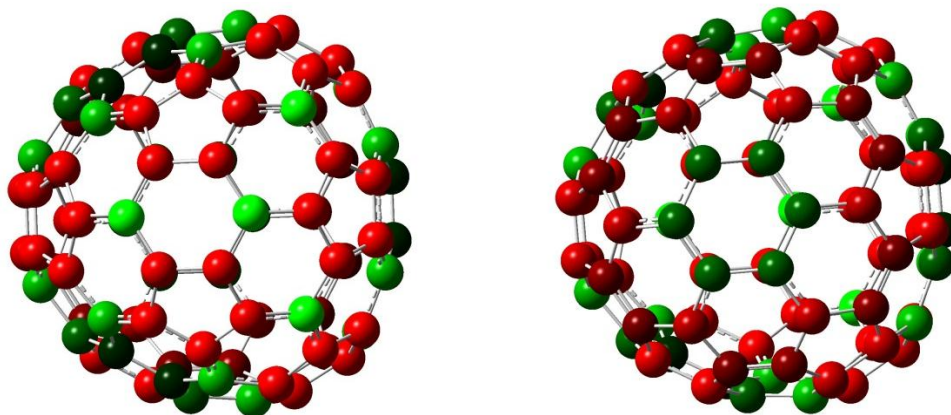


Figure 18: Mulliken charge analysis of  $C_{94}^{2-}(I34)$ . More negatively charged atoms shown in red.

Negative charge density is clearly more significant on atoms that are involved in pentagons, regardless of their extended motif (pyracyclene or para-fused-pentagon).

## CONCLUSION:

Computational evidence supports the hypothesis that the difference in stabilities between neutral cage fullerene isomers and their dianion counterparts is determined by the distance between pentagons on the surface of the isomer's fullerene cage. Plots of the HOMO-1, HOMO and LUMO for  $C_{94}^{2-}(I34)$ , the  $C_{94}$  isomer found in  $Ca@C_{94}$  and  $Tm@C_{94}$ , show that the propensity is for added electrons to collect on pentagons not involved in pyracyclene bonding motifs. This is caused by electrostatic repulsion between pentagons as the electron density collects more on pentagon atoms than on non-pentagon atoms.

A more detailed look at the electron properties of a smaller isomeric system of fullerenes ( $C_{80}$ , which has seven IPR isomers) will be taken in the next chapter in order to understand what role these bonding configurations take in determining the stabilities of fullerenes and their anions.

## CHAPTER 3: C<sub>80</sub>: ENERGIES, CHARGES, AND PYRACYCLENE

### BONDS

#### CONTRIBUTIONS:

This chapter represents work that has not yet been published focusing on the relative stabilities of C<sub>80</sub> IPR isomeric set at charges between 0 and -6. Contributions to this chapter are as follows: Tim Fuhrer (author of this dissertation) performed all computational work and all writing in the manuscript.

#### INTRODUCTION:

The previous chapter showed a relationship between the number of pyracyclene motifs and the number of para-fused-pentagons on a C<sub>94</sub> isomer and its dielectron affinity that is caused by the collection of added negative charge onto the pentagon atoms of the cage, which electrostatically repel one another when the pentagons are found in very close proximity to one another, as in the pyracyclene bonding motif. In this chapter we present a much more detailed analysis of the effect of added electrons to the isomers of the much smaller C<sub>80</sub> isomeric set, which has only seven IPR isomers.

C<sub>80</sub> has been one of the most studied isomeric sets of fullerenes, largely because *I<sub>h</sub>(7)C<sub>80</sub>* and *D<sub>5h</sub>(6)C<sub>80</sub>* were the first cages found to contain the trimetallic nitride template (TNT) cluster,<sup>58,93</sup> which have been found to contain electronic and magnetic properties that show great promise for medical applications.<sup>68-76</sup> Recent, yet unpublished experimental results from the Dorn group show that a third IPR isomer of C<sub>80</sub> can be found in endohedral metallofullerenes (EMF), specifically there is experimental evidence for the existence of Y<sub>2</sub>C<sub>2</sub>@C<sub>2v</sub>(5)C<sub>80</sub>, giving evidence that the most stable cage for a C<sub>80</sub> EMF is dependent on the total oxidation state of the endohedral cluster. Slanina has

studied the  $C_{80}$  IPR system extensively using computational methods, but restricted his study to the thermodynamic stability of only the neutral cages.<sup>57,92</sup>

In this chapter we present a complete computational study of the  $C_{80}$  IPR isomeric set including the neutral species as well as the first six anions for each isomer. The first six anions of each isomer were chosen because the oxidation states of experimentally discovered endohedral atoms and clusters found in  $C_{80}$  fullerenes varies between +1 and +6. Each isomer at each charge is studied for charge distribution and structural changes that occur as a result of increased negative charge.

## **COMPUTATIONAL METHODS:**

All seven IPR isomers of  $C_{80}$  were modeled at charges between 0 and -6 via density functional theory with the Gaussian 03 modeling program.<sup>47</sup> First, the geometries of each IPR isomer were optimized seven times, once at each charge between 0 and -6, using the B3LYP density functional and the 6-31G(d) basis set. B3LYP is the most popular of all density functional for modeling systems of this size and is known to be particularly accurate, especially in cases like this where an endohedral metal atom is not being considered.<sup>101</sup> Calibration steps shown in chapter 2 of this work demonstrate that the B3LYP functional produces results comparable to that of other density functional methods. The 6-31G(d) basis set is larger and more accurate than the 3-21G basis set and includes polarization functions which allow some flexibility to the wave function to include higher level orbitals needed to accurately describe bonding. Models with odd number charges were assumed to be in the doublet spin state while those with even number charges were assumed to have the singlet spin state.

Once the geometry of each isomer had been optimized at each desired charge, a vibrational frequency analysis was performed on each model to assure that each geometry was in fact a minimum on its potential energy hypersurface rather than a saddle point. Optimized geometries with imaginary frequencies were reoptimized either using tighter convergence criteria, or from an adjusted starting geometry in order to find an optimized geometry with no imaginary vibrational modes.

The energies computed for each optimized isomer at each charge were used to evaluate which isomer was most stable at each charge and what the optimum charge is for each isomer. For each IPR isomer, we plotted relative electronic energy versus charge. We then examined the relationship between the location of the minimum of each parabola and the number of pyracyclene motifs and para-fused-pentagons on the corresponding isomer. Additionally, we calculated the difference in Mulliken charge for each atom of each isomer as that isomer was changed from neutral to the -6 anion. The length change for each bond of each isomer was also calculated for the same change. These results were tabulated to show which types of atoms and bonds absorbed the largest fraction of the added electrons and how those electrons affected the geometry of the cage.

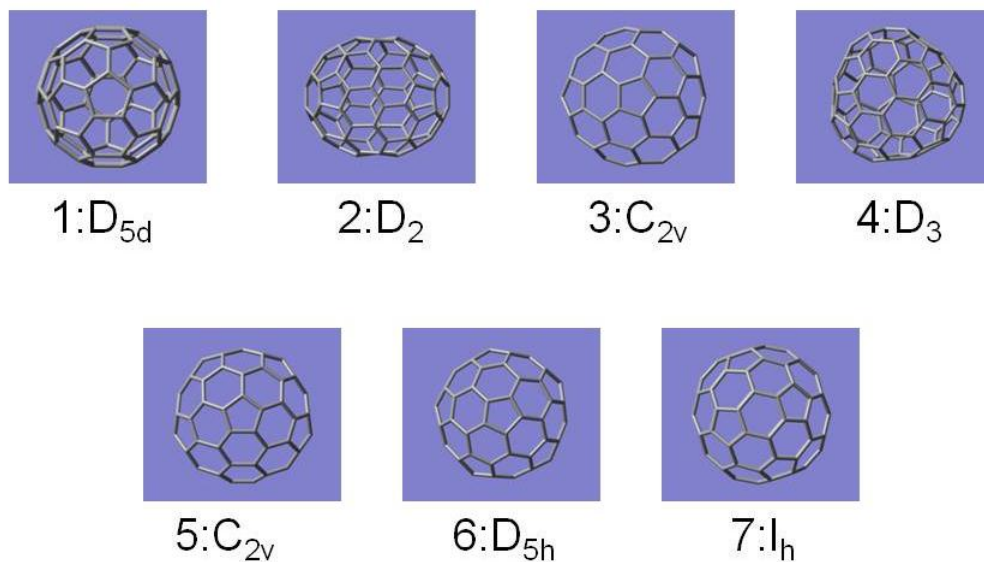


Figure 19: The seven IPR isomers of C<sub>80</sub>.

**RESULTS AND DISCUSSION:**

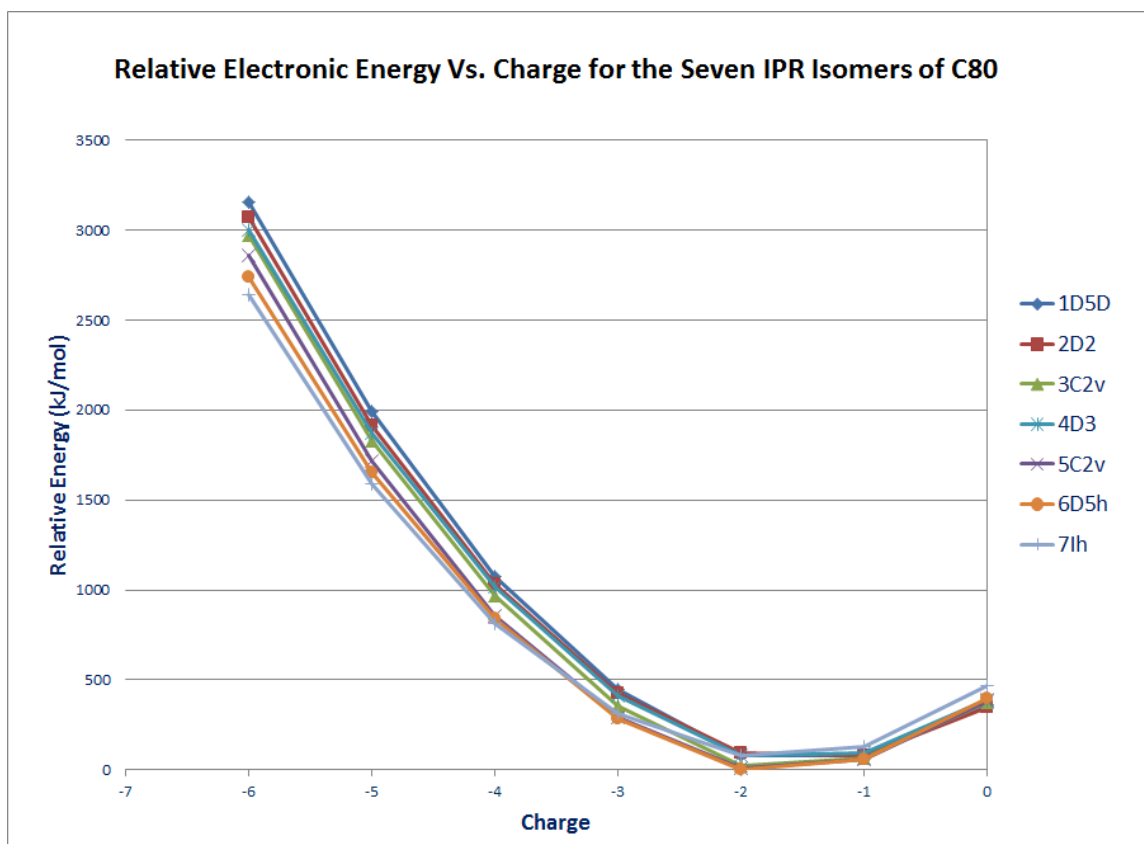
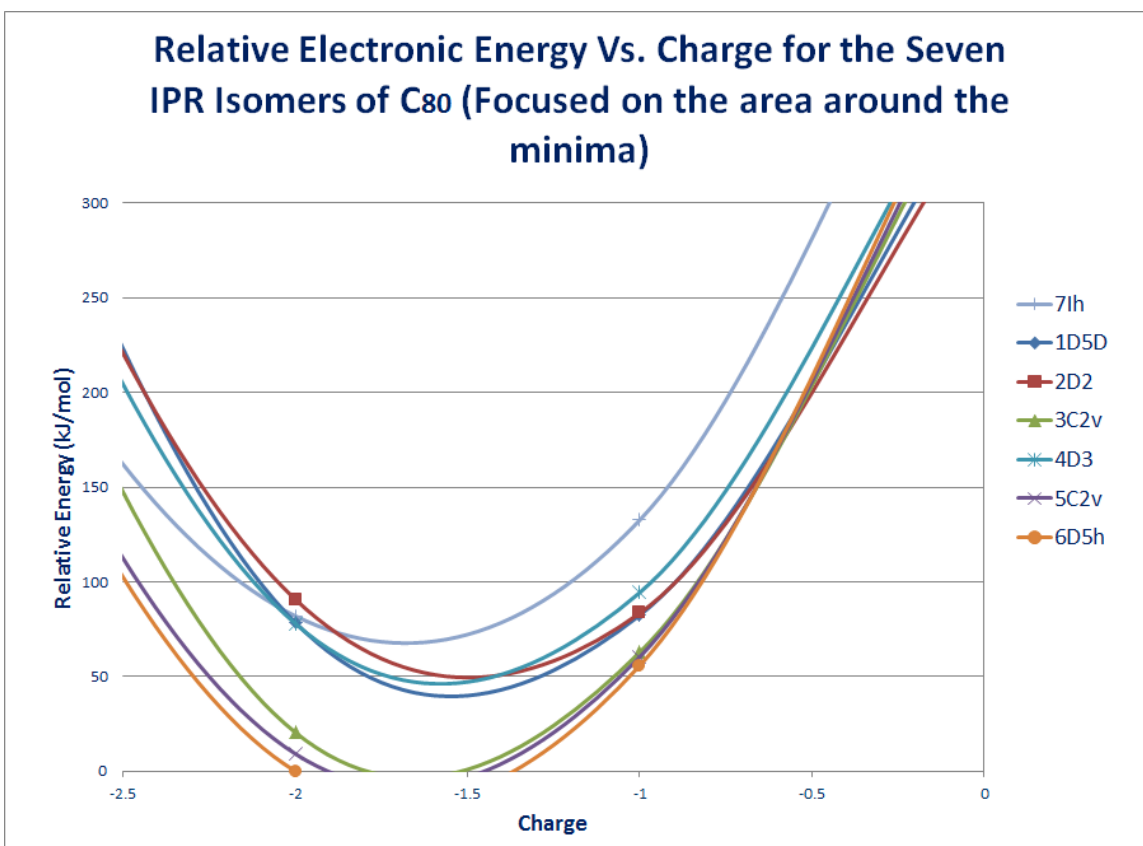
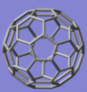
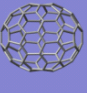
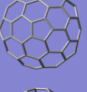
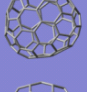
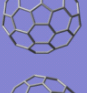
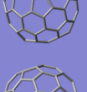
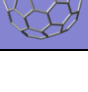


Figure 20: Relative electronic energy versus charge for the seven IPR isomers of C<sub>80</sub>.



**Figure 21: Relative electronic energy versus charge for the seven IPR isomers of C<sub>80</sub> focused on area around the minima.**

A plot of relative electronic energy versus charge yielded a nearly perfect parabola for each IPR isomer of C<sub>80</sub> (See **Figure 20 and 21** above). The minimum of each parabola gives us a relative energy comparison between the isomers as well as an idea as to which isomer is the best equipped to absorb electrons (see **Table 1** below).

Isomer		Parabola Minimum	Pyra	Para
1 D <sub>5D</sub>		(-1.40, 61.7)	20	0
2 D <sub>2</sub>		(-1.41, 59.6)	18	2
3 C <sub>2v</sub>		(-1.51, 26.1)	13	8
4 D <sub>3</sub>		(-1.46, 69.0)	15	6
5 C <sub>2v</sub>		(-1.61, 1.00)	9	9
6 D <sub>5h</sub>		(-1.62, 7.79)	5	20
7 I <sub>h</sub>		(-1.68, 71.1)	0	30

**Table 2: Minima from graph of relative energy (kJ/mole) versus charge for each isomer of C<sub>80</sub> compared to the number of para-fused-pentagons and pyracyclene motifs on each isomers.**

A plot of the count of Pyracyclene bonding motifs versus the charge at the energy minimum of each quadratic above (**Figure 22** below) shows a correlation (albeit nonlinear) suggesting that the presence of pyracyclene bonding motifs on the cage destabilizes the addition of negative charge to the cage.



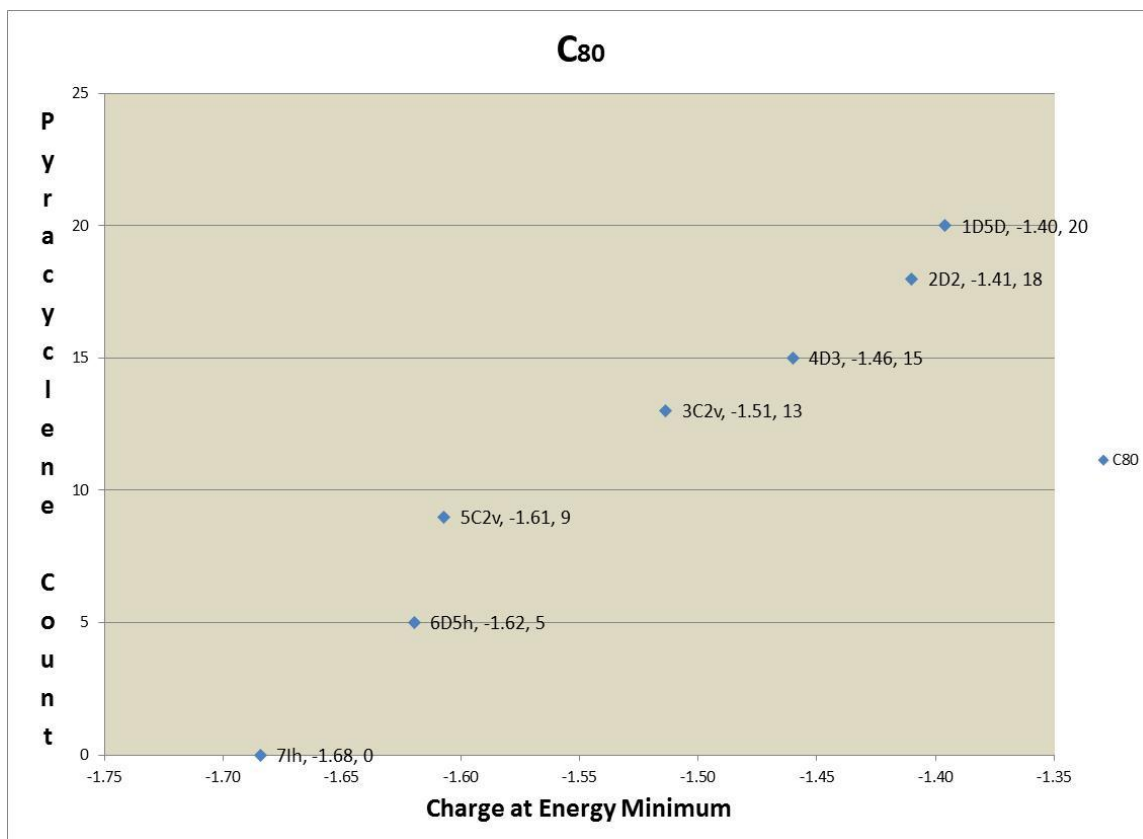


**Figure 22: Plot of Pyracylene count for each IPR isomer of  $C_{80}$  versus the charge of the cage at its energy minimum.**

A plot of the counts of Para-Fused-Pentagon bonding motifs versus the charge at the energy minimum of each quadratic above (**Figure 23** below) shows a correlation (also nonlinear) suggesting that the presence of pyracylene bonding motifs on the cage may stabilize the addition of negative charge to the cage.

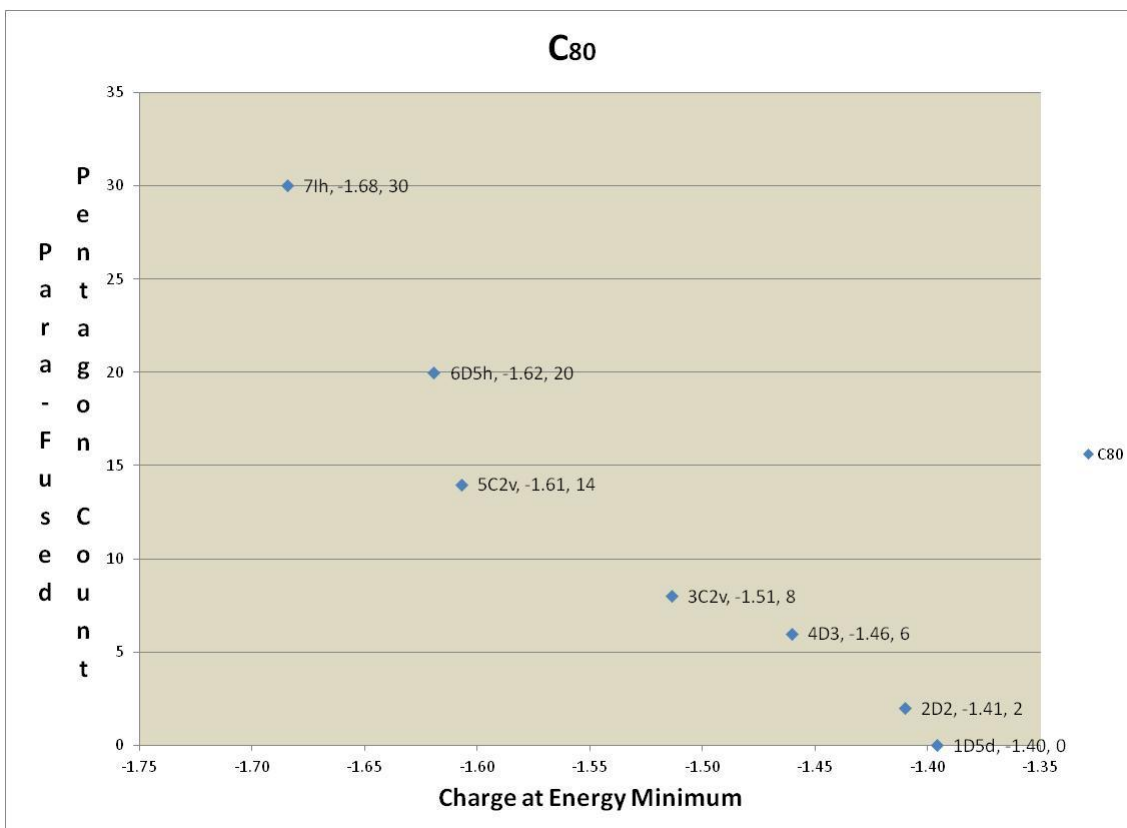


**Figure 23: Plot of Para-Fused-Pentagon count for each IPR isomer of  $C_{80}$  versus the charge of the cage at its energy minimum**

An analysis of the effect that adding six electrons to the cage of each isomer has on the charge of each atom and the length of each bond shows that the added charge is only partially delocalized across the cage and accumulates more on some atoms than others (see **Appendix 2** for a detailed list of the average change in charge for each atom type on each isomer). For example, adding 6 electrons to isomer number 1 ( $D_{5d}$ ) caused the average charge of each pyracyclene atom (an atom on a pentagon that is bonded directly to another pentagon) to become  $0.0879 e$  more negative, while the average pentagon atom that was not part of a pyracyclene bond became  $0.0647 e$  more negative and non-pentagon atoms (hexagon only) became  $0.0595 e$  more negative on average. This means that on average, pyracyclene carbon atoms are absorbing 36% more added

negative charge than non-pyracyclene pentagon carbon atoms, and 48% more than atoms that are not on pentagons.

The bonds that run from pentagon to pentagon, the so-called pyracyclene bonds, are lengthened by the adding of electrons more so than any other bonding motifs. For example, in the  $D_{5d}$  isomer, the additional six electrons caused the average pyracyclene bond to lengthen by 0.0333 angstroms, approximately 30 times as much as the average lengthening for bonds surrounded on all sides by hexagons. This makes sense considering that the pentagon atoms have become more negative by adding the electron density that the bonds that join pentagons together would become weaker and of higher energy and the hexagon-only atoms have absorbed the least negative charge.

One interesting feature is that the bonds that make up the pentagon edges also either shorten, or lengthen very slightly, even though the atoms of the pentagon are the ones absorbing most of the added electron density. For example, on the  $D_{5d}$  isomer, the average pentagon edge bond length *shortened* by 0.0015 angstroms. It is likely then that the electron density that accumulates on the pentagon atoms is in bonding orbitals in toward the other pentagon atoms, but in antibonding orbitals toward the off pentagon atoms. A detailed analysis of how the length of each bond type on each isomer was affected by the addition of six electrons to that isomer is included in **Appendix 2**.

Analysis of the stability of each anion of each cage shows that the most stable isomer is dependent on the amount of negative charge transferred to the cage. The  $I_h(7)$  cage is the most stable for cage charges of -4, -5 and -6, but the difference in stability between the  $I_h(7)$  cage and the second most stable isomer at those charges, the  $D_{5h}(6)$  becomes smaller as the charge becomes less negative. The  $D_{5h}(6)$  cage is the most stable

at cage charges of -1, -2, and -3, and the difference between it and the second most stable isomer at those charges, the  $C_{2v}(5)$  becomes smaller as the charge becomes less negative.

The lowest energy species out of the 49 modeled for this project (all seven IPR isomers of  $C_{80}$  at seven different charges from 0 to -6) is the  $D_{5h}$  isomer (number 6) with a -2 charge. A closer look at that particular species will give us more insight into cause for the stability differences between different isomers at different charges.

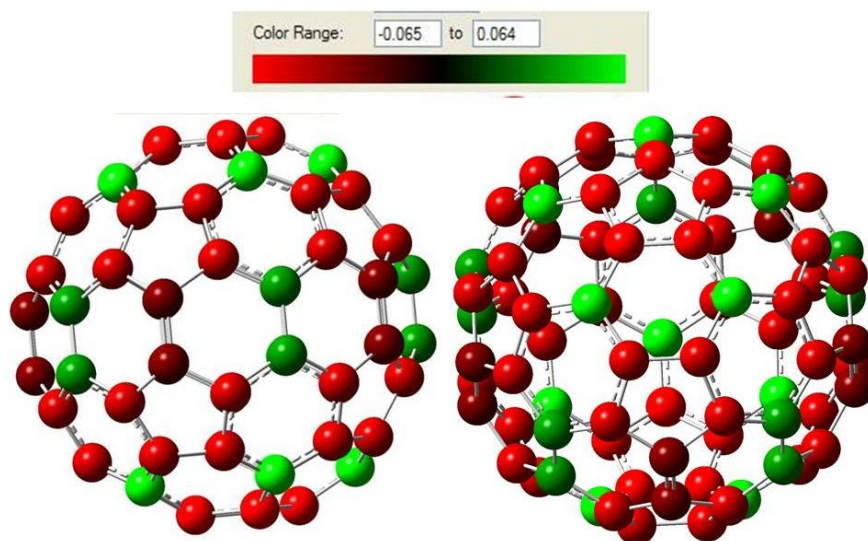


**Figure 24:** Model of the  $C_{80}^{2-}(6)D_{5h}$  anion showing the relative Mulliken charges for each atom from two different points of view.

**Figure 24** above shows pictorially that the added negative charge does collect on the pentagon carbon atoms (red), leaving the carbon atoms that are hexagon only with partially positive charges, even on a fullerene dianion. We see both of the proposed hypotheses at work here. Bonds that hold two pentagons together (the so-called pyracyclene motif) are destabilized because the two pentagons repel one another as a result of their increased negative charge. The para-fused-pentagon motif is stabilized by the two positively charged hexagon atoms that separate the pentagons that are fused para to one another on that hexagon.

The answer to the question of why charge collects on pentagon carbon atoms rather than hexagon carbon atoms can be seen in **Figure 25** below in the plot of the HOMO for  $C_{80}^{2-}(6)D_{5h}$ . Each pentagon can become a region of aromaticity when an additional pi electron is added to it.

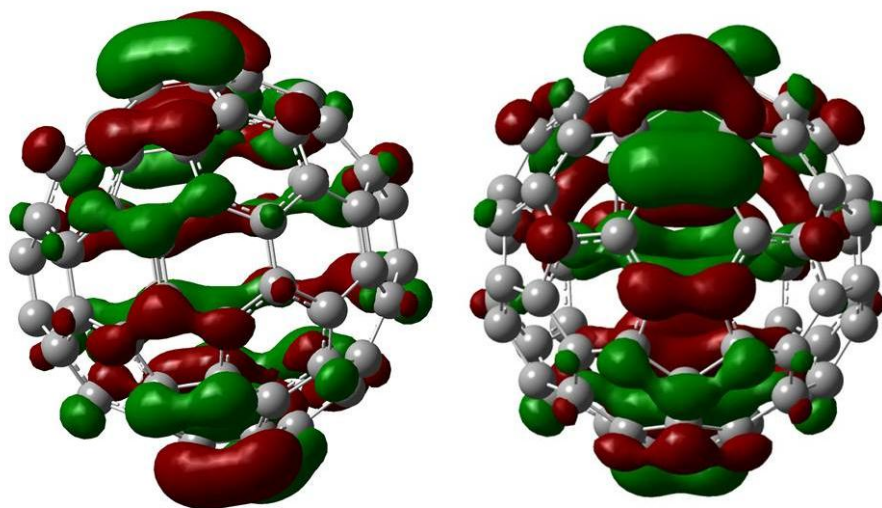


**Figure 25:** Plot of the HOMO of  $C_{80}^{2-}(6)D_{5h}$  from two different points of view.

#### **CONCLUSION:**

The results of computations presented herein support the hypothesis that the ability of empty fullerene cages to accept electrons is dependent on the structure of the cage. In particular, the presence of pyracyclene bonding motifs on the cage is a strong indicator of an inability to accept electrons, while the presence of the para-fused-pentagon motif is a strong indicator of an ability to accept electrons. The cause for both of these phenomena is the accumulation of electron density on the pentagon atoms, which absorb more of the added negative charge than do the non-pentagon carbon atoms. Electrostatic repulsion between the more negatively charged pentagons atoms causes cages with pentagons only separated by one bond to become unstable as electron density

is added, while those with the more positive hexagon atoms separating the pentagons become more stable as electrons are added.

That being said, the pentagon edge bonds do not get much longer with the added electron density and in some cases shorten. This could be explained by assuming that the electrons localized in those bonding areas are in bonding orbitals rather than antibonding orbitals. Adding an additional electron to bonding orbitals on a pentagon of a fullerene cage gives a total of six pi electrons on the pentagon, causing a localized region of aromaticity. This gives a possible explanation for the stability of fused pentagon isomers for EMFs.

## CHAPTER 4: $Y_2C_2@C_{2n}$ : AN ENDOHEDRAL METAL CARBIDE FULLERENE

### CONTRIBUTIONS:

This chapter represents contributions from two sources: (i) work published the Dorn group and our collaborators at the University of Virginia detailing the relationship between computational models of  $D_3$ - $Y_2C_2@C_{92}$  synthesized and characterized by our group<sup>9</sup>, and (ii) work that has just been accepted for publication in the Journal of the American Chemical Society describing the nanoscale compression of the  $Y_2C_2^{4+}$  endohedral cluster as size of the fullerene containing it becomes smaller.<sup>10</sup> Contributions from the authors of these works are as follows: all computational molecular modeling was performed by Tim Fuhrer (author of this dissertation). Syntheses and separations of yttrium carbide fullerenes were performed by Jianyuan Zhang, Wujun Fu, Jiechao Ge, James Duchamp and Hunter Champion of the Dorn group.  $^{13}C$  NMR data were obtained by Hugo Azurmendi, Dan Bearden and Jerry Dallas. Mass spectrometry experiments were performed by Kim Harich, Raman experiments were performed by Brian Burke and G. Chan. Writing of manuscript (i) was primarily the work of Brian Burke with the supervision and editing of Kenneth Williams. Writing of manuscript (ii) was accomplished primarily by Jianyuan Zhang with the supervision and editing of Harry Dorn.

### INTRODUCTION:

The synthesis and characterization of a yttrium carbide fullerene is of particular interest because of the potential use of yttrium carbide materials as a new class of superconductors.<sup>119</sup> The first metal carbide EMF to be reported was  $Sc_2C_2@C_{82}$  by

Shinohara and coworkers.<sup>120</sup> Soon after, a number of other metal carbide EMFs were reported,<sup>121-123</sup> including the first yttrium carbide EMF,  $Y_2C_2@C_{82}$ , which was found with three different cage geometries ( $C_s$ ,  $C_{2v}$  and  $C_{3v}$ ).<sup>124</sup> Wujun Fu from our group isolated the  $Y_2C_2@C_{92}$  molecule from the plasma-arc soot of a yttrium packed rod without the presence of  $N_2$  gas during the reaction.<sup>125</sup> The existence of a  $D_3$ - $Y_2C_2@C_{92}$  (IPR isomer number 85 according to Fowler's book)<sup>2</sup> structure rather than a  $Y_2@C_{94}$  was confirmed by  $^{13}C$ -NMR spectroscopy (see **Figure 26** below). Based on the above  $^{13}C$ -NMR evidence, particularly the perfect triplet seen for the carbide at 227.26 ppm (splitting of 22.4 Hz caused by the yttrium atoms), we expected the geometry of the  $Y_2C_2$  cluster to be planar with the Yttrium atoms aligned along the  $D_3$  axis of the cage and the carbide aligned perpendicular to the axis. This is consistent with a similar structure for  $Gd_2C_2@C_{3v}(8)C_{92}$  published by Balch's group and confirmed by X-ray crystal data.<sup>8</sup>



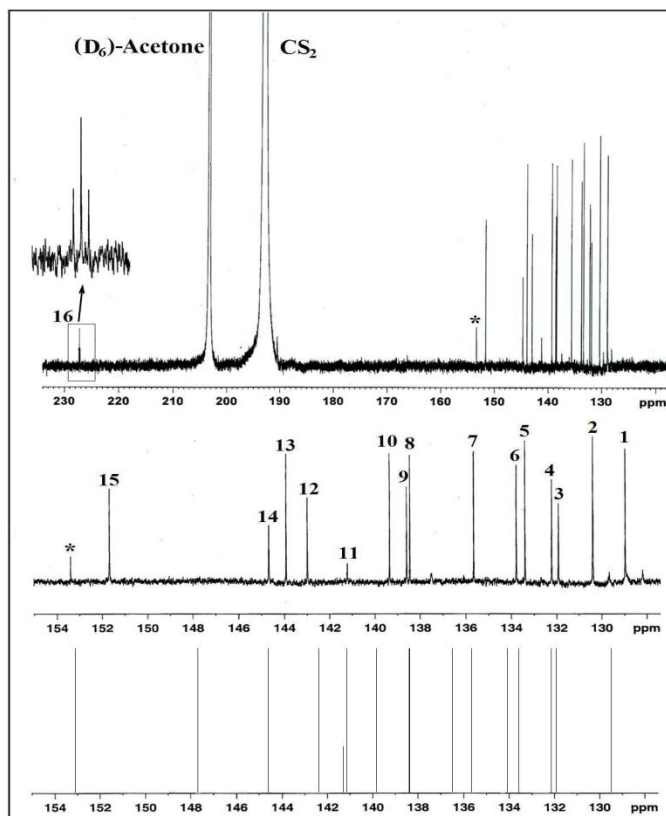


**Figure 26:** 800MHz  $^{13}\text{C}$  NMR spectrum of  $\text{Y}_2\text{C}_2@D_3(85)\text{-C}_{92}$  in  $\text{CS}_2$  with 10 mg  $\text{Cr}(\text{acac})_3$  relaxant, acetone- $d_6$  lock after 32768 scan at 25 °C. (a) The whole range of  $^{13}\text{C}$  NMR spectrum of  $\text{Y}_2\text{C}_2@D_3(85)\text{-C}_{92}$  (b) Expand range (from 128 to 154 ppm) of  $^{13}\text{C}$  NMR spectrum of  $\text{Y}_2\text{C}_2@D_3(85)\text{-C}_{92}$ . The signal marked with \* is assigned to impurities because it was not visible in the 600 MHz  $^{13}\text{C}$  NMR and its unreasonable chemical shift. (c) Calculated  $^{13}\text{C}$  NMR spectrum of  $\text{Y}_2\text{C}_2@D_3(85)\text{-C}_{92}$ . (figure from reference <sup>125</sup>)

Jianyuan Zhang, also of our group, has isolated and characterized  $\text{Y}_2\text{C}_2@C_{3v}(8)\text{C}_{82}$  from same plasma-arc soot as the  $\text{Y}_2\text{C}_2@D_3(85)\text{C}_{92}$  mentioned earlier. A similar triplet was found for the carbide group in the  $^{13}\text{C}$ -NMR, this time at 257 ppm with a  $^1J_{\text{Y-C}}$  coupling of 17.2 Hz (see **Figure 27b** below).

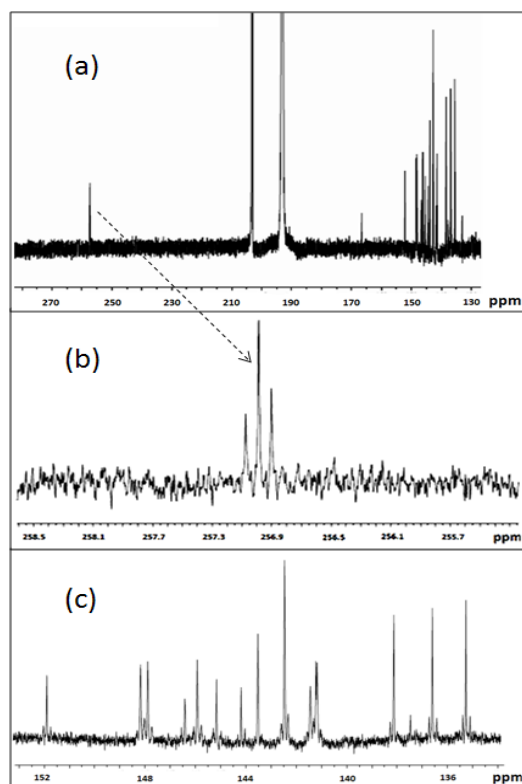
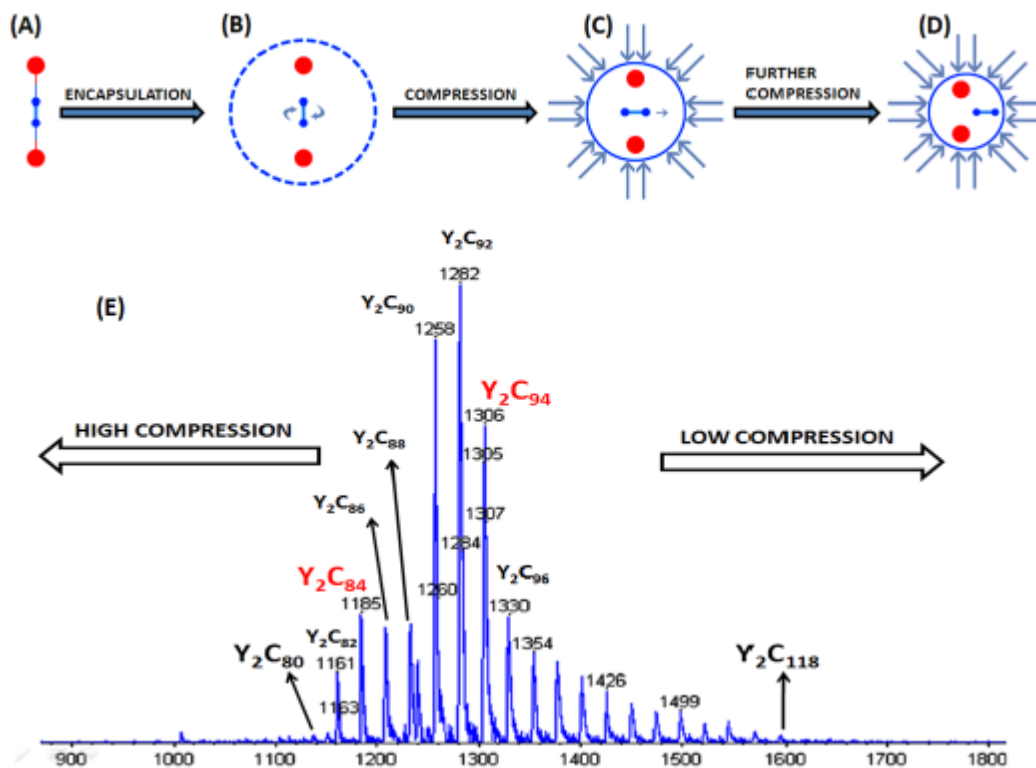


Figure 27:  $^{13}\text{C}$ -NMR for  $\text{Y}_2\text{C}_2@C_{2v}(8)\text{C}_{82}$ .

Experimental and computational results for these two molecules supports the idea of a cluster that is progressively more compressed as the cage size decreases. This nanoscale fullerene compression (**NFC**) of metal clusters by decreasing fullerene cage size can be directly compared to the effects of macroscopic pressure compression (**MPC**) of the same metal carbide lattice, yttrium carbides.  $\text{Y}_2\text{C}_3$  for example, has been reported as a superconductor whose superconducting transition temperature ( $T_c$ ) is strongly dependent on the external pressure.<sup>119</sup>

To test this hypothesis, in addition to the  $\text{Y}_2\text{C}_2@C_{82}$  and  $\text{Y}_2\text{C}_2@C_{92}$ , a hypothetical  $\text{Y}_2\text{C}_2@C_{100}$  and the linear  $\text{Y}_2\text{C}_2^{4+}$  ion were also modeled for cluster size and shape as well as NMR properties. These models were then compared to experimental data for all systems for which it is available. MALDI-TOF-MS analysis of the plasma

arc soot shows that there may be not only these, but a number of other yttrium carbide fullerenes in the soot (see **Figure 28** below).



**Figure 28:** Nanoscale fullerene compression of yttrium carbide endohedral fullerenes. (a)  $Y_2C_2^{4+}$  cluster without a cage. (b) Linear  $Y_2C_2^{4+}$  cluster inside a large fullerene cage. (c)  $Y_2C_2^{4+}$  cluster with carbide bond vector orthogonal to the yttrium-yttrium vector in a compressed fullerene cage. (d)  $Y_2C_2^{4+}$  cluster with carbide bond vector orthogonal to and deviated from yttrium-yttrium vector. (e) Mass-spectrometry showing a family of endohedral metallofullerenes with formula  $Y_2C_{2n}$ .

The experimental data included herein, attained by several members of the Dorn group, include a detailed study of the  $^{13}C$  NMR of  $Y_2C_2@D_3(85)C_{92}$ ,  $^{13}C$  enriched  $Y_2C_2@C_{3v}(8)C_{82}$ , as well as an isomer of  $Y_2C_2@C_{84}$ . For the first time, the Dorn group has observed the important scalar  $^1J_{Y-C}$  coupling for each of these samples. These coupling values will also be compared to computed values.

## COMPUTATIONAL METHODS:

In order to augment the experimental observations and assist in explaining some of the physical properties of these yttrium carbide fullerenes, density functional theory (DFT) geometry optimizations using the B3LYP functional<sup>102,103,126</sup> as described in the Gaussian 09<sup>127</sup> program package were performed for  $Y_2C_2@C_{3v}(8)C_{82}$ ,  $Y_2C_2@D_3(85)C_{92}$ , and  $Y_2C_2@D_5(450)C_{100}$  molecules, and the  $Y_2C_2^{4+}$  cation (to approximate the  $Y_2C_2$  cluster in an infinitely large cage). In each of these computations, the 6-31G basis set was used for carbon and the DZVP basis set was used for yttrium atoms<sup>128</sup>. Geometry optimizations were performed on each species with the starting geometries based on computational predictions of the corresponding  $Sc_2C_2@C_{3v}(8)C_{82}$  computations by Poblet<sup>129</sup> (see **Figure 29**), and the crystal structure for  $Gd_2C_2@D_3(85)C_{92}$  published by Yang et al.<sup>8</sup> For the  $Y_2C_2@D_5(450)C_{100}$  molecule, the  $D_5$  isomer number<sup>2</sup> 450 (see **Figure 30** in the next section) was chosen based on previous theoretical work by Nagase,<sup>130</sup> and a linear cluster geometry was chosen.

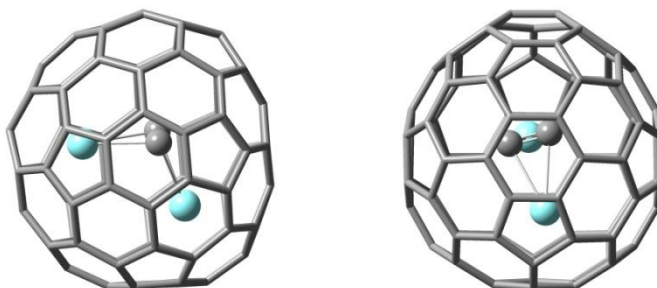


**Figure 29:** Front and side view of starting geometry for  $Y_2C_2@C_{3v}(8)C_{82}$ .

Optimized geometries were shown to be potential energy surface minima rather than saddle points by the absence of imaginary frequencies from the computed harmonic frequencies. The transition state geometry for  $Y_2C_2@D_3(85)C_{92}$  (See **Figure 31** in the

next section) showed one imaginary frequency associated with the vibration of the internal carbide group between two optimized structures. NMR spectra computations were carried out on the optimized geometry using the OPBE density functional<sup>131</sup> and the 6-311G basis set for carbon atoms and DZVP basis set for yttrium atoms.

## RESULTS:

For the hypothetical  $Y_2C_2^{4+}$  cluster, modeling confirmed the proposed linear structure with Y-C bond length of 2.28 Å and C-C bond length of 1.27 Å.  $^{13}C$ -NMR modeling showed a chemical shift for the carbide group of 150 ppm with a  $^1J_{Y-C}$  coupling of 55.5 Hz. This is in good agreement with the experimental observations of the Y-C-C interaction in  $(Cp)_2Y-C\equiv CMe$  by Denhaan *et. al.* which showed a carbide chemical shift of 142 ppm with a  $^1J_{Y-C}$  coupling of 73.9 Hz.<sup>132</sup>

The hypothetical  $Y_2C_2@C_{100}$  proved not to be quite large enough to maintain the expected linear cluster geometry. Each Y-C-C bond angle bent to 157.6 degrees with a cluster dihedral angle of 15.6 degrees (see **Figure 30** below). It is likely that the non-zero dihedral angle is caused by attraction of the yttrium atoms for the partial negative charge found on the polar pentagons, which are skewed from one another by 22 degrees. The predicted  $^{13}C$ -NMR chemical shift for the carbide group was 156 ppm and the predicted  $^1J_{Y-C}$  coupling was 63.0Hz, showing that the bonding in this cluster is similar to that of the  $Y_2C_2^{4+}$  cluster not inside a fullerene.



**Figure 30: Computational model of  $Y_2C_2@C_{100}$ . Cluster is slightly compressed with Y-C-C bond angles of 157.6 degrees and a dihedral angle of 15.6 degrees.**

For the  $Y_2C_2@D_3(85)C_{92}$ , the NMR predicted planar cluster geometry was not found by geometry optimization, but rather a skewed nonplanar cluster geometry (see **Figure 31(a)** below). The expected nearly planar geometry was found when the transition state was modeled (see **Figure 31(b)** below).



**Figure 31: Two views of the modeled cluster geometry for  $Y_2C_2@C_{92}$ . The left view (a) is the optimized structure while the right view (b) is the transition state structure between two equivalent optimized structures.**

The transition state modeling was accomplished using the same method and basis set as the optimized structure. The presence of one imaginary vibrational frequency confirmed the geometry as a transition state. The difference in total energy between the optimized structure and the transition state structure is approximately 12 kJ/mol.

The optimized structure has Y-C bond lengths of 2.29 Å and 2.82 Å with a C-C bond length of 1.27 Å. The predicted  $^{13}\text{C}$ -NMR shift for the carbide group was 229 ppm, excellent agreement with the experimental determined 227 ppm shift. The predicted  $^1\text{J}_{\text{Y-C}}$  coupling to the nearest carbon to each yttrium was 40.6 Hz. It was 4.4 Hz between a yttrium and the further away carbide carbon. This averages out to 22.5 Hz, a near perfect match to the 22.4 Hz experimental observation, but this does not explain the perfection of the observed triplet.

The transition state structure has Y-C bond lengths of 2.48 Å with a C-C bond length of 1.28 Å. The predicted  $^{13}\text{C}$ -NMR shift for the carbide group in this case was 288 ppm with a predicted  $^1\text{J}_{\text{Y-C}}$  coupling was 21.6 Hz. One can rationalize the experimental results with the computed models by treating the cluster as oscillating very quickly between equivalent optimized states while passing through the predicted transition state geometry. Since the most time would be spent in the optimized states, the observed chemical shift and average  $^1\text{J}_{\text{Y-C}}$  coupling closely matches that predicted for the optimized structure, but since the oscillation happens so quickly, the NMR sees the states as averaged and produces the observed triplet rather than a more complicated splitting pattern.

In order to confirm that this transition state is the transition state between two equivalent optimized structures, we attempted an Intrinsic Reaction Coordinate (IRC) calculation using the transition state geometry as the initial structure, the B3LYP density function, the 6-31G basis set for the carbon atoms and the DZVP basis set for the yttrium atoms. Though this calculation proved to be too large for the computational resources available, the partial results confirmed that the transition state structure we found does

move toward the optimized structure described earlier. In addition, the partial results of the IRC calculation showed that as the cluster changes from the planar transition state geometry to the skewed optimized geometry, it rotates within the cage. The yttrium atoms can be viewed as forming an axis of rotation for the carbide carbon atoms, and the carbide carbon atoms acting as a horse on an amusement park **carousel**, moving up and down in relation to the axis as they rotate about it.

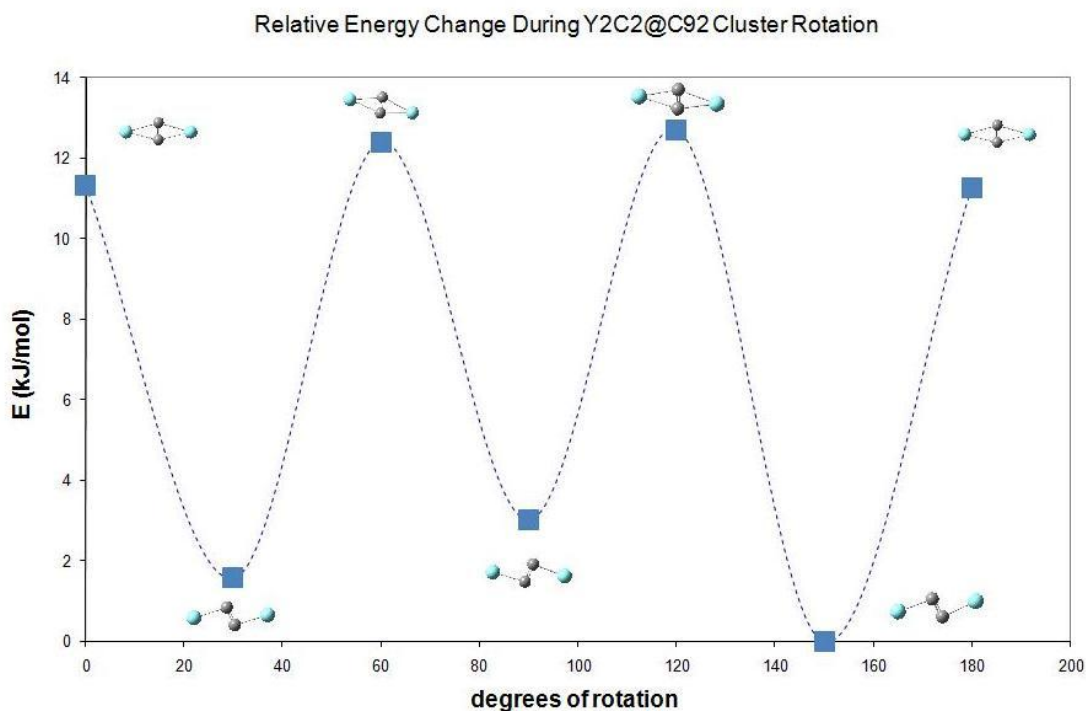


**Figure 32: Energetics of Rotation of Y<sub>2</sub>C<sub>2</sub> Cluster within the C<sub>92</sub> Cage.**

To test this hypothesis, we optimized structures and transition states with the cluster rotated various numbers of degrees around the yttrium axis (see **Appendix 4** for models of geometries). The results are shown in **Figure 32** above with representations of each cluster with a horizontal axis of rotation. The three transition states found each consist of a nearly planar cluster with the carbide group lined up directly with one of the



three pyracyclene bonding motifs found around the equator of the cage (see **Figure 33** below).

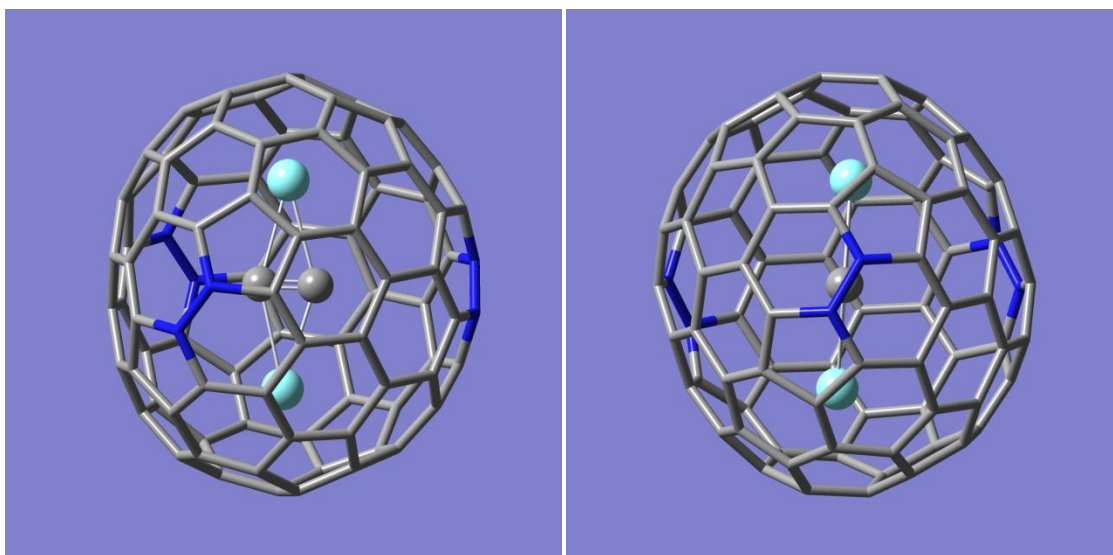


**Figure 33:**  $Y_2C_2$  from two different viewpoints with pyracyclene atoms shown in dark blue.

Upon more detailed examination of the high resolution NMR spectrum obtained by Hollings Marine Laboratory, we noticed that many of the carbon atoms around the equator of the cage (if we again consider the yttrium atoms as defining the rotational axis) have a slight broadening of their signal, while several others did not. The equatorial carbon atoms whose signal was not broadened were the pyracyclene motif atoms that lined up with the transition state geometry (shown in blue and indicated by arrows in **Figure 34** below) giving experimental evidence that these are the equatorial atoms that the carbide atoms spend the least time near.

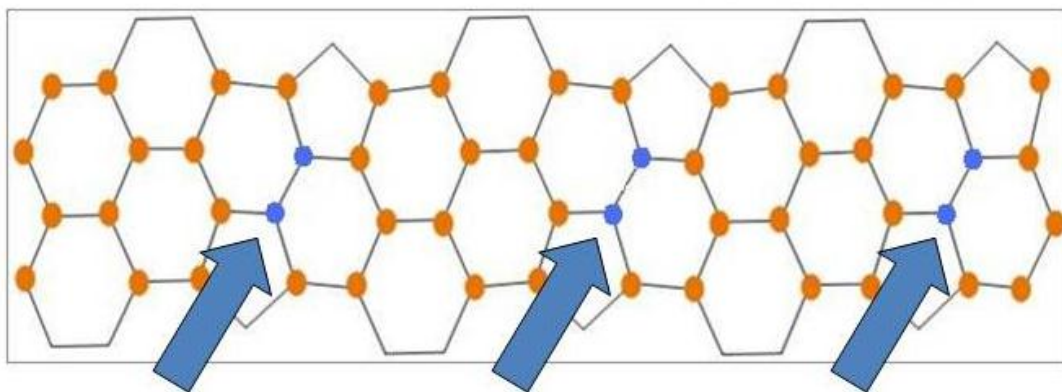
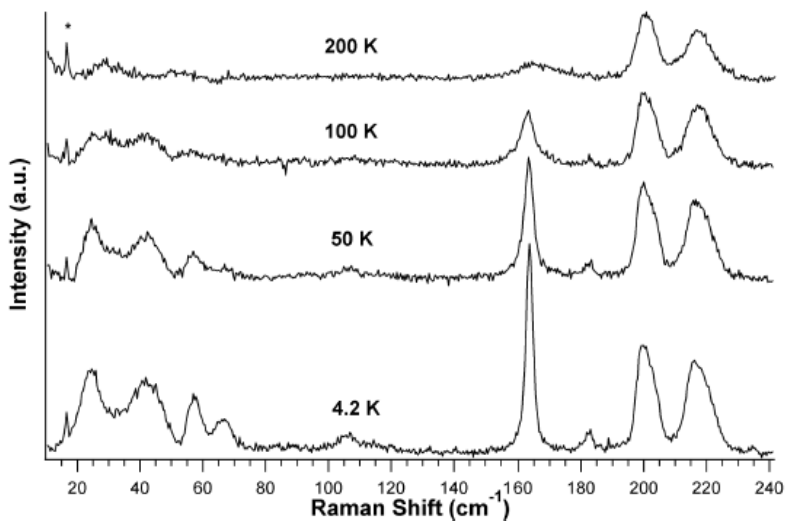


**Figure 34: Equatorial carbon atoms on the  $C_{92}$  cage. Atoms with significant signal broadening in the NMR show in orange, those without significant signal broadening, the pyracyclene bonding motifs, are shown in blue.**

Based on the density surface map shown in **Figure 3** in chapter 1, we can see an area of charge density behind each pyracyclene bond that is likely the reason for the carbide group's avoidance of the pyracyclene atoms.

Brian Burke and Keith Williams from the Physics Department at University of Virginia studied  $Y_2C_2@C_{92}$  in collaboration with our group using low temperature Raman spectroscopy.<sup>9</sup> The results shown in **Figure 35** below show that low frequency Raman signals emerge at very low temperatures. These peaks match the predicted frequencies for several modes of rotation of the carbide if it is treated as a free rigid rotor (see table included in **Figure 35**).



Experiment ( $\text{cm}^{-1}$ )	Free $\text{C}_2$ rotor ( $\text{cm}^{-1}$ )	Perturbed $\text{C}_2$ rotor ( $\text{cm}^{-1}$ )
24.2	24.2 (2 $\rightarrow$ 4)	0.0
42.2	38.1 (4 $\rightarrow$ 6)	0.0
57.0	51.9 (6 $\rightarrow$ 8)	0.0
66.9	65.7 (8 $\rightarrow$ 10)	0.0
106.1	107.3 (14 $\rightarrow$ 16)	0.0

**Figure 35: Raman spectroscopy of  $\text{Y}_2\text{C}_2@C_{92}$  at several temperatures with matching  $\text{C}_2$  free rigid rotor frequencies. (figure from reference <sup>9</sup>)**

As for the  $\text{Y}_2\text{C}_2@C_{3v}(8)C_{82}$ , the computationally optimized geometry matches very closely with the experimental observations of Nagase and the computational predictions of Poblet for the  $\text{Sc}_2\text{C}_2@C_{3v}(8)C_{82}$ .<sup>129,133</sup> The geometry of the cluster is even more compressed than in the  $\text{Y}_2\text{C}_2@C_{92}$  case (see **Figure 36** below). The average predicted Y-C bond length was 2.43 Å. The predicted  $^{13}\text{C}$ -NMR chemical shift for the carbide was 288 ppm, compared to the experimentally observed 257 ppm. The predicted  $^1J_{\text{Y-C}}$  coupling for the carbide in  $\text{Y}_2\text{C}_2@C_{82}$  was 18.3 Hz compared to the experimentally observed 17.2 Hz.

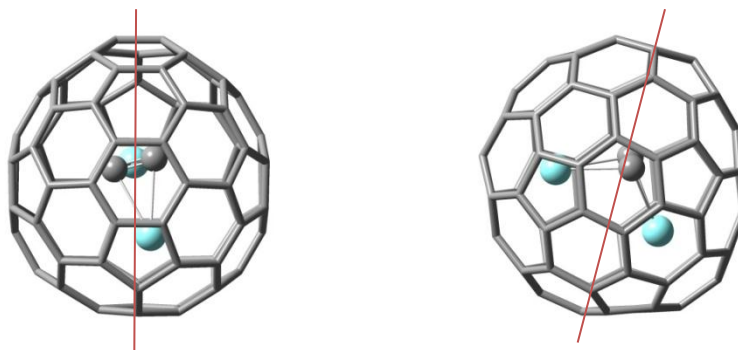







**Figure 36: Optimized structure of  $Y_2C_2@C_{82}$ . Symmetry axis for each view is shown in red.**

## DISCUSSION:

The experimental and computational results are summarized in **Table 2** below. The  $(Y_2C_2)^{4+}$  cluster clearly prefers a linear geometry in the absence of a fullerene cage. However, even in relatively large cages like  $C_{100}$ , the cluster geometry is slightly distorted from a linear configuration. As the cage size gets smaller the  $(Y_2C_2)^{4+}$  cluster geometry becomes more distorted into an idealized butterfly shape ( $C_{92}$ ) and a compressed butterfly shape ( $C_{82}$ ).

It is also clear that the  $^{13}C$  NMR shift for the carbide group in the cluster and its  $^1J_{Y-C}$  coupling parameters provide a very sensitive probe of the degree of NFC compression of the  $(Y_2C_2)^{4+}$  cluster, as illustrated by the right two columns of **Table 2**. The carbide signal exhibits a significant deshielding, which increases with increased NFC compression from about 150 ppm for the nearly linear clusters ( $C_{100}$  or no cage) to over 250 ppm for compressed clusters ( $C_{82}$  cage). At the same time, the scalar  $^1J_{Y-C}$  coupling decreases upon NFC compression from over 50 Hz for the nearly linear clusters to about 17 Hz in the smaller caged clusters.

Molecule	Optimized cluster structure	Average atomic distance in the cluster Y-C/Y-Y/C-C (Å)	C <sub>2</sub> <sup>13</sup> C NMR chemical shift (ppm)	<sup>1</sup> J <sub>Y-C</sub> (Hz)
(Y <sub>2</sub> C <sub>2</sub> ) <sup>4+</sup>		2.92/5.83/1.27	147* (150)	70.9* (55.5)
Y <sub>2</sub> C <sub>2</sub> @D <sub>3h</sub> -C <sub>100</sub>		2.89/5.51/1.26	(156)	(57.1)
Y <sub>2</sub> C <sub>2</sub> @D <sub>3h</sub> -C <sub>92</sub> (opt)		2.53/4.92/1.27	227.3 (229)	22.4 (22.5**)
Y <sub>2</sub> C <sub>2</sub> @D <sub>3h</sub> -C <sub>92</sub> (TS)		2.48/4.81/1.27	(288)	(21.6)
Y <sub>2</sub> C <sub>2</sub> @C <sub>84</sub>	--	--	247.8	17.8
Y <sub>2</sub> C <sub>2</sub> @C <sub>3v</sub> -C <sub>82</sub>		2.43/3.74/1.27	257.0 (288)	17.2 (18.3)
Y <sub>2</sub> C <sub>2</sub> @C <sub>5</sub> -C <sub>82</sub>	--	--	256.2	17.0

**Table 3: Key results from NMR experiments and DFT Calculations. Numbers in parentheses are computational results.**

\*These values represent the experimental results of (Cp)<sub>2</sub>YC≡CPh·OEt<sub>2</sub>.

\*\*This number represents the average value of the scalar coupling constants between Y atom 1 and carbide atom 1 (40.6Hz), and Y atom 1 and carbide atom 2 (4.4 Hz).

Also shown in **Table 3**, the atomic distances within the (Y<sub>2</sub>C<sub>2</sub>)<sup>4+</sup> cluster computed via DFT suggest that the cluster atoms are forced closer together with increased compression, as indicated by the decreased Y-Y distance and decreased Y-C distance in each cluster as cage size gets smaller. However, the C-C bond distance in the cluster is virtually unaffected by cage size. It is very interesting to note that this trend is very similar to that seen in the superconducting Y<sub>2</sub>C<sub>3</sub> system under macroscopic pressure compression (MPC) for the Y-Y distances, the Y-C distances, and the C-C distances, as shown in **Figure 37** below.<sup>119</sup>

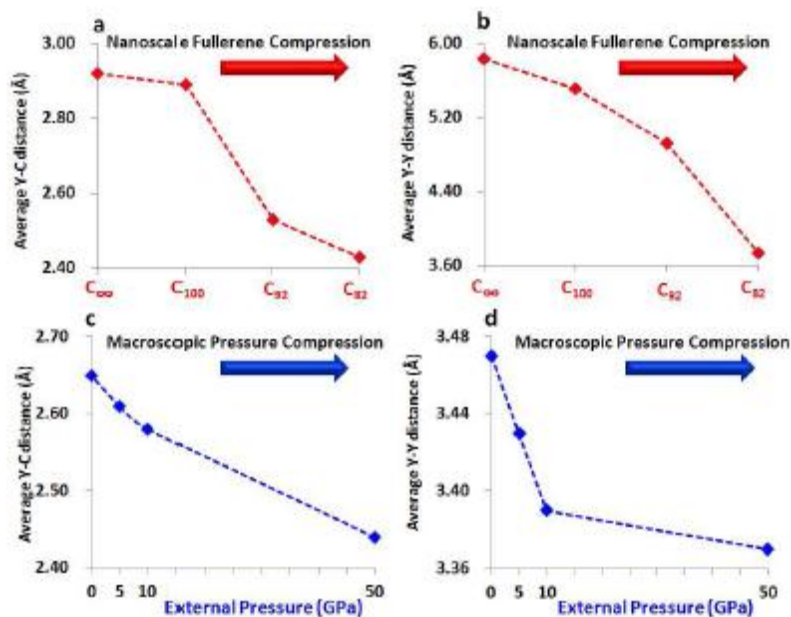


**Figure 37: The change of interatomic distances upon compression. Red lines and points denote the data obtained from NFC (data source Table 2,  $C_{\infty}$  represents the calculated interatomic distances for  $(Y_2C_2)^{4+}$  cluster), and blue lines and points denote the data obtained from MPC (data source Ref. <sup>119</sup>). Y-C distances are average values of corresponding Y-C1, Y-C2 and Y-C3 distances in the lattice. Y-Y distances are average values of corresponding Y-Y1 and Y-Y2 distances in the lattice). (a) Y-C distances in fullerene cages. (b) Y-Y distances in fullerene cages. (c) Y-C distances in superconducting materials. (d) Y-Y distances in superconducting materials.**

## CONCLUSION:

According to Burke and Williams's predictions, if the rotation of the carbide group in  $Y_2C_2@C_{92}$  is hindered, or "perturbed", there should be no signal for the rotation in the Raman spectra. This has led to speculation that the carbide atoms may be tunneling from one energy minimum to the next, without classically traveling through the transition state in between. Quantum mechanical tunneling of this type often plays a role in reactions where a hydrogen atom or ion is transferred.<sup>134-136</sup> Carbon atoms are normally considered to be on the large side for tunneling, however, carbon atom tunneling has been observed in the past.<sup>137,138</sup> The hypothesis of carbon tunneling also fits well with our NMR data which suggests that the carbide atoms spend little if any time in close proximity to the pyracylene cage atoms.

As the  $Y_2C_2$  cluster is placed in smaller and smaller cages, the geometry of the cluster becomes more and more compressed. This obviously leads to shorter and shorter Y-C bond lengths, but NMR  $^1J_{Y-C}$  coupling data and models suggest that the bond is becoming weaker even as it is becoming shorter. Our data in comparison with published data<sup>119</sup> shows that the forces exerted by the cage on the cluster mimic the pressure forces exerted by the diamond anvil on  $Y_2C_3$  by Amano's group which produced a superconducting  $Y_2C_3$ . SQUID measurements are being performed on  $Y_2C_2@C_{3v}(8)C_{82}$  and  $Y_2C_2@D_3(85)C_{92}$  by Jianyuan Zhang of our group to test whether this compression leads to the similar superconducting behavior in the  $Y_2C_2$  fullerenes to that seen in high compression  $Y_2C_3$  by Amano.

## **CHAPTER 5: Gd<sub>2</sub>@C<sub>79</sub>N: STRUCTURAL AND ELECTRONIC PROPERTIES**

### **CONTRIBUTIONS:**

This chapter represents work published in the Journal of the American Chemical Society in 2011 detailing the synthesis, isolation and characterization of Gd<sub>2</sub>@C<sub>79</sub>N and a derivative.<sup>12</sup> Contributions to this chapter are as follows: Tim Fuhrer (author of this dissertation) performed all computational work reported in the manuscript. Synthesis and isolation were performed by Wujun Fu, Jianyuan Zhang, Caitlyn Dixon, Jiechao Ge, and Chunying Shu. Mass spectrometry was performed by Kim Harich. Electrochemical experiments were performed by Hunter Champion. Writing of the published manuscript was performed primarily by Wujun Fu with assistance from Jianyuan Zhang and direction from Harry Dorn.

### **INTRODUCTION:**

The ability to synthesize fullerenes with atoms other than carbon on the cage has become an intriguing idea in recent years with several applications.<sup>139-141</sup> The first of these was the aza(60) fullerene (C<sub>59</sub>N) reported by Wudl and coworkers.<sup>142</sup> This C<sub>59</sub>N was unstable and was easily dimerized to (C<sub>59</sub>N)<sub>2</sub>. For larger cage systems like C<sub>80</sub>, it is well recognized that endohedral clusters like trimetallic nitride template (TNT) (i.e. M<sub>3</sub>N@C<sub>80</sub>) stabilize a C<sub>80</sub><sup>6-</sup> cage. The stability of the aza(80) cage (C<sub>79</sub>N) was first reported by Akasaka and coworkers who characterized La<sub>2</sub>@C<sub>79</sub>N by mass spectrometry.<sup>143</sup> More recently, our group has reported the isolation and characterization of several paramagnetic dimetallic endohedral heterofullerenes (EHFs).<sup>144</sup> The EPR



studies on  $Y_2@C_{79}N$  indicate that the unpaired electron is localized between the two yttrium atoms rather than on the cage.

Gadolinium endohedral metallofullerenes (EMFs) have become very important in recent years because of their magnetic properties and their potential use as MRI contrast agents.<sup>69,71-75,145,146</sup> In this chapter, we report the structural and electronic properties of the first gadolinium based EHF;  $Gd_2@C_{79}N$ .<sup>12</sup> Our data show that this unique molecule displays an unusually high stability compared with other EHFs reported so far.<sup>144</sup> This molecule also has unique magnetic properties because the seven unpaired *f* electrons on each gadolinium atom can interact with an additional unpaired electron formally provided by the cage nitrogen atom.

## **EXPERIMENTAL AND COMPUTATIONAL METHODS:**

**Preparation, Separation and Characterization of  $Gd_2@C_{79}N$ :** The experimental work on this project was done primarily by Wujun Fu and Jianyuan Zhang of the Dorn group.<sup>12</sup> The preparation of  $Gd_2@C_{79}N$  was accomplished using a Kratschmer-Huffman generator to vaporize graphite rods containing a mixture of  $Gd_2O_3$ , graphite powder, and metallic copper with a mass ratio of 2.0:1.0:2.1 in a dynamic flow of He and  $N_2$ . The resulting soot was then extracted by refluxing with toluene in a Soxhlet extractor. The soluble extract was then separated by column chromatography using a cyclopentadiene-functionalized Merrifield peptide resin column, which retains most empty cage fullerenes as well as the more reactive endohedral fullerenes. The remaining fraction was separated into seven distinct fractions by HPLC using a pentabromobenzyl column. The yield ratio of  $Gd_2@C_{79}N$  using this protocol is about 1

mg for each gram of C<sub>60</sub> formed. This is about 10 times the yield seen for Y<sub>2</sub>@C<sub>79</sub>N (see **Figure 38**).

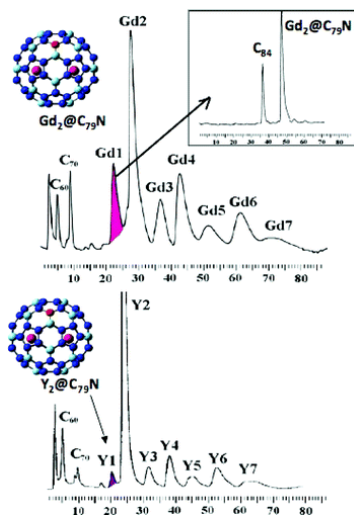


**Figure 38: HPLC Chromatography of soot extracts containing Gd<sub>2</sub>@C<sub>79</sub>N fractions and Y<sub>2</sub>@C<sub>79</sub>N fractions from separate soot preparations.**

The resulting Gd<sub>2</sub>@C<sub>79</sub>N was characterized by time-of-flight mass spectrometry, cyclic voltametry and EPR.<sup>12</sup>

**Computational Methods:** In order to augment the experimental observations and assist in explaining some of the physical properties of this new gadolinium heterofullerene, density functional theory (DFT) computations were performed for Gd<sub>2</sub>@C<sub>79</sub>N. In an effort to properly treat the unpaired electrons on the gadolinium atoms, the PBE0 functional<sup>110</sup> as described in the Gaussian 09<sup>127</sup> program package was used for Gd<sub>2</sub>@C<sub>79</sub>N, while the B3LYP functional<sup>102,103,126</sup> was used for the empty cage calculations. The PBE0 density functional was chosen for the Gadolinium containing fullerenes because it has been shown to have greater ability to model fullerenes that contain metal atoms with unpaired *f* electrons.<sup>109-111</sup> DFT-optimized energy values were obtained by performing a geometry optimization on starting geometries that were based on X-ray crystallographic structures of the Corresponding Tb<sub>2</sub>@C<sub>79</sub>N.<sup>144</sup> The 6-31G

basis set<sup>147</sup> was used for all carbon and nitrogen atoms in all computations. The CEP-121G basis set<sup>112,113,148</sup> was used for Gadolinium.

Once the geometry had been optimized for  $\text{Gd}_2@C_{79}\text{N}$ , a vibrational frequency analysis was performed to assure the each geometry was in fact a minimum on its potential energy hypersurface rather than a saddle point. Gaussian 09 computes a vibrational spectrum by taking the second derivatives of the quantum mechanical energies with respect to the Cartesian coordinates for each nucleus, and then converting those coordinates to mass weighted coordinates for the purpose of calculating the frequencies using harmonic approximation.<sup>49,50</sup> Once computed, the vibrational frequencies are then examined to make sure that no imaginary frequencies are contained. An imaginary vibrational frequency corresponds to a coordinate on the potential energy hypersurface where potential energy is at a maximum rather than a minimum.

## RESULTS AND DISCUSSION:

As shown in **Figure 39** (below) the heterofullerene  $(C_{79}\text{N})^{5-}$  and isoelectronic  $I_h$ - $(C_{80})^{6-}$  cage both have relatively large HOMO-LUMO gaps of 2.67 and 3.16 eV, respectively. These values are similar to the HOMO-LUMO gaps for well-known stable  $M_3\text{N}@I_h\text{-C}_{80}$  molecules.<sup>94,149-151</sup> It is also significant that the HOMO level and the total energy of the hetero fullerene cage  $(C_{79}\text{N})^{5-}$  is even lower than the isoelectronic cage  $I_h$ - $(C_{80})^{6-}$ . However, when an additional electron is added (**Figure 39c**) to the cage surface of the  $(C_{79}\text{N})^{5-}$  to make  $(C_{79}\text{N})^{6-}$ , the resulting HOMO-LUMO gap is relatively small (1.47 eV) and destabilized relative to  $(C_{79}\text{N})^{5-}$ . This result is consistent with the hypothesis that the  $(M_2)^{5+}$  endohedral cluster would be suitable for stabilization of a

heterofullerene  $(C_{79}N)^{5-}$  cage if the internal cluster can accept the unpaired electron formally from the nitrogen atom of the fullerene cage.

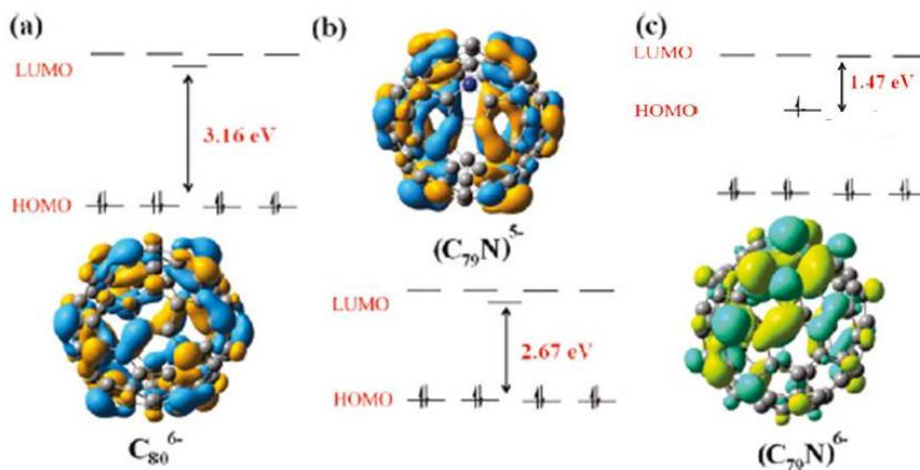


**Figure 39:** DFT HOMO-LUMO levels of  $(C_{80})^{6-}$ ,  $(C_{79}N)^{5-}$  and  $(C_{79}N)^{6-}$  cages.

Extension of the DFT approach to  $Gd_2@C_{79}N$  using the PBE0 functional and the CEP-121G basis set for gadolinium atoms provides energy levels that are comparable with the previously reported  $Y_2@C_{79}N$  system (**Figure 40**).<sup>144</sup> The computed HOMO-LUMO gap for  $Gd_2@C_{79}N$  (2.74 eV) is slightly larger than the previously computed HOMO-LUMO gap for  $Y_2@C_{79}N$  (2.39 eV).<sup>144</sup> Careful examination of each level below the HOMO indicates no significant Gd-Gd overlap until the HOMO-7 through HOMO-22 levels. We assign the HOMO-7 level as the highest of the fifteen singly-occupied molecular orbitals (SOMO) on  $Gd_2@C_{79}N$ . The HOMO-7 SOMO can be described in terms of a natural bonding order (NBO) as a  $Gd(s^1p^{0.95}d^{0.11}f^{0.06})-Gd(s^1p^{0.95}d^{0.11}f^{0.06})$  bond. Along with  $Y_2@C_{79}N$ ,  $Gd_2@C_{79}N$  then represents another example of spin-polarized orbitals that occur at energy levels below the HOMO.<sup>144</sup> The large degree of *s* character on the  $Gd_2$  cluster as well as the  $\alpha$  spin densities illustrated in **Figure 41** for both  $Gd_2@C_{79}N$  and  $Y_2@C_{79}N$  clearly indicate unpaired electron density localized between

the two gadolinium atoms rather than on the heterofullerene cage, but with a higher degree of *d* and *p* character in the spin orbital for the Gd<sub>2</sub>@C<sub>79</sub>N case than for the Y<sub>2</sub>@C<sub>79</sub>N.<sup>144</sup> The computed Gd-Gd bond distance for Gd<sub>2</sub>@C<sub>79</sub>N is 3.808 Å. While this is a long M-M bond, it is close to the X-ray crystallographic value for Tb<sub>2</sub>@C<sub>79</sub>N (3.902 Å) and the previously computed Y-Y distance in Y<sub>2</sub>@C<sub>79</sub>N (3.994 Å).<sup>144</sup>

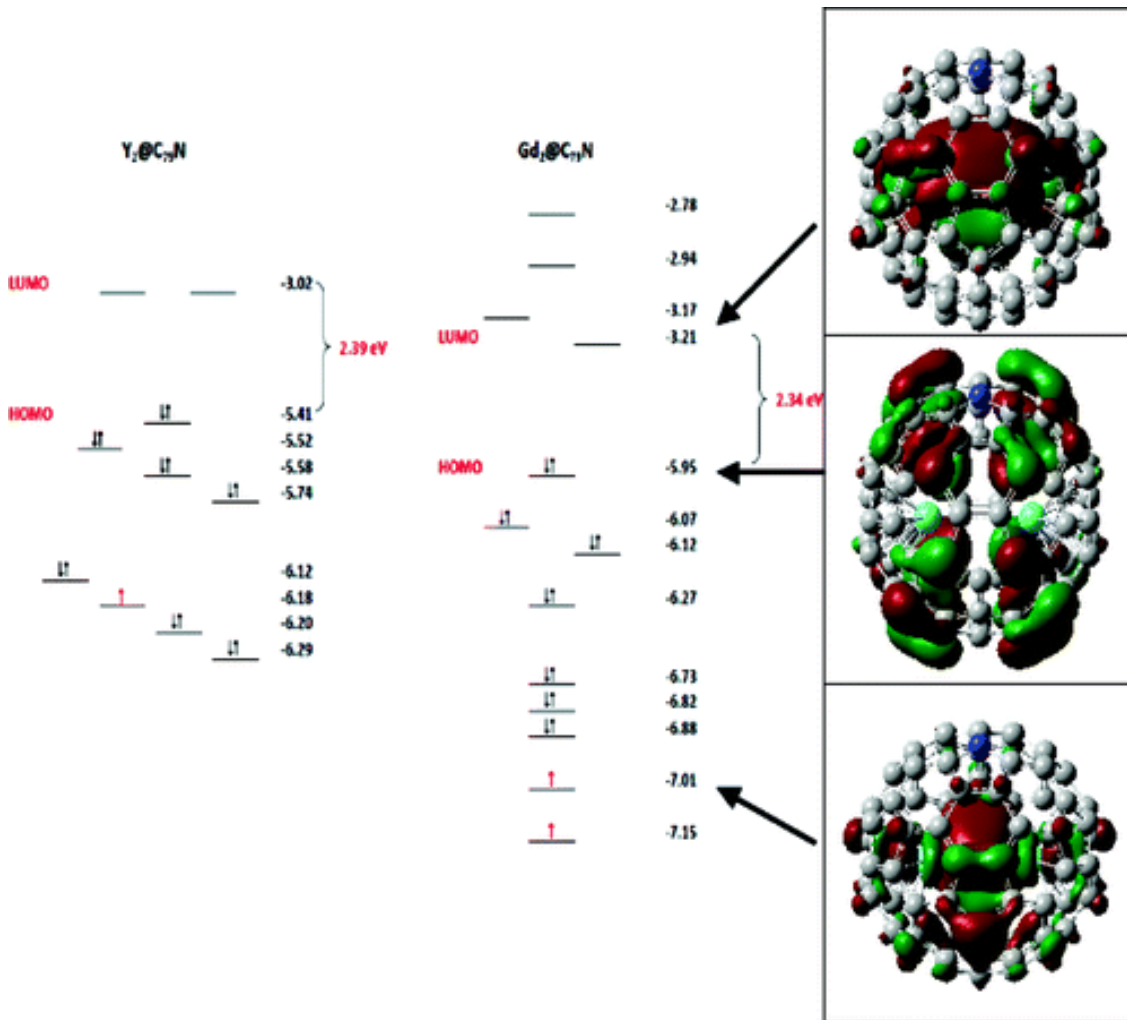


Figure 40: DFT MO energy level diagrams optimized for Y<sub>2</sub>@C<sub>79</sub>N and Gd<sub>2</sub>@C<sub>79</sub>N.<sup>12,144</sup>

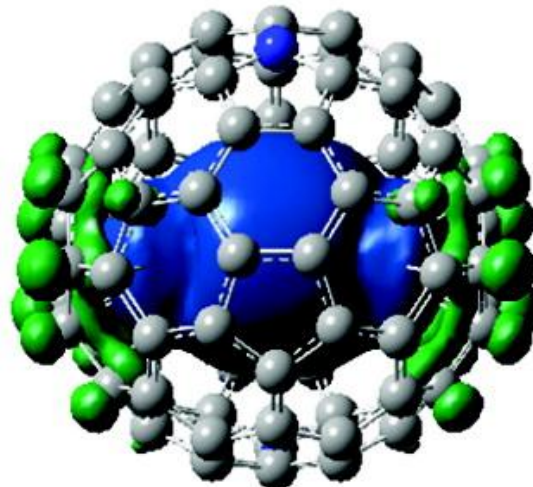
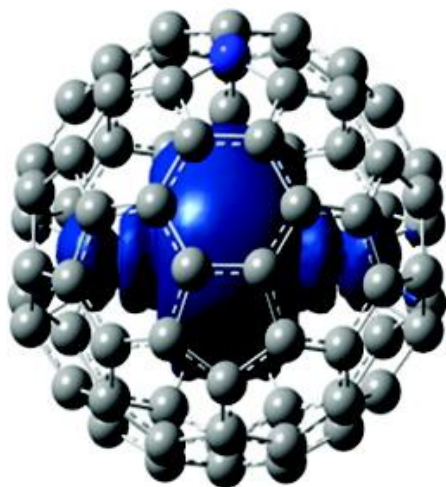


Figure 41: Unpaired Spin Density ( $\alpha$ ) distribution for  $\text{Y}_2@C_{79}\text{N}$  and  $\text{Gd}_2@C_{79}\text{N}$ <sup>12</sup>

## CONCLUSION:

In summary, we have prepared, separated, and characterized a new dimetallic EHF,  $\text{Gd}_2@C_{79}\text{N}$  for the first time. Theoretical computations presented herein agree with experimental results that this molecule has an unusually high chemical stability and the unpaired electron spin density is centered between the gadolinium atoms of the encapsulated  $\text{Gd}_2$  cluster. Additionally, this molecule can be described as having a spin quantum number of  $15/2$  as a result of the combination of two octet spins on the gadolinium atoms and an additional unpaired electron formally associated with the nitrogen atom on the cage, but found between the two gadolinium atoms of the cluster. As a result of its unusual stability and high spin state, we believe this unique EHF could be very useful in future biomedical, magnetic and electronic application areas.

## **CHAPTER 6: METATHESIS: REPLACING A METAL ATOM IN A FULLERENE CAGE**

### **CONTRIBUTIONS:**

This chapter represents work not yet published describing the plausibility of the so-called “metathesis reaction” in trimetallic-nitride template (TNT) endohedral metallofullerenes (EMF). Contributions to this chapter are as follows: Tim Fuhrer (author of this dissertation) performed all computational work reported in the manuscript. Experimental work thus far has all been performed by Hunter Champion and Jianyuan Zhang. Writing of the manuscript was performed primarily by Tim Fuhrer with direction from Harry Dorn.

### **INTRODUCTION:**

In view of the improving yields for  $\text{Sc}_3\text{N}@C_{80}$  that can now be achieved in the electric-arc process<sup>152</sup> and its commercial availability, it is important to explore whether metal-metal interchange metathesis reactions are feasible. Metathesis reactions will not only improve our understanding of the synthesis process, but could open new avenues for incorporating a wider range of different metals into endohedral metallofullerenes. The ability to incorporate different metals, particularly those that are radioactive or magnetically active, into the cage may lead to faster advances in medicine since the cage can isolate the metal ion from the biosystem.

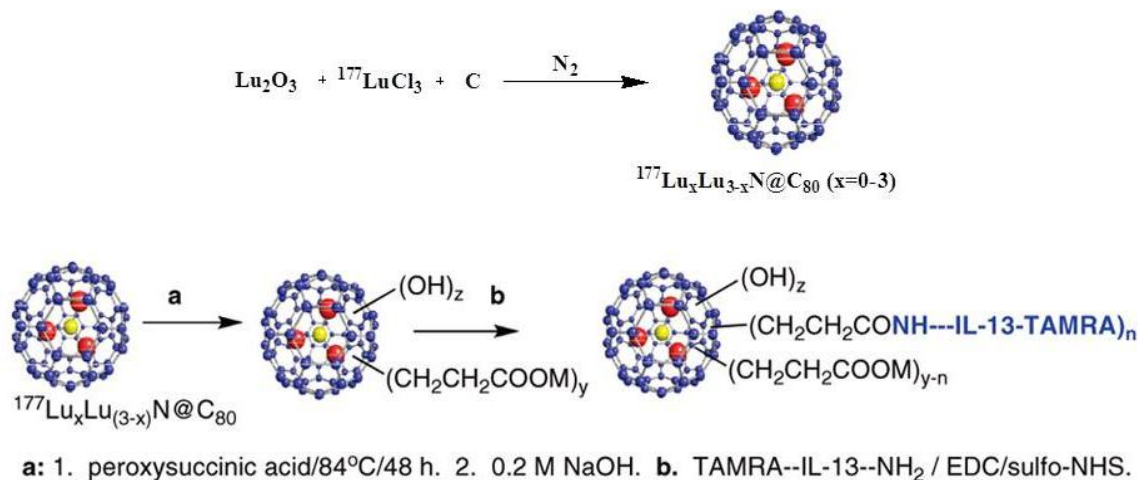


**Figure 42: Synthesis and functionalization of  $\beta$ -emitting  $\text{Lu}_3\text{N}@C_{80}$  for use in cancer therapy.**

For example,  $\beta$ -emitting ions have been found to be useful for treating cancer tumors.<sup>153</sup> Encapsulation of  $\beta$ -emitting lutetium-177 in an  $I_h$ - $C_{80}$  cage has been achieved in the Kratschmer-Huffman generator by Gibson *et al*, but at relatively low yields.<sup>76</sup> This  $\beta$ -emitting EMF was then functionalized with an interleukin-13 (IL-13) peptide that is designed to target an overexpressed receptor in glioblastoma multiforme tumors (see **Figure 42**).<sup>76,154</sup> Gadolinium containing EMFs have also been synthesized, but in lower yields than  $\text{Sc}_3\text{N}@C_{80}$ , and have been found to have relaxation times up to 30 to 40 times longer than MRI contrasting agents that are commercially available.<sup>73</sup> The metathesis reaction described herein may provide more efficient means of preparing these and other useful EMFs.

Experimental work on this project so far has been performed by Hunter Champion and Jianyuan Zhang of the Dorn group. The first attempt was to insert one or more yttrium atoms in place of scandium in  $\text{Sc}_3\text{N}@C_{80}$ . The reaction was performed by Jianyuan Zhang using a laser activation technique as illustrated in **Figure 43** below. As shown by the mass spectrometry results, about a 1% yield was achieved.



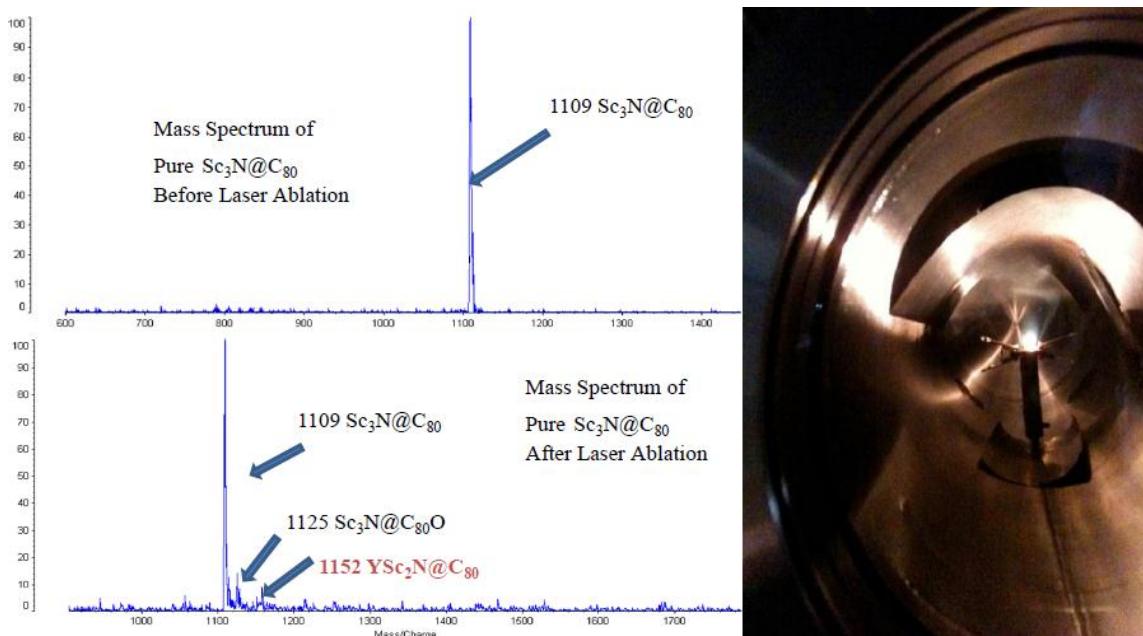


**Figure 43: Metathesis Reaction between Y (metal) and  $\text{Sc}_3\text{N}@C_{80}$  Yttrium metal powder (~40 mesh) and  $\text{Sc}_3\text{N}@C_{80}$  (mass ratio Y/  $\text{Sc}_3\text{N}@C_{80}$ =2/1) The pellet was irradiated by  $\text{CO}_2$  laser (10.6 micrometer, less than 25W) for about 6 minutes under 50 torr of  $\text{N}_2$ . (in chamber on the right)**

Hunter Champion attempted to insert one or more aluminum atoms into  $\text{Sc}_3\text{N}@C_{80}$ ,  $\text{Y}_3\text{N}@C_{80}$  or  $\text{Lu}_3\text{N}@C_{80}$  by thermal activation in a sealed quartz tube with low oxygen content at temperatures between  $650^\circ\text{C}$  and  $1000^\circ\text{C}$  (see **Figure 44** below). These trials are still ongoing.



**Figure 44: Sealed quartz tube containing  $\text{Sc}_3\text{N}@C_{80}$  and Al powder for attempted metathesis reaction.**

## COMPUTATIONAL METHODS:

The thermodynamic viability of these proposed reactions can be evaluated via quantum mechanical molecular modeling. For example, to predict the  $\Delta G_{reaction}$  at a range of temperatures for the following reaction:



one would compute the electronic and nuclear repulsion contributions to the total energy for each species using quantum mechanics, compute the remaining energetic terms (vibrational, rotational and translational) as well as the enthalpic (PV) and entropic (at various temperatures) terms using the same method described in the statistical mechanics portion of chapter one of this work. Since the models used in the computations assume gas phase single molecules, terms accounting for the free energies of sublimation of each species will need to be added into the calculation of  $\Delta G_{reaction}$  via Hess's Law.

In order to gain an understanding of the thermodynamics of several proposed reactions, we modeled  $\text{Sc}_3\text{N@C}_{80}$ ,  $\text{Sc}_2\text{YN@C}_{80}$ ,  $\text{Sc}_2\text{AlN@C}_{80}$ ,  $\text{Sc}_2\text{LuN@C}_{80}$ ,  $\text{Sc}_2\text{GdN@C}_{80}$ ,  $\text{Sc}_2\text{LaN@C}_{80}$ , Sc,  $\text{Sc}^{3+}$ , Y,  $\text{Y}^{3+}$ , Al,  $\text{Al}^{3+}$ , Gd,  $\text{Gd}^{3+}$ , Lu,  $\text{Lu}^{3+}$ , La and  $\text{La}^{3+}$  using the PBE0 density functional and the 6-31G(d) basis set for carbon, nitrogen, scandium, aluminum, the DZVP basis set for yttrium, and the cep-121G electronic core potential basis set for gadolinium, lutetium and lanthanum.<sup>87,112,113,128</sup> The PBE0 density function was chosen because of the success with which it has been shown to model fullerenes that contain metal atoms with unpaired *f* electrons.<sup>109-111</sup> we then used the computed free energies to model the thermodynamics for several hypothetical metathesis reactions involving  $\text{Sc}_3\text{N@C}_{80}$  reacting with a particular metal in several different forms (gas, solid, gas ion, solid oxide). In order to simplify the model somewhat, we made the

assumption that the free energy of sublimation of the product endohedral metallofullerene is the same as the free energy of sublimation of the reactant endohedral, allowing us to approximate the  $\Delta G_{reaction}$  of reaction (1) above by computing  $\Delta G_{reaction}$  for:



and assuming that  $\Delta G_{reaction(1)} = \Delta G_{reaction(2)}$ .

Modeling both the neutral atom and the 3+ ion for each proposed reactant metal allowed for the prediction of  $\Delta G_{reaction}$  for the reaction of  $Sc_3N@C_{80}$  with both the neutral metal and a salt of that metal. For example, in the lutetium case,  $\Delta G_{reaction}$  can be computed for the following reaction:



by modeling the species involved as described above, but including terms for the free energies of sublimation of  $Lu_2O_3$  and  $Sc_2O_3$  in the Hess's Law calculation of  $\Delta G_{reaction}$ .

## RESULTS AND DISCUSSION:

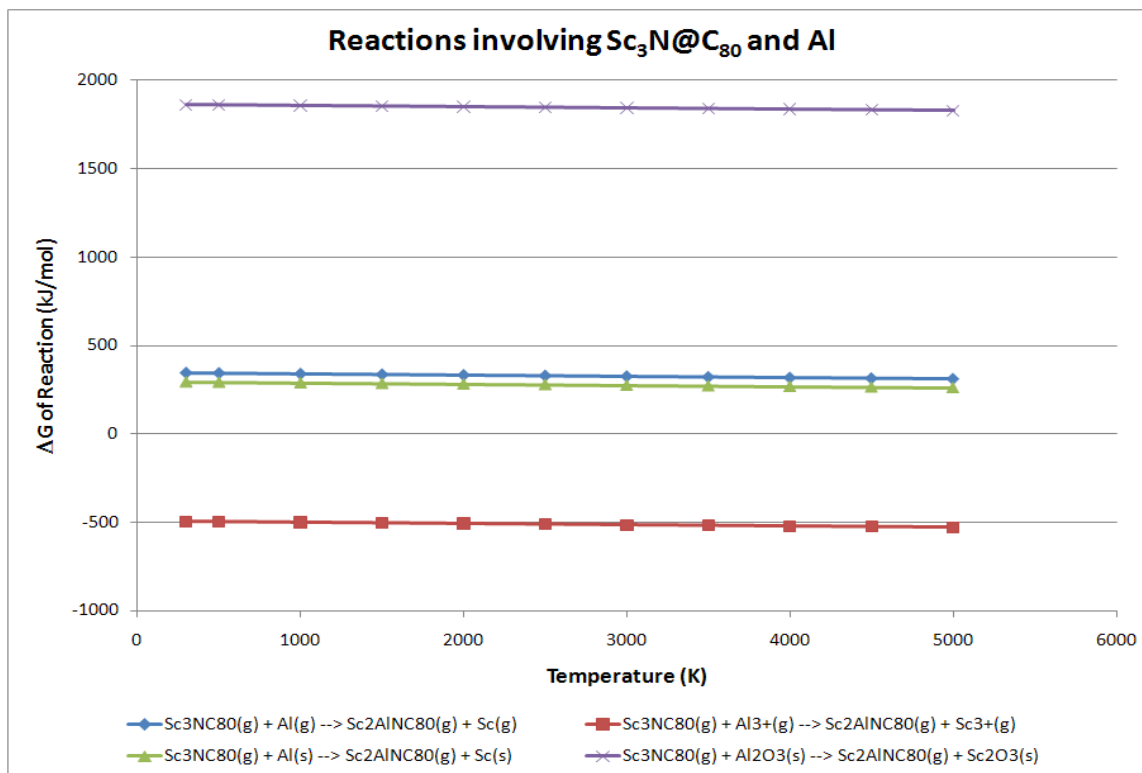


**Figure 45:** Plot of computed  $\Delta G$  of reaction versus temperature for reactions involving  $\text{Sc}_3\text{N}@C_{80}$  and aluminum in several forms. Crystal entropy effects are not included for the oxide case.

**Figure 45** (above) shows the results of computations involving the reaction of  $\text{Sc}_3\text{N}@C_{80}$  with aluminum in several different forms (chemical equations for each reaction shown in the figure). Based on these results, it is unlikely that we will have success with a metathesis reaction involving aluminum and  $\text{Sc}_3\text{N}@C_{80}$  from a thermodynamic viewpoint. Of the four reactions modeled, the only one with an exergonic Gibbs free energy change is the one involving gas phase  $\text{Al}^{3+}$ , which would be quite difficult to achieve at reasonable temperatures, but not necessarily impossible using laser activation of  $\text{Al}_2\text{O}_3$ .

The results of computations of the Gibbs free energy chances for the reactions of lutetium in several forms with  $\text{Sc}_3\text{N}@C_{80}$  are shown in **Figure 46** below (chemical

equations for each reaction shown in the figure). Reaction of solid metal lutetium with  $\text{Sc}_3\text{N}@C_{80}$  is a bit more promising than for the aluminum case, but yields should still be expected to be less than one percent.

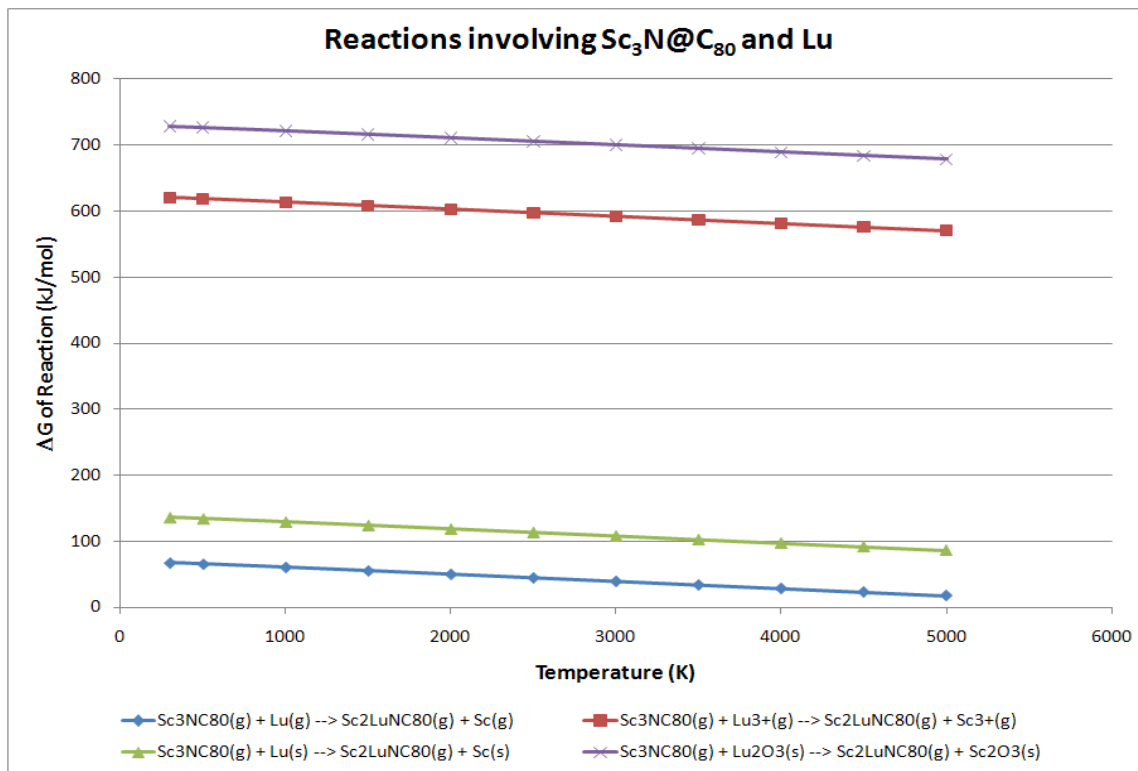


**Figure 46:** Plot of computed  $\Delta G$  of reaction versus temperature for reactions involving  $\text{Sc}_3\text{N}@C_{80}$  and lutetium in several forms. Crystal entropy effects are not included for the oxide case.

**Figure 47** (below) shows the results of computations involving  $\text{Sc}_3\text{N}@C_{80}$  and yttrium in several forms (chemical equations for each reaction shown in the figure). Predictions for the reactions of  $\text{Sc}_3\text{N}@C_{80}$  with solid yttrium metal match the experimental results reported earlier of about a one percent yield. The exciting thing here is the prediction of an extremely exergonic reaction between  $\text{Sc}_3\text{N}@C_{80}$  and solid yttrium oxide.

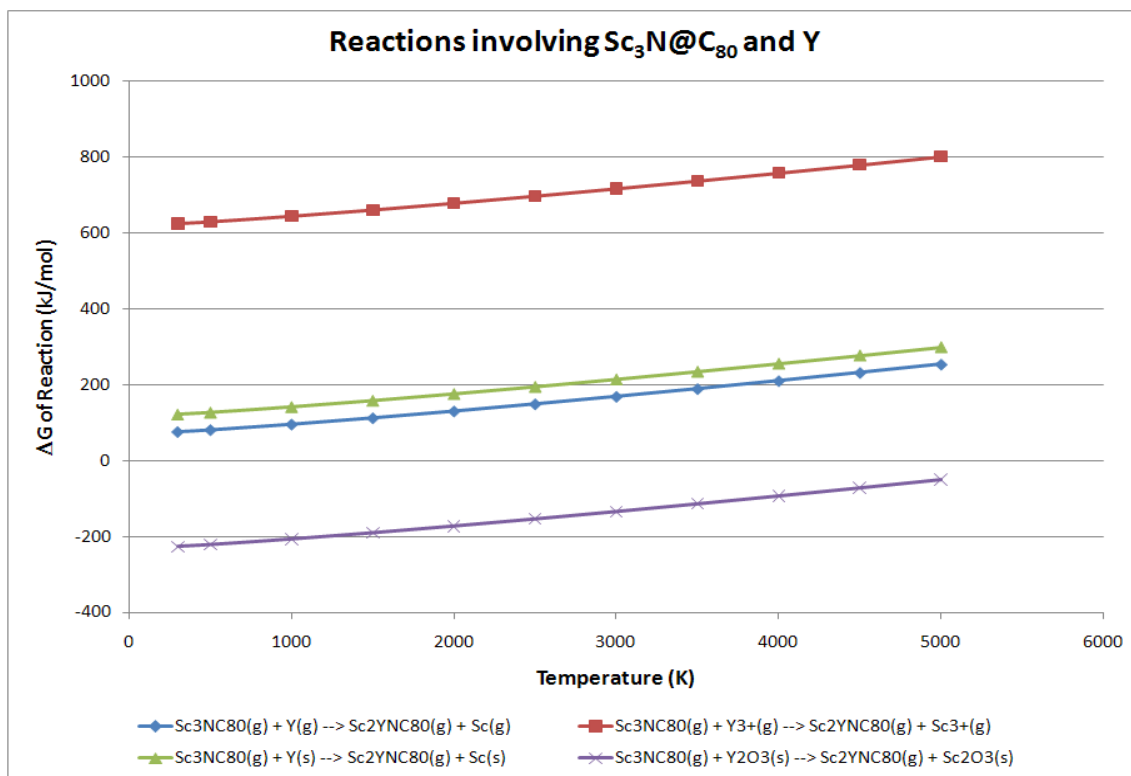


**Figure 47: Plot of computed  $\Delta G$  of reaction versus temperature for reactions involving  $\text{Sc}_3\text{N}@C_{80}$  and yttrium in several forms. Crystal entropy effects are not included for the oxide case.**

The predicted Gibbs free energies for the reactions of gadolinium in several forms with  $\text{Sc}_3\text{N}@C_{80}$  are shown in **Figure 48** (chemical equations for each reaction shown in the figure). Based on these results, our best option for metathesis reaction involving gadolinium with  $\text{Sc}_3\text{N}@C_{80}$  would be the reaction of solid metal gadolinium with  $\text{Sc}_3\text{N}@C_{80}$ . Beginning with gas phase gadolinium is slightly more favorable from a thermodynamic standpoint, but complicates the experiment because the high temperatures needed for sublimation of gadolinium would decompose the fullerene cage.



Figure 48: Plot of computed  $\Delta G$  of reaction versus temperature for reactions involving  $\text{Sc}_3\text{N}@C_{80}$  and gadolinium in several forms. Crystal entropy effects are not included for the oxide case.

Figure 49 (below) shows the results of computations involving the reactions of  $\text{Sc}_3\text{N}@C_{80}$  with Lanthanum in several forms (chemical equations for each reaction shown in the figure). In addition to yttrium, lanthanum presents another very promising case for the metathesis reaction in that a very exergonic reaction is predicted for the reaction of  $\text{Sc}_3\text{N}@C_{80}$  with lanthanum oxide.

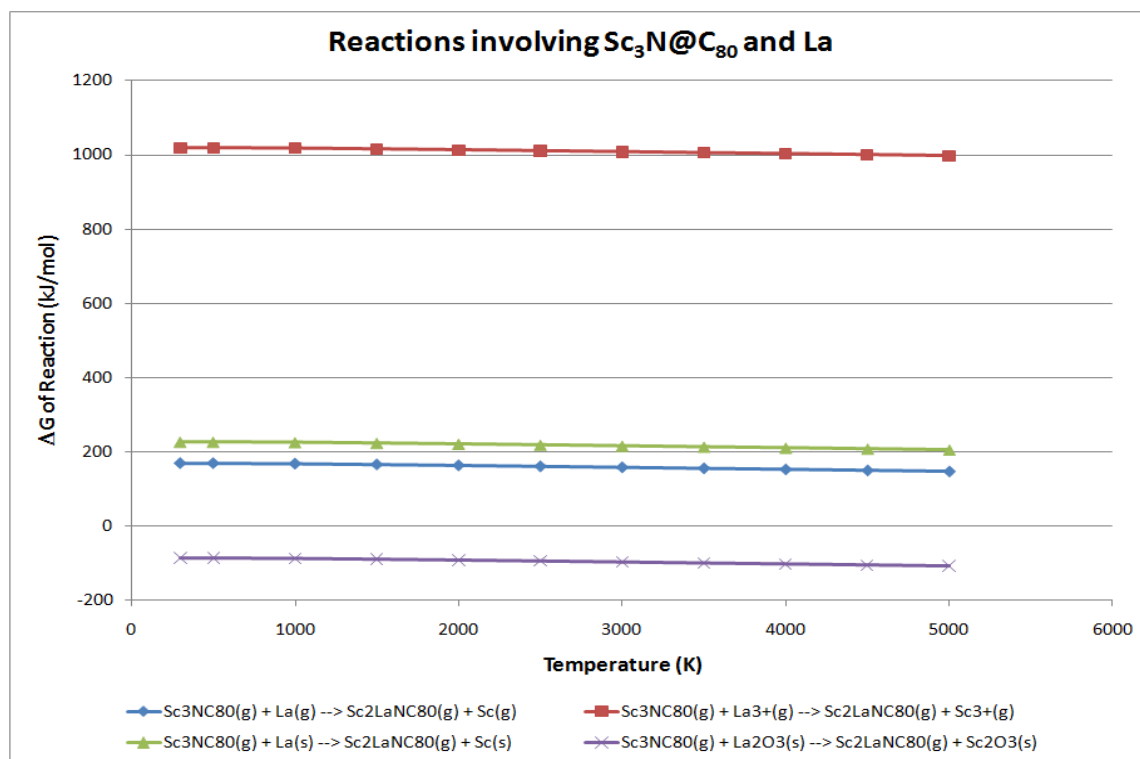


**Figure 49: Plot of computed  $\Delta G$  of reaction versus temperature for reactions involving  $\text{Sc}_3\text{N@C}_{80}$  and lanthanum in several forms. Crystal entropy effects are not included for the oxide case.**

## CONCLUSION:

In summary, we have presented computational predictions for the Gibbs free energies of reaction for the reactions of several metals in several forms with  $\text{Sc}_3\text{N@C}_{80}$  in order to predict the feasibility of a metal-metal exchange “metathesis” reaction. Based on computations so far, we should not expect appreciable yields for the metathesis reaction of Al with  $\text{Sc}_3\text{N@C}_{80}$  unless the Al ions are in the gas phase (very high temperature perhaps using laser ablation). The Lu case is a bit more promising in the neutral atom, but <1% yields would still be expected at reasonable temperatures. We should also not expect appreciable yields for the reaction of Gd with  $\text{Sc}_3\text{N@C}_{80}$ , unless Gd is in its neutral state and in the gas phase (very high temperature). Yields at  $\leq 1\%$  are expected for the reaction of Y(s) metal with  $\text{Sc}_3\text{N@C}_{80}$  which agrees with our experiments so far,



but the reaction of  $\text{Y}_2\text{O}_3(\text{s})$  with  $\text{Sc}_3\text{N}@\text{C}_{80}$  is predicted to give much more significant yields, as could the reaction of  $\text{La}_2\text{O}_3$  with  $\text{Sc}_3\text{N}@\text{C}_{80}$ .

Computations are currently running to investigate the thermodynamic viability of reactions involving ytterbium metal or ytterbium salts with either  $\text{Sc}_3\text{N}@\text{C}_{80}$  or  $\text{Lu}_3\text{N}@\text{C}_{80}$ . These reactions have shown some promise in the lab, but the geometry optimizations that are needed to model these reactions have yet to converge.

## CHAPTER 7: CONCLUDING REMARKS

### GENERAL COMMENTS:

The research presented herein describes the computational modeling of several classes of fullerenes and endohedral metallofullerenes. Through these computational studies and the experimental studies performed by our group, we have been able to predict and explain the properties of several novel endohedral metallofullerenes as well as develop theories about the structure and stability of endohedral metallofullerenes in general.

By looking at the anions of  $C_{94}$  and  $C_{80}$ , we discover a general theory about the stability of the fullerene anions that encase the clusters of EMFs. Specifically, cages with more pyracyclene bonding motifs become less stable as negative charge on the cage is increased because the negative charge collects on the pentagon atoms, causing negatively charged cages to be less stable with the pentagons bonded together. That being said, even though the pentagon atoms become more negatively charged, the bonds within the pentagons become shorter, which signifies that the added electron density is localizing in the bonding orbitals between those atoms. This is to be expected as the additional electron in the pentagon for allow for aromaticity of the pentagon.

We also report on two novel endohedrals, the  $Y_2C_2@C_{92}$ , and the  $Gd_2@C_{79}N$ . NMR and computational evidence support the idea of a unique cluster rotation in the  $Y_2C_2@C_{92}$  that we refer to as a “carousel rotation”. The  $Gd_2@C_{79}N$  is not only unique because of its incorporation of a nitrogen atom onto the cage, but for its significant lack of reactivity, particularly for a molecule with a spin quantum number of  $15/2$ .

Perhaps the most interesting part of this report is the computational and experimental evidence for the possibility of the so-called “metathesis” metal-metal interchange reaction for endohedral metallofullerenes.  $\text{Sc}_3\text{N@C}_{80}$  can be made in the graphite-arc reactor in large yields. The reaction of  $\text{Sc}_3\text{N@C}_{80}$  with several metals is explored and found to be thermodynamically favorable for the replacement of one of the scandium atoms with yttrium or lanthanum.

### **FULLERENE ANIONS:**

Fullerene anions are of interest computationally because most metal clusters in endohedral metallofullerenes (EMFs) have a net positive charge, leaving the cage with a net negative charge. This provides a convenient way of approximating models for EMFs without modeling the cluster, by modeling the appropriate empty cage anion. We have done this for all the dianions of the  $\text{C}_{94}$  IPR isomeric set (134 isomers). We have also modeled all of the IPR isomers for  $\text{C}_{80}$  (seven isomers) at all charges between zero and negative six. Analysis of that data has shown a lack of ability for cages with pyracyclene bonding motifs to accept negative charge, probably because of localization of that added charge on the pentagons, which become smaller with added electrons, possibly due to the addition of those electrons to bonding LUMO orbitals on the pentagon.

A more challenging and time consuming task, but perhaps more instructive, would be to model, in the same way we did for  $\text{C}_{80}$ , all of the IPR isomers of a slightly larger fullerene cage that would have a larger number of isomers. The  $\text{C}_{84}$  cage for example has 24 IPR isomers. A full computational treatment of all 24 of these isomers at

all of the charges for which we did the  $C_{80}$  isomers would give more data points and therefore more detail and reliability to the conclusions we have drawn based on  $C_{80}$ .

### **CARBIDE CLUSTERS:**

Our work concerning  $Y_2C_2@C_{92}$  has helped us find out some very interesting things about the cluster dynamics of carbide groups inside of fullerenes. The puzzling question that has not yet been answered is of how they are formed. Is the  $C_2$  unit surrounded by a forming cage and then encased in that cage? Or, is the  $C_2$  unit ejected from a larger cage into the middle of the cage that has already encased the 2 metal atoms? While there are computational approaches to this problem that might yield useful results, an experimental approach that would give great insight would be to use an isotopically normal graphite rod in the arc generator, packed with carbon-13 labeled yttrium carbide. Once  $Y_2C_2@C_{92}$  is isolated from the plasma arc soot, NMR spectral signals will tell us whether the carbide group in the molecule has higher carbon-13 abundance than the cage, which would support the hypothesis of the  $C_2$  unit being surrounded from the start rather than ejected from the cage.

Additionally, the cluster geometry of carbides in general needs a bit more investigation. While the geometries of  $Gd_2C_2@C_{92}$  and  $Y_2C_2@C_{92}$  have been found to have the metal atoms of the  $M_2C_2$  cluster oriented along the cage main  $D_3$  symmetry axis,<sup>8,9</sup> preliminary computational and experimental findings for  $Y_2C_2@C_{82}$  suggest that the metal atoms may be oriented orthogonal to the main  $C_{3v}$  axis of the cage with the carbide group aligned with the main axis. Both computational models and high resolution NMR spectra are being run to confirm or refute this hypothesis.

## OTHER FUTURE DIRECTIONS:

The atomic and subatomic interactions that cause the formation of fullerenes in the plasma arc have long been of intense interest in the literature. There has been extensive of molecular dynamics work done in an effort to computationally simulate the formation of fullerenes in the plasma arc environment.<sup>114,116,117,155-158</sup> The carbon pentagons that must form in order for fullerenes to be made are thought to be created in the plasma arc by pressure caused by the inert gas in the chamber.<sup>159</sup> In particular, the pentagons are thought to close from the  $C_{18}$  geometry shown in **Figure 43** below.<sup>160</sup> Several different catalysts have been shown to cause the kinds of defects that begin the “pentagon road” including chlorine and compounds containing chlorine atoms or chloride ions.<sup>161</sup>

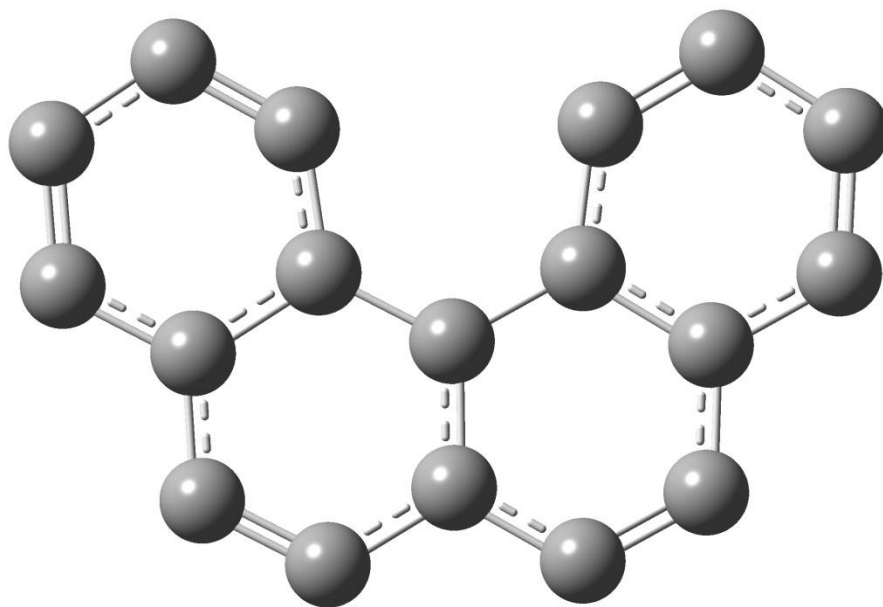


**Figure 50:  $C_{18}$  unit thought to be a precursor to pentagon closure in fullerenes.**

Computational models are being developed to try to explain the role of chlorine as a catalyst in the ring closure by placing either hydrogen or chlorine atoms to terminate

each carbon on the C<sub>18</sub> unit shown in **Figure 50** and calculating the pentagon closure energy for several different configurations of chlorines and hydrogens. Results so far suggest that the orth-para directing nature of chlorine atoms on aromatic rings explains their role as pentagon closure catalysts in fullerene formation.

## **CONCLUSION:**

Knowledge about the formation, structure, and possible applications for fullerenes and endohedral metallofullerenes is still growing at a fantastic rate. This work scratches some of the surfaces of what is still yet to come in the world of fullerene discovery, but there is still infinitely more for us to find in the years to come.

## APPENDIX 1: Relative Energies of C<sub>94</sub><sup>2-</sup> ion isomers

Isomer	$\Delta E$ (kJ/mol)
124 C2	0
132 C1	5.81243692
<b>134</b> C3v	9.92412745
118 C1	15.04456133
75 C1	17.62590043
119 C1	19.66121428
122 C1	20.13369926
125 C1	22.6486132
20 C2	22.76872982
130 C2	23.36442952
123 C1	29.18096222
117 C2	32.63596269
95 C1	33.10206771
51 C2	36.77758392
91 C1	36.77881791
36 C1	37.28756104
112 C1	38.44606292
101 C1	40.15059002
65 C1	41.27797972
131 C1	42.23833511
59 C1	42.42091238
126 C2	43.83379895
43 C2	44.42590171
128 C1	44.58763251
56 C1	46.43041845
120 Cs	47.37617606
82 C1	49.30300426
34 C1	49.54124213
45 Cs	49.78381207
15 C1	50.0338647
74 C1	50.30237458
18 Cs	51.46591741
133 C2	53.23442796
68 C1	53.92054988
57 C1	53.99096579
44 Cs	54.46163917
61 C2	54.56348231
97 C1	55.1601797
115 C1	56.79387082
72 C1	57.27053034
19 C1	57.39537287
111 C1	57.88484483
127 C1	58.15889453
31 Cs	58.61607284
62 C1	59.44326287

42 Cs	59.89925971
129 C1	60.83055081
47 C2	60.9670243
98 C1	61.63384879
12 C1	62.03316109
121 C2	62.66477763
92 C1	63.14918237
37 C1	63.31645298
73 C2	64.21642187
21 C1	66.42767048
116 C1	67.45786417
85 C1	70.65913632
87 C1	71.72645458
94 C2	72.86124819
35 C1	73.80020575
16 C1	74.68925256
69 C1	74.71548131
110 C3	75.16136997
32 C1	75.40905964
102 C1	78.3774762
49 C1	79.17964521
54 C1	79.67835894
24 C2v	79.86474318
103 C1	80.09161264
64 C1	80.76379315
66 C1	83.22556697
99 C1	85.33092916
80 C1	85.63280915
81 C1	86.03361798
60 C1	86.12868734
93 C1	88.4194886
76 C1	89.06683188
67 C1	89.84715674
105 C1	91.93587326
8 C1	94.40452589
55 C1	95.1118881
50 C1	96.23449939
3 C2	97.77165087
71 C1	98.84855221
53 C1	99.20782563
90 C1	100.2255744
33 C2	100.3220616
48 C1	101.9050018
96 C3	104.0218899
113 C1	104.7510438
58 C1	105.4834007

22 C2	106.4389777
114 C3	109.2432743
108 C2	114.8448573
77 C1	114.9379313
78 C1	115.9039577
83 C1	119.2428849
23 Cs	119.8989185
5 C1	122.0811816
79 C1	122.6580565
39 Cs	122.8374044
86 C2	125.9694421
70 C1	127.2339092
10 C1	128.2524456
11 C1	128.2524456
14 Cs	131.2059231
104 C1	132.510324
88 C1	132.5334547
25 C1	135.9703392
9 C2	136.1260838
63 C1	137.0817133
29 C1	138.1280801
106 C1	141.6890195
100 C1	143.7465976
109 C2	149.0157135
84 C1	149.6622954
17 Cs	159.0853725
41 C1	167.3162099
107 C2	178.4819626
40 Cs	181.1351879
7 C2	181.2027945
89 C2	182.1436687
4 C2	183.7138752
6 C1	183.972907
13 Cs	184.4078211
27 C1	184.6560621
52 C2v	190.4551353
28 C1	208.3638545
38 C1	210.3256019
2 C1	213.3118456
1 C2	221.3951825
30 C1	245.3634507
26 C2	252.8653181
46 Cs	273.1255403

**APPENDIX 2: Effect on atomic charges and bond lengths of adding 6 electrons to each isomer of C<sub>80</sub>. Bond types are shown in more detail in Figure 4 (a=4 Hexagons, b=Pyracyclene, c=Pent. to Hex., d=Pent. Edge)**

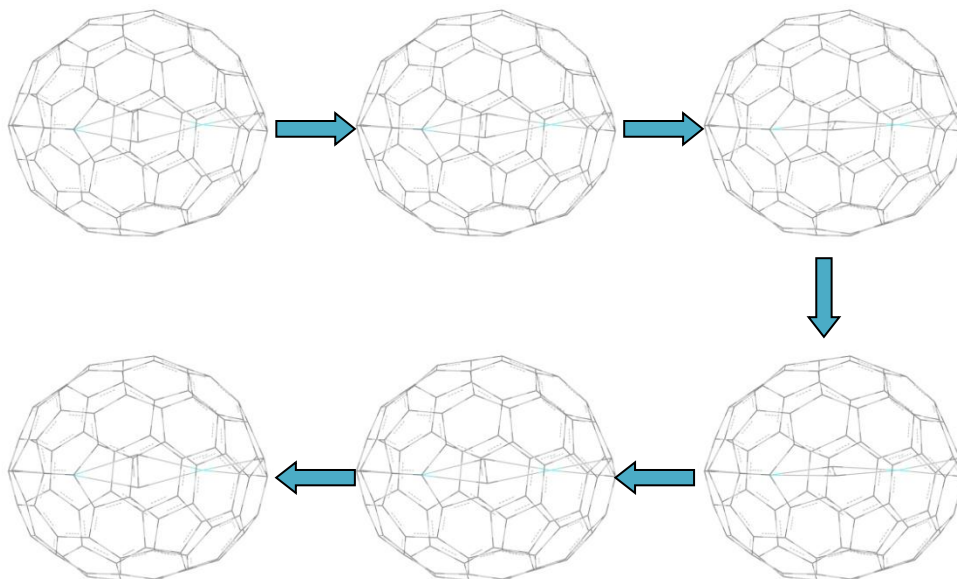
Isomer	Atom	Avg ΔCharge.	St.Dev.	Bond	Avg. ΔLength	St.Dev.
<b>1D5D</b>	Pyracyclene	-0.0879	0.0023	Pyracyclene	0.0333	0.0032
	NonPyraPent	-0.0647	0.0001	Pent. to Hex.	0.0239	0.0000
	Hex-1Pent			4 Hexagons	0.0011	0.0163
				Pent. Edge	-0.0015	0.0043
<b>2D2</b>	Pyracyclene	-0.0816	0.0312	Pyracyclene	0.0326	0.0221
	NonPyraPent	-0.0837	0.0216	Pent. to Hex.	0.0240	0.0071
	Hex-1Pent	-0.0550	0.0144	4 Hexagons	-0.0026	0.0059
	Hex-2Pent	-0.0440	0.0000	Pent. Edge	0.0000	0.0169
<b>3C2v</b>	Pyracyclene	-0.0734	0.0267	Pyracyclene	0.0299	0.0184
	NonPyraPent	-0.0909	0.0199	Pent. to Hex.	0.0192	0.0174
	Hex-1Pent	-0.0705	0.0081	4 Hexagons	-0.0062	0.0095
	Hex-2Pent	-0.0400	0.0103	Pent. Edge	0.0021	0.0172
	Hex-3Pent	-0.0210	0.0061			
<b>4D3</b>	Pyracyclene	-0.0839	0.0121	Pyracyclene	0.0385	0.0059
	NonPyraPent	-0.0875	0.0153	Pent. to Hex.	0.0097	0.0082
	Hex-0Pent	-0.0658	0.0007	4 Hexagons	0.0089	0.0036
	Hex-1Pent	-0.0473	0.0006	Pent. Edge	0.0023	0.0136
	Hex-2Pent	-0.0371	0.0080			
<b>5C2v</b>	Pyracyclene	-0.0749	0.0189	Pyracyclene	0.0318	0.0144
	NonPyraPent	-0.0886	0.0144	Pent. to Hex.	0.0139	0.0129
	Hex-1Pent	-0.0684	0.0001	4 Hexagons	-0.0046	0.0115
	Hex-2Pent	-0.0487	0.0085	Pent. Edge	0.0038	0.0163
	Hex-3Pent	-0.0314	0.0101			
<b>6D5h</b>	Pyracyclene	-0.0813	0.0537	Pyracyclene	0.0338	0.0010
	NonPyraPent	-0.0764	0.0453	Pent. to Hex.	0.0102	0.0076
	Hex-2Pent	-0.0620	0.0321	4 Hexagons	-0.0009	0.0118
	Hex-3Pent	-0.0749	0.0538	Pent. Edge	0.0055	0.0177
<b>7Ih</b>	NonPyraPent	-0.0850	0.0057	Pent. to Hex.	0.0089	0.0122
	Hex-3Pent	-0.0449	0.0054	Pent. Edge	0.0075	0.0082



**APPENDIX 3: Dependence of relative energy (kJ/mol) of C<sub>80</sub> IPR isomers on charge of the cage. The *D*<sub>5h</sub>(6)C<sub>80</sub><sup>2-</sup> is shown to have the lowest energy of the 49 systems modeled.**

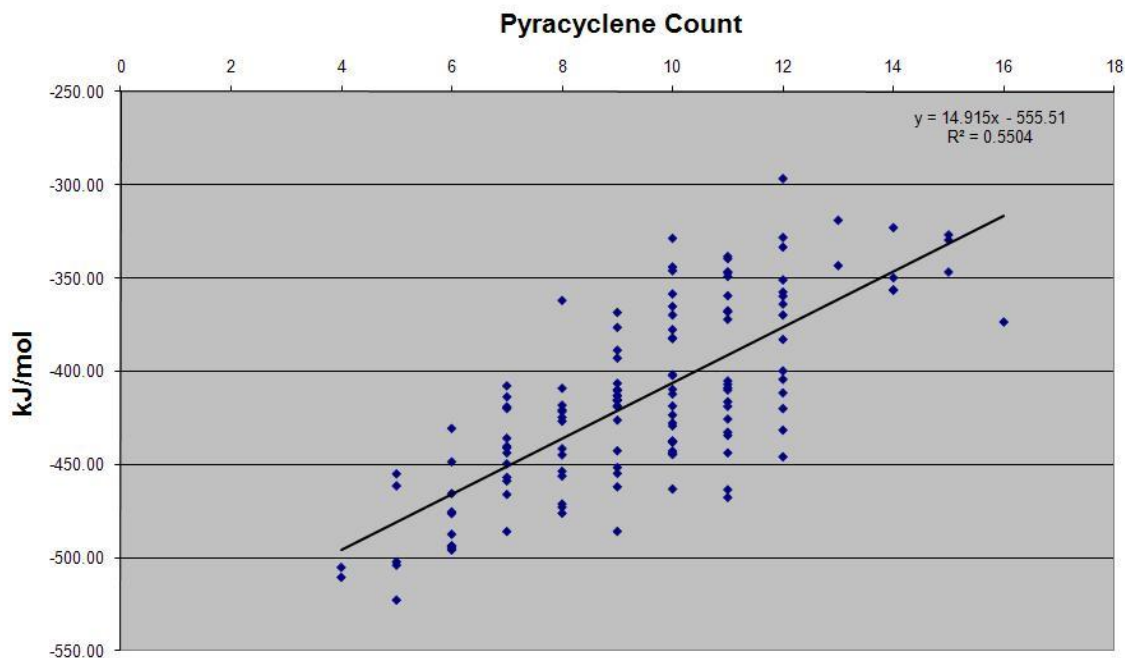
<b>Isomer</b>	<b>0</b>	<b>-1</b>	<b>-2</b>	<b>-3</b>	<b>-4</b>	<b>-5</b>	<b>-6</b>
1-D5d	361.75	82.40	78.52	447.01	1075.85	1994.30	3157.78
2-D2	350.95	83.50	90.75	425.24	1030.74	1916.92	3070.01
3-C2v	378.92	62.85	20.49	355.92	966.24	1832.27	2974.33
4-D3	387.64	94.38	77.96	408.94	1018.28	1869.54	2996.64
5-C2v	385.88	60.42	9.22	292.49	855.24	1717.46	2858.10
6-D5h	396.51	55.81	<u>0.00</u>	281.88	841.85	1651.83	2736.08
7-Ih	465.39	132.68	82.00	311.31	813.93	1590.12	2640.03

**APPENDIX 4: Six geometries of  $Y_2C_2C_{92}$  optimized to confirm carousel rotation hypothesis. For each structure, the cage symmetry axis is horizontal through the cluster.**

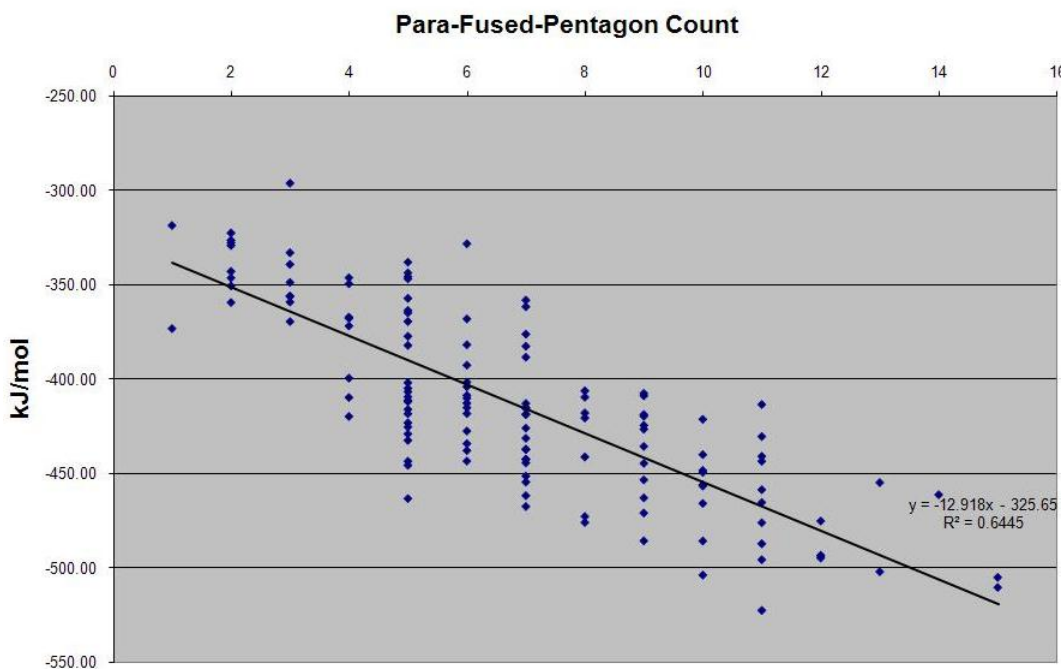


**APPENDIX 5: Complete plot of dielectron affinities of the C<sub>94</sub> IPR isomers vs. number of pyracyclene motifs on each and verse number of para-fused-pentagon motifs on each.**

**C<sub>94</sub> Dielectron Affinities**



**C<sub>94</sub> Dielectron Affinities**



## REFERENCES

- (1) Kratschmer, W.; Lamb, L. D.; Fostiropoulos, K.; Huffman, D. R. *Nature* **1990**, *347*, 354-358.
- (2) Fowler, P. W.; Manolopoulos, D. E. *An Atlas of Fullerenes*; Dover: Mineola, NY, 2006.
- (3) Richter, H.; Labrocca, A. J.; Grieco, W. J.; Taghizadeh, K.; Lafleur, A. L.; Howard, J. B. *The Journal of Physical Chemistry B* **1997**, *101*, 1556-1560.
- (4) Richter, H.; Taghizadeh, K.; Grieco, W. J.; Lafleur, A. L.; Howard, J. B. *The Journal of Physical Chemistry* **1996**, *100*, 19603-19610.
- (5) Slanina, Z.; Zhao, X.; Uhlik, F.; Lee, S.-L. *Journal of Molecular Structure: THEOCHEM* **2003**, *630*, 205-213.
- (6) Fuhrer, T.; Dorn, H. C. In *VAS; VAS: VCU Richmond Virginia*, 2009.
- (7) Fuhrer, T. J.; Dorn, H. C. In *SERMACS 2010 New Orleans, LA*, 2010.
- (8) Yang, H.; Lu, C.; Liu, Z.; Jin, H.; Che, Y.; Olmstead, M. M.; Balch, A. L. *Journal of the American Chemical Society* **2008**, *130*, 17296-17300.
- (9) Burke, B. G.; Chan, J.; Williams, K.; Fu, W.; Fuhrer, T.; Dorn, H. C.; Puretzky, A. A.; Geohegan, D. B. 2010.
- (10) Zhang, J.; Fuhrer, T.; Fu, W.; Ge, J.; Bearden, D. W.; Dallas, J.; Duchamp, J.; Walker, K.; Champion, H.; Azurmendi, H.; Harich, K.; Dorn, H. C. *Journal of the American Chemical Society* **2012**.
- (11) Fuhrer, T. J.; Dorn, H. C. In *217th ECS Meeting Vancouver, BC*, 2010.
- (12) Fu, W.; Zhang, J.; Fuhrer, T.; Champion, H.; Furukawa, K.; Kato, T.; Mahaney, J. E.; Burke, B. G.; Williams, K. A.; Walker, K.; Dixon, C.; Ge, J.; Shu, C.; Harich, K.; Dorn, H. C. *Journal of the American Chemical Society* **2011**, *133*, 9741-9750.
- (13) Fuhrer, T. J.; Dorn, H. C. In *ECS 2011 Montreal, Quebec*, 2011.
- (14) Kroto, H. W.; Heath, J. R.; O'Brien, S. C.; Curl, R. F.; Smalley, R. E. *Nature* **1985**, *318*, 162-163.
- (15)
- (16) Taylor, R.; Hare, J. P.; Abdul-Sada, A. a. K.; Kroto, H. W. *Journal of the Chemical Society, Chemical Communications* **1990**, *20*, 1423-1425.
- (17) Buseck, P. R.; Tshipursky, S. J.; Hettich, R. *Science* **1992**, *257*, 215-217.
- (18) Cami, J.; Bernard-Salas, J.; Peeters, E.; Malek, S. E. *Science* **2010**, *329*, 1180-1182.
- (19) Manolopoulos, D. E.; May, J. C.; Down, S. E. *Chemical Physics Letters* **1991**, *181*, 105-111.
- (20) Kroto, H. W. *Nature* **1987**, *329*, 529-531.
- (21) Schmalz, T. G.; Seitz, W. A.; Klein, D. J.; Hite, G. E. *Journal of the American Chemical Society* **1988**, *110*, 1113-1127.
- (22) Zhang, B. L.; Wang, C. Z.; Ho, K. M.; Xu, C. H.; Chan, C. T. *The Journal of Chemical Physics* **1992**, *97*, 5007-5011.
- (23) Diederich, F.; Whetten, R. L.; Thilgen, C.; Ettl, R.; Chao, I. T. O.; Alvarez, M. M. *Science* **1991**, *254*, 1768-1770.
- (24) Kikuchi, K.; Nakahara, N.; Wakabayashi, T.; Suzuki, S.; Shiromaru, H.; Miyake, Y.; Saito, K.; Ikemoto, I.; Kainosho, M.; Achiba, Y. *Nature* **1992**, *357*, 142-145.

- (25) Diederich, F.; Ettl, R.; Rubin, Y.; Whetten, R. L.; Beck, R.; Alvarez, M.; Anz, S.; Sensharma, D.; Wudl, F.; Khemani, K. C.; Koch, A. *Science* **1991**, 252, 548-551.
- (26) Osawa, E. *Kagaku (Kyoto)* **1970**, 25, 854-863.
- (27) Davidson, R. A. *Theoretical Chemistry Accounts: Theory, Computation, and Modeling (Theoretica Chimica Acta)* **1981**, 58, 193-231.
- (28) Jones, D. E. H. *New Scientist* **1966**, 35.
- (29) Dewar, M. J. S.; Thiel, W. *Journal of the American Chemical Society* **1977**, 99, 4899-4907.
- (30) Newton, M. D.; Stanton, R. E. *Journal of the American Chemical Society* **1986**, 108, 2469-2470.
- (31) Fowler, P. W. *Chemical Physics Letters* **1986**, 131, 444-450.
- (32) Klein, D. J.; Schmalz, T. G.; Hite, G. E.; Seitz, W. A. *Journal of the American Chemical Society* **1986**, 108, 1301-1302.
- (33) Rudzinski, J. M.; Slanina, Z.; Togasi, M.; Osawa, E.; Iizuka, T. *Thermochimica Acta* **1988**, 125, 155-162.
- (34) Fowler, P. W.; Lazzeretti, P.; Zanasi, R. *Chemical Physics Letters* **1990**, 165, 79-86.
- (35) Schulman, J. M.; Disch, R. L.; Miller, M. A.; Peck, R. C. *Chemical Physics Letters* **1987**, 141, 45-48.
- (36) Luthi, H. P.; Almlöf, J. *Chemical Physics Letters* **1987**, 135, 357-360.
- (37) Manolopoulos, D. E. *J. Chem. Soc. Faraday Trans.* **1991**, 87, 2861-2862.
- (38) Fowler, P. W.; Battan, R. C.; Manolopoulos, D. E. *J. Chem. Soc. Faraday Trans.* **1991**, 87, 3103-3104.
- (39) Manolopoulos, D. E.; Fowler, P. W. *Journal of Chemical Physics* **1992**, 96, 7603-7614.
- (40) Raghavachari, K. *Chemical Physics Letters* **1992**, 190, 397-400.
- (41) Zhang, B. L.; Wang, C. Z.; Ho, K. M. *The Journal of Chemical Physics* **1992**, 96, 7183-7185.
- (42) Bakowies, D.; Kolb, M.; Thiel, W. *Chemical Physics Letters* **1992**, 200, 411-417.
- (43) Bakowies, D. *Chemical Physics Letters* **1992**, 197, 324-329.
- (44) Raghavachari, K.; Rohlfing, C. M. *Chemical Physics Letters* **1993**, 208, 436-440.
- (45) Colt, J. R.; Scuseria, G. E. *Journal of Physical Chemistry* **1992**, 96, 10265-10268.
- (46) Slanina, Z. *International Journal of Quantum Chemistry* **1979**, 16, 79-86.
- (47) Frisch, M. J.; Trucks, G. W.; Schlegel, H. B.; Scuseria, G. E.; Robb, M. A.; Cheeseman, J. R.; Montgomery, J., J. A.; Vreven, T.; Kudin, K. N.; Burant, J. C.; Millam, J. M.; Iyengar, S. S.; Tomasi, J.; Barone, V.; Mennucci, B.; Cossi, M.; Scalmani, G.; Rega, N.; Petersson, G. A.; Nakatsuji, H.; Hada, M.; Ehara, M.; Toyota, K.; Fukuda, R.; Hasegawa, J.; Ishida, M.; Nakajima, T.; Honda, Y.; Kitao, O.; Nakai, H.; Klene, M.; Li, X.; Knox, J. E.; Hratchian, H. P.; Cross, J. B.; Bakken, V.; Adamo, C.; Jaramillo, J.; Gomperts, R.; Stratmann, R. E.; Yazyev, O.; Austin, A. J.; Cammi, R.; Pomelli, C.; Ochterski, J. W.; Ayala, P. Y.; Morokuma, K.; Voth, G. A.; Salvador, P.; Dannenberg, J. J.; Zakrzewski, V. G.; Dapprich, S.; Daniels, A. D.; Strain, M. C.; Farkas, O.; Malick, D.

- K.; Rabuck, A. D.; Raghavachari, K.; Foresman, J. B.; Ortiz, J. V.; Cui, Q.; Baboul, A. G.; Clifford, S.; Cioslowski, J.; Stefanov, B. B.; Liu, G.; Liashenko, A.; Piskorz, P.; Komaromi, I.; Martin, R. L.; Fox, D. J.; Keith, T.; Al-Laham, M. A.; Peng, C. Y.; Nanayakkara, A.; Challacombe, M.; Gill, P. M. W.; Johnson, B.; Chen, W.; Wong, M. W.; Gonzalez, C.; Pople, J. A.; Gaussian, Inc.: Wallingford CT, 2004.
- (48) McQuarrie, D. A. *Statistical Thermodynamics*; Harper and Row: New York, 1973.
- (49) Pulay, P. *Molecular Physics* **1969**, *17*, 197-204.
- (50) Johannes, N.; Markus, R.; Carsten, K.; Bernd, A. H. *Journal of Computational Chemistry* **2002**, *23*, 895-910.
- (51) Nash, L. H. *Elements of Statistical Thermodynamics*; Dover Mineola, NY, 2006.
- (52) Slanina, Z.; Rudzinski, J. M.; Osawa, E. *Carbon* **1987**, *25*, 747-750.
- (53) Slanina, Z.; Frangoisa, J.-P.; Bakowiesb, D.; Thielb, W. *Journal of Molecular Structure: THEOCHEM* **1993**, *279*, 213-216.
- (54) Slanina, Z.; Lee, S.-L. *Journal of Molecular Structure: THEOCHEM* **1995**, *333*, 153-158.
- (55) Lee, S.-L.; Sun, M.-L.; Slanina, Z. *International Journal of Quantum Chemistry: Quantum Chemistry Symposium* **1996**, *30*, 1567-1576.
- (56) Nakao, K.; Kurita, N.; Fujita, M. *Physical Review B* **1994**, *49*, 11415.
- (57) Slanina, Z.; Lee, S.-L.; Adamowicz, L. *International Journal of Quantum Chemistry* **1997**, *63*, 529-535.
- (58) Stevenson, S.; Rice, G.; Glass, T.; Harich, K.; Cromer, F.; Jordan, M. R.; Craft, J.; Hadju, E.; Bible, R.; Olmstead, M. M.; Maitra, K.; Fisher, A. J.; Balch, A. L.; Dorn, H. C. *Nature* **1999**, *401*, 55-57.
- (59) Zhao, X.; slanina, Z.; Goto, H.; Osawa, E. *Journal of Chemical Physics* **2003**, *118*, 10534-10540.
- (60) Che, Y.; Yang, H.; Wang, Z.; Jin, H.; Liu, Z.; Lu, C.; Zuo, T.; Dorn, H. C.; Beavers, C. M.; Olmstead, M. M.; Balch, A. L. *Inorganic Chemistry* **2009**, *48*, 6004-6010.
- (61) Slanina, Z.; Uhlik, F.; Adamowicz, L.; Kobayashi, K.; Nagase, S. *International Journal of Quantum Chemistry* **2004**, *100*, 600-616.
- (62) Zdenek, S.; Shyi-Long, L.; Filip, U.; Ludwik, A.; Shigeru, N. *International Journal of Quantum Chemistry* **2006**, *106*, 2222-2228.
- (63) Frank, H. H.; Rudi, H. M.; Achim, F.; Sabine, R.-S.; Stefan, G.; Manfred, M. K.; Dirk, F.; Martin, B.; Kaoru, K.; Shigeru, N. *S. Angew Chem Int Ed Engl* **1996**, *35*, 1732-1734.
- (64) Heath, J. R.; O'Brien, S. C.; Zhang, Q.; Liu, Y.; Curl, R. F.; Tittel, F. K.; Smalley, R. E. *Journal of the American Chemical Society* **1985**, *107*, 7779-7780.
- (65) Chai, Y.; Guo, T.; Jin, C.; Haufler, R. E.; Chibante, L. P. F.; Fure, J.; Wang, L.; Alford, J. M.; Smalley, R. E. *The Journal of Physical Chemistry* **2002**, *95*, 7564-7568.
- (66) Johnson, R. D.; de Vries, M. S.; Salem, J.; Bethune, D. S.; Yannoni, C. S. *Nature* **1992**, *355*, 239-240.
- (67) Bethune, D. S.; Johnson, R. D.; Salem, J. R.; de Vries, M. S.; Yannoni, C. S. *Nature* **1993**, *366*, 123-128.

- (68) Stevenson, S.; Stephen, R. R.; Amos, T. M.; Cadorette, V. R.; Reid, J. E.; Phillips, J. P. *Journal of the American Chemical Society* **2005**, *127*, 12776-12777.
- (69) J. Wilson, L.; W. Cagle, D.; P. Thrash, T.; J. Kennel, S.; Mirzadeh, S.; Michael Alford, J.; J. Ehrhardt, G. *Coordination Chemistry Reviews* **1999**, *190-192*, 199-207.
- (70) Iezzi, E. B.; Duchamp, J. C.; Fletcher, K. R.; Glass, T. E.; Dorn, H. C. *Nano Letters* **2002**, *2*, 1187-1190.
- (71) Kato, H.; Kanazawa, Y.; Okumura, M.; Taninaka, A.; Yokawa, T.; Shinohara, H. *Journal of the American Chemical Society* **2003**, *125*, 4391-4397.
- (72) Bolskar, R. D.; Benedetto, A. F.; Husebo, L. O.; Price, R. E.; Jackson, E. F.; Wallace, S.; Wilson, L. J.; Alford, J. M. *Journal of the American Chemical Society* **2003**, *125*, 5471-5478.
- (73) Fatouros, P. P.; Corwin, F. D.; Chen, Z.-J.; Broaddus, W. C.; Tatum, J. L.; Kettenmann, B.; Ge, Z.; Gibson, H. W.; Russ, J. L.; Leonard, A. P.; Duchamp, J. C.; Dorn, H. C. *Radiology* **2006**, *240*, 756-764.
- (74) Shu, C.-Y.; Ma, X.-Y.; Zhang, J.-F.; Corwin, F. D.; Sim, J. H.; Zhang, E.-Y.; Dorn, H. C.; Gibson, H. W.; Fatouros, P. P.; Wang, C.-R.; Fang, X.-H. *Bioconjugate Chemistry* **2008**, *19*, 651-655.
- (75) Shu, C.; Corwin, F. D.; Zhang, J.; Chen, Z.; Reid, J. E.; Sun, M.; Xu, W.; Sim, J. H.; Wang, C.; Fatouros, P. P.; Esker, A. R.; Gibson, H. W.; Dorn, H. C. *Bioconjugate Chemistry* **2009**, *20*, 1186-1193.
- (76) Shultz, M. D.; Duchamp, J. C.; Wilson, J. D.; Shu, C.-Y.; Ge, J.; Zhang, J.; Gibson, H. W.; Fillmore, H. L.; Hirsch, J. I.; Dorn, H. C.; Fatouros, P. P. *Journal of the American Chemical Society* **2010**, *132*, 4980-4981.
- (77) Kobayashi, K.; Nagase, S.; Yoshida, M.; ÅEsawa, E. *Journal of the American Chemical Society* **1997**, *119*, 12693-12694.
- (78) Wan, T. S. M.; Zhang, H.-W.; Nakane, T.; Xu, Z.; Inakuma, M.; Shinohara, H.; Kobayashi, K.; Nagase, S. *Journal of the American Chemical Society* **1998**, *120*, 6806-6807.
- (79) Foreman, J. B.; Frisch, A. *Exploring Chemistry with Electronic Structure Methods*; 2nd ed.; Gaussian, Inc.: Pittsburgh, PA, 1996.
- (80) Fowler, P. W.; Manolopoulos, D. E. *Chemical Physics Letters* **1991**, *187*, 1-7.
- (81) Chai, Y.; Guo, T.; Jin, C.; Haufler, R. E.; Chibante, L. P. F.; Fure, J.; Wang, L.; Alford, J. M.; Smalley, R. E. *The Journal of Physical Chemistry* **1991**, *95*, 7564-7568.
- (82) Kobayashi, K.; Nagase, S. *Chemical Physics Letters* **1998**, *282*, 325-329.
- (83) Thomas, R. C.; Walter, J. S.; AIP: 1993; Vol. 98, p 5555-5565.
- (84) Cao, X.; Dolg, M. *Journal of Chemical Physics* **2001**, *115*, 7348-7355.
- (85) Cao, X.; Dolg, M. *Journal of Molecular Structure: THEOCHEM* **2002**, *581*, 139-147.
- (86) Senapati, L.; Schrier, J.; Whaley, K. B. *Nano Letters* **2004**, *4*, 2073-2078.
- (87) Stevens, W. J.; Krauss, M.; Basch, H.; Jasien, P. G. *Canadian Journal of Chemistry* **1992**, *70*, 612-630.

- (88) Slanina, Z.; Zhao, X.; Grabuleda, X.; Ozawa, M.; Uhlík, F.; Ivanov, P.; Kobayashi, K.; Nagase, S. *Journal of Molecular Graphics and Modelling* **2001**, *19*, 252-255.
- (89) Slanina, Z.; Kobayashi, K.; Nagase, S. *Journal of Chemical Physics* **2004**, *120*, 3397-3400.
- (90) Xu, Z.; Nakane, T.; Shinohara, H. *Journal of the American Chemical Society* **1996**, *118*, 11309-11310.
- (91) Slanina, Z.; Adamowicz, L.; Kobayashi, K.; Nagase, S. *Molecular Simulation* **2005**, *31*, 71-77.
- (92) Zdenek, S.; Shigeru, N. *ChemPhysChem* **2005**, *6*, 2060-2063.
- (93) Duchamp, J. C.; Demortier, A.; Fletcher, K. R.; Dorn, D.; Iezzi, E. B.; Glass, T.; Dorn, H. C. *Chemical Physics Letters* **2003**, *375*, 655-659.
- (94) Krause, M.; Dunsch, L. *ChemPhysChem* **2004**, *5*, 1445-1449.
- (95) Slanina, Z.; Chen, Z.; Schleyer, P. v. R.; Uhlík, F.; Lu, X.; Nagase, S. *The Journal of Physical Chemistry A* **2006**, *110*, 2231-2234.
- (96) Stevenson, S.; Burbank, P.; Harich, K.; Sun, Z.; Dorn, H. C.; van Loosdrecht, P. H. M.; deVries, M. S.; Salem, J. R.; Kiang, C. H.; Johnson, R. D.; Bethune, D. S. *The Journal of Physical Chemistry A* **1998**, *102*, 2833-2837.
- (97) Kato, H.; Taninaka, A.; Sugai, T.; Shinohara, H. *Journal of the American Chemical Society* **2003**, *125*, 7782-7783.
- (98) Kohn, W.; Sham, L. *Phys. Rev. A* **1965**, *140*, 1133.
- (99) Parr, R. G.; Yang, W. *Density-Functional Theory of Atoms and Molecules*; Oxford University Press: New York, 1989.
- (100) Cohen, A. J.; Mori-Sánchez, P.; Yang, W. *Science* **2008**, *321*, 792-794.
- (101) Sousa, S. r. F.; Fernandes, P. A.; Ramos, M. J. o. *The Journal of Physical Chemistry A* **2007**, *111*, 10439-10452.
- (102) Becke, A. D. *J. Chem. Phys* **1993**, *98*, 5648.
- (103) Lee, C.; Yang, W.; Parr, R. G. *Phys. Rev. B* **1988**, *37*, 785.
- (104) Perdew, J. P.; Schmidt, K. In *Density Functional Theory and Its Applications to Materials*; Van Doren, V. E., Vam Alseoy, K., Geerlings, P., Eds.; AIP Press: New York, 2001.
- (105) Zhao, Y.; Truhlar, D. G. *The Journal of Physical Chemistry A* **2004**, *108*, 6908-6918.
- (106) Zhao, Y.; Truhlar, D. G. *Journal of Chemical Theory and Computation* **2005**, *1*, 415-432.
- (107) Slanina, Z.; Pulay, P.; Nagase, S. *Journal of Chemical Theory and Computation* **2006**, *2*, 782-785.
- (108) Qian, M. C.; Khanna, S. N. *Journal of Applied Physics* **2007**, *101*.
- (109) Perdew, J. P.; Burke, K.; Ernzerhof, M. *Physical Review Letters* **1996**, *77*, 3865.
- (110) Adamo, C.; Barone, V. *The Journal of Chemical Physics* **1999**, *110*, 6158-6170.
- (111) Yang, S.; Popov, A.; Kalbac, M.; Dunsch, L. *Chemistry – A European Journal* **2008**, *14*, 2084-2092.
- (112) Stevens, W. J.; Basch, H.; Krauss, M. *J. Chem. Phys* **1984**, *81*, 6026.
- (113) Cundari, T. R.; Stevens, W. J. *J. Chem. Phys.* **1993**, *98*, 5555-65.



- (114) Maruyama, S.; Yamaguchi, Y. *Thermal Science & Engineering* **1995**, *3*.
- (115) Brenner, D. W. *Phys. Rev. B* **1990**, *42*, 9458-9471.
- (116) Maruyama, S.; Yamaguchi, Y. *Chemical Physics Letters* **1998**, *286*, 343-349.
- (117) Yamaguchi, Y.; Maruyama, S. *Chemical Physics Letters* **1998**, *286*, 336-342.
- (118) Slanina, Z.; Uhlík, F.; Lee, S.-L.; Adamowicz, L.; Nagase, S. *Chemical Physics Letters* **2008**, *463*, 121-123.
- (119) Amano, G.; Akutagawa, S.; Muranaka, T.; Zenitani, Y.; Akimitsu, J. *J. Phys. Soc. Jpn.* **2004**, *73*, 530-532.
- (120) Wang, C. R.; Kai, T.; Tomiyama, T.; Yoshida, T.; Kobayashi, Y.; Nishibori, E.; Takata, M.; Sakata, M.; Shinohara, H. *Angew Chem Int Edit* **2001**, *40*, 397.
- (121) Tan, K.; Lu, X. *Chemical Communications* **2005**, 4444-4446.
- (122) Iiduka, Y.; Wakahara, T.; Nakahodo, T.; Tsuchiya, T.; Sakuraba, A.; Maeda, Y.; Akasaka, T.; Yoza, K.; Horn, E.; Kato, T.; Liu, M. T. H.; Mizorogi, N.; Kobayashi, K.; Nagase, S. *Journal of the American Chemical Society* **2005**, *127*, 12500-12501.
- (123) Kurihara, H.; Lu, X.; Iiduka, Y.; Mizorogi, N.; Slanina, Z.; Tsuchiya, T.; Akasaka, T.; Nagase, S. *Journal of the American Chemical Society* **2011**, *133*, 2382-2385.
- (124) Inoue, T.; Tomiyama, T.; Sugai, T.; Okazaki, T.; Suematsu, T.; Fujii, N.; Utsumi, H.; Nojima, K.; Shinohara, H. *The Journal of Physical Chemistry B* **2004**, *108*, 7573-7579.
- (125) Fu, W.; Fuhrer, T.; Ge, J.; Dallas, J.; Bearden, D. W.; Champion, H.; Shu, C.; Azurmendi, H.; Harich, K.; Reid, J.; Dorn, H. C. 2010.
- (126) Stephens, P. J.; Devlin, F. J.; Chabalowski, C. F.; Frisch, M. J. *J. Phys. Chem.* **1994**, *98*, 11623.
- (127) Frisch, M. J.; Trucks, G. W.; Schlegel, H. B.; Scuseria, G. E.; Robb, M. A.; Cheeseman, J. R.; Scalmani, G.; Barone, V.; Mennucci, B.; Petersson, G. A.; Nakatsuji, H.; Caricato, M.; Li, X.; Hratchian, H. P.; Izmaylov, A. F.; Bloino, J.; Zheng, G.; Sonnenberg, J. L.; Hada, M.; Ehara, M.; Toyota, K.; Fukuda, R.; Hasegawa, J.; Ishida, M.; Nakajima, T.; Honda, Y.; Kitao, O.; Nakai, H.; Vreven, T.; Montgomery, J., J. A.; Peralta, J. E.; Ogliaro, F.; Bearpark, M.; Heyd, J. J.; Brothers, E.; Kudin, K. N.; Staroverov, V. N.; Kobayashi, R.; Normand, J.; Raghavachari, K.; Rendell, A.; Burant, J. C.; Iyengar, S. S.; Tomasi, J.; Cossi, M.; Rega, N.; Millam, N. J.; Klene, M.; Knox, J. E.; Cross, J. B.; Bakken, V.; Adamo, C.; Jaramillo, J.; Gomperts, R.; Stratmann, R. E.; Yazyev, O.; Austin, A. J.; Cammi, R.; Pomelli, C.; Ochterski, J. W.; Martin, R. L.; Morokuma, K.; Zakrzewski, V. G.; Voth, G. A.; Salvador, P.; Dannenberg, J. J.; Dapprich, S.; Daniels, A. D.; Farkas, Ö.; Foresman, J. B.; Ortiz, J. V.; Cioslowski, J.; Fox, D. J.; Revision A.1 ed.; Gaussian, Inc.: Wallingford CT, 2009.
- (128) Godbout, N.; Salahub, D. R.; Andzelm, J.; Wimmer, E. *Canadian Journal of Chemistry* **1992**, *70*, 560-571.
- (129) Valencia, R.; Rodriguez-Forteza, A.; Poblet, J. M. *Journal of Physical Chemistry A* **2008**, *112*, 4550-4555.
- (130) Yang, T.; Zhao, X. A.; Nagase, S. *Physical Chemistry Chemical Physics* **2011**, *13*, 5034-5037.

- (131) Zhang, Y.; Wu, A.; Xu, X.; Yan, Y. *Chemical Physics Letters* **2006**, *421*, 383-388.
- (132) Denhaan, K. H.; Wielstra, Y.; Teuben, J. H. *Organometallics* **1987**, *6*, 2053.
- (133) Yamazaki, Y.; Nakajima, K.; Wakahara, T.; Tsuchiya, T.; Ishitsuka, M. O.; Maeda, Y.; Akasaka, T.; Waelchli, M.; Mizorogi, N.; Nagase, S. *Angew Chem Int Edit* **2008**, *47*, 7905.
- (134) Garrett, B. C.; Truhlar, D. G.; Bowman, J. M.; Wagner, A. F.; Robie, D.; Arepalli, S.; Presser, N.; Gordon, R. J. *Journal of the American Chemical Society* **1986**, *108*, 3515-3516.
- (135) Truhlar, D. G.; Gao, J.; Alhambra, C.; Garcia-Viloca, M.; Corchado, J.; Sanchez, M. L.; Villa, J. *Accounts of Chemical Research* **2002**, *35*, 341-349.
- (136) Kohen, A.; Klinman, J. P. *Chemistry & biology* **1999**, *6*, R191-R198.
- (137) Zuev, P. S.; Sheridan, R. S.; Albu, T. V.; Truhlar, D. G.; Hrovat, D. A.; Borden, W. T. *Science* **2003**, *299*, 867-870.
- (138) Miller, D. J.; Subramanian, R.; Saunders, W. H. *Journal of the American Chemical Society* **1981**, *103*, 3519-3522.
- (139) Prassides, K.; Keshavarz-K, M.; Hummelen, J. C.; Andreoni, W.; Giannozzi, P.; Beer, E.; Bellavia, C.; Cristofolini, L.; Gonzalez, R.; Lappas, A.; Murata, Y.; Malecki, M.; Srdanov, V.; Wudl, F. *Science* **1996**, *271*, 1833-1835.
- (140) M. Poblet, J.; Munoz, J.; Winkler, K.; Cancilla, M.; Hayashi, A.; B. Lebrilla, C.; L. Balch, A. *Chemical Communications* **1999**, 493-494.
- (141) Vostrowsky, O.; Hirsch, A. *Chemical Reviews* **2006**, *106*, 5191-5207.
- (142) Hummelen, J. C.; Knight, B.; Pavlovich, J.; Gonzalez, R.; Wudl, F. *Science* **1995**, *269*, 1554-1556.
- (143) Akasaka, T.; Okubo, S.; Wakahara, T.; Yamamoto, K.; Kobayashi, K.; Nagase, S.; Kato, T.; Kako, M.; Nakadaira, Y.; Kitayama, Y.; Matsuura, K. *Chemistry Letters* **1999**, *28*, 945-946.
- (144) Zuo, T.; Xu, L.; Beavers, C. M.; Olmstead, M. M.; Fu, W.; Crawford, T. D.; Balch, A. L.; Dorn, H. C. *Journal of the American Chemical Society* **2008**, *130*, 12992-12997.
- (145) Sitharaman, B.; Wilson, L. J. *Journal of Biomedical Nanotechnology* **2007**, *3*, 342-352.
- (146) Chaur, M. N.; Melin, F.; Athans, A. J.; Elliott, B.; Walker, K.; Holloway, B. C.; Echegoyen, L. *Chemical Communications* **2008**, 2665-2667.
- (147) Hehre, W. J.; Ditchfield, R.; Pople, J. A. *J. Chem. Phys* **1972**, *56*, 2257.
- (148) Stevens, W. J.; Krauss, M.; Basch, H.; Jasien, P. G. *Can. J. Chem* **1992**, *70*, 612-630.
- (149) Elliott, B.; Yu, L.; Echegoyen, L. *Journal of the American Chemical Society* **2005**, *127*, 10885-10888.
- (150) Iiduka, Y.; Ikenaga, O.; Sakuraba, A.; Wakahara, T.; Tsuchiya, T.; Maeda, Y.; Nakahodo, T.; Akasaka, T.; Kako, M.; Mizorogi, N.; Nagase, S. *Journal of the American Chemical Society* **2005**, *127*, 9956-9957.
- (151) Cai, T.; Xu, L.; Anderson, M. R.; Ge, Z.; Zuo, T.; Wang, X.; Olmstead, M. M.; Balch, A. L.; Gibson, H. W.; Dorn, H. C. *Journal of the American Chemical Society* **2006**, *128*, 8581-8589.

- (152) Stevenson, S.; Mackey, M. A.; Thompson, M. C.; Coumbe, H. L.; Madasu, P. K.; Coumbe, C. E.; Phillips, J. P. *Chemical Communications* **2007**, 4263-4265.
- (153) Kneifel, S.; Bernhardt, P.; Uusijärvi, H.; Good, S.; Plasswilm, L.; Buitrago-Téllez, C.; Müller-Brand, J.; Mäcke, H.; Merlo, A. *European Journal of Nuclear Medicine and Molecular Imaging* **2007**, *34*, 1388-1395.
- (154) Debinski, W.; Miner, R.; Leland, P.; Obiri, N. I.; Puri, R. K. *Journal of Biological Chemistry* **1996**, *271*, 22428-22433.
- (155) Ohtsuki, T.; Ohno, K.; Shiga, K.; Kawazoe, Y.; Maruyama, S.; Masumoto, K. *Journal of Chemical Physics* **2000**, *112*, 2834-2842.
- (156) Maruyama, S.; Shibuta, Y. *Molecular Crystals and Liquid Crystals* **2002**, *387*, 311-316.
- (157) Shiga, K.; Ohno, K.; Kawazoe, Y.; Maruyama, Y.; Hirata, T.; Hatakeyama, R.; Sato, N. *Materials Science and Engineering a-Structural Materials Properties Microstructure and Processing* **2000**, *290*, 6-10.
- (158) Maruyama, S.; Yamaguchi, Y.; Kohno, M.; Yoshida, T. *Fullerene Science and Technology* **1999**, *7*, 621-636.
- (159) Smalley, R. E. *Accounts of Chemical Research* **1992**, *25*, 98-105.
- (160) Churilov, G. N.; Novikov, P. V.; Tarabanko, V. E.; Lopatin, V. A.; Vnukova, N. G.; Bulina, N. V. *Carbon* **2002**, *40*, 891-896.
- (161) Huang, R. B.; Xie, S. Y.; Tang, Z. C.; Wang, Y. H.; Huang, W. J.; Chen, H.; Zheng, L. S. *Journal of Cluster Science* **1999**, *10*, 383-396.